

University of Warwick institutional repository: <http://go.warwick.ac.uk/wrap>

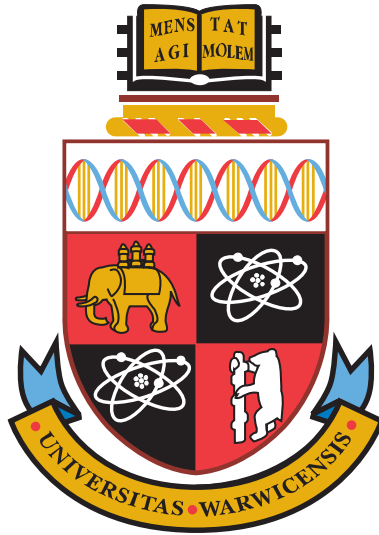
**A Thesis Submitted for the Degree of PhD at the University of Warwick**

<http://go.warwick.ac.uk/wrap/59339>

This thesis is made available online and is protected by original copyright.

Please scroll down to view the document itself.

Please refer to the repository record for this item for information to help you to cite it. Our policy information is available from the repository home page.



# Interactions in the Integer Quantum Hall Effect

by

**Christoph Sohrmann**

**Thesis**

Submitted to the University of Warwick

for the degree of

**Doctor of Philosophy**

**Physics**

September 2007

THE UNIVERSITY OF  
**WARWICK**

# Contents

<b>List of Figures</b>	<b>v</b>
<b>Acknowledgments</b>	<b>viii</b>
<b>Declarations</b>	<b>ix</b>
<b>Abstract</b>	<b>xi</b>
<b>Abbreviations</b>	<b>xii</b>
<b>Chapter 1 Introduction</b>	<b>1</b>
<b>Chapter 2 The Integer Quantum Hall Effect</b>	<b>7</b>
2.1 Electrons in a Magnetic Field . . . . .	7
2.2 The Quantised Hall Effect . . . . .	9
2.3 Disorder, Scaling, and Electron-Electron Interactions in 2D . . . . .	14
<b>Chapter 3 Modelling the IQHE</b>	<b>19</b>
3.1 Chalker-Coddington Network and RG Approach . . . . .	19
3.2 Random Landau Matrix Model . . . . .	23
3.3 Hamiltonian Diagonalisation . . . . .	24
<b>Chapter 4 Hartree-Fock Approximation</b>	<b>28</b>
4.1 Derivation of the HF Equations . . . . .	28

4.2	Solving the HF Equations with Spin . . . . .	35
4.3	Calculation of the Total HF Energy . . . . .	37
4.4	The Roothaan Algorithm . . . . .	38
4.5	The Level Shifting Algorithm . . . . .	43
4.6	The Optimal Damping Algorithm . . . . .	44
4.7	Convergence . . . . .	49
4.8	Further Improvements . . . . .	50
<b>Chapter 5</b>	<b>Properties of the 2DEG</b>	<b>52</b>
5.1	Density of States and Mobility . . . . .	52
5.2	Local Density of States . . . . .	56
5.3	Chemical Potential and Compressibility . . . . .	56
5.4	Participation Ratio . . . . .	58
5.5	Screening . . . . .	59
<b>Chapter 6</b>	<b>Electronic Compressibility</b>	<b>64</b>
6.1	Compressibility Patterns . . . . .	64
6.2	Coulomb Blockade . . . . .	66
6.3	Numerical Results in the $(B, n_e)$ -Plane . . . . .	69
6.4	Charge Density Distribution and Screening . . . . .	74
6.5	Breakdown of Linear Screening . . . . .	78
6.6	Compressibility Patterns in the FQHE . . . . .	83
6.7	Conclusion . . . . .	84
<b>Chapter 7</b>	<b>Conductivity</b>	<b>86</b>
7.1	Linear Response: The Kubo Formula . . . . .	88
7.2	Periodic Boundary Conditions, Berry Phase, and Conductivity . . . . .	89
7.3	Numerical Results . . . . .	93

<b>Chapter 8</b>	<b>Interaction Effects in STS Measurements</b>	<b>100</b>
8.1	Probing a 2DEG . . . . .	100
8.2	The Donor Potential . . . . .	102
8.3	The Tip Potential . . . . .	104
8.4	Numerical Results . . . . .	105
<b>Chapter 9</b>	<b>Summary and Conclusion</b>	<b>112</b>
<b>Appendix A</b>	<b>Calculation of Periodic Matrix Elements</b>	<b>116</b>
<b>Appendix B</b>	<b>Mobility</b>	<b>118</b>
<b>Appendix C</b>	<b>Commutators</b>	<b>120</b>
<b>Appendix D</b>	<b>Guiding Centre Velocity</b>	<b>121</b>
<b>Appendix E</b>	<b>Formulas Involving Landau Functions</b>	<b>123</b>

# List of Figures

1.1	Schematic sketch of a Hall bar geometry . . . . .	2
1.2	Hall conductance and longitudinal resistance schematically. . . . .	3
1.3	Measured Hall voltage . . . . .	4
1.4	Compressibility measurement of Ilani et al. . . . .	6
2.1	Schematic sketch of the $\beta$ -function for different dimensions. . . . .	16
2.2	Transition from a Wigner electron lattice to a Wigner hole lattice. . . .	18
3.1	Charge density for localised and delocalised states . . . . .	21
3.2	Chalker-Coddington network of saddle points . . . . .	22
3.3	RG structure for Chalker-Coddington network . . . . .	23
4.1	Oscillatory behaviour of the Roothaan algorithm . . . . .	41
4.2	HF-potential for two electrons during the HF iteration . . . . .	42
4.3	Convergence behaviour of three algorithms. . . . .	50
5.1	DOS at $B = 3T$ for non-interacting and interaction system . . . . .	55
5.2	Local density of states in 3D . . . . .	57
5.3	Scaling functions of the participation ratio $P_\alpha$ at $B = 3T$ . . . . .	60
5.4	Power-law fit of the system size dependence of $P_\alpha$ at $B = 3$ . . . . .	61
6.1	Measurement of the inverse electronic compressibility . . . . .	65
6.2	Spatial compressibility scans visualising localised states . . . . .	67

6.3	$\kappa^{-1}$ for a HF-interacting system as a function of position and electron density . . . . .	70
6.4	$\kappa^{-1}$ for a non-interacting system in the $(B, n_e)$ -plane . . . . .	71
6.5	$\kappa^{-1}$ for a HF-interacting system with disorder strength $W/d^2 = 1.25\text{meV}$ in the $(B, n_e)$ -plane . . . . .	72
6.6	$\kappa^{-1}$ for a HF-interacting system with disorder strength $W/d^2 = 2.5\text{meV}$ in the $(B, n_e)$ -plane . . . . .	73
6.7	$\kappa^{-1}$ for a HF-interacting system with disorder strength $W/d^2 = 3.75\text{meV}$ in the $(B, n_e)$ -plane . . . . .	74
6.8	Spatial distribution of non-interacting electron density at $\nu = 1/2$ . . . . .	75
6.9	Spatial distribution of HF-interacting electron density $\nu = 0.1$ . . . . .	77
6.10	Spatial distribution of HF-interacting electron density $\nu = 0.9$ . . . . .	78
6.11	Spatial distribution of Hartree-interacting electron density at $\nu = 1/2$ . . . . .	79
6.12	Spatial distribution of HF-interacting electron density at $\nu = 1/2$ . . . . .	80
6.13	Cross-sections of spatial distribution of HF-interacting electron density at $\nu = 0.9$ . . . . .	81
6.14	$\kappa^{-1}$ for HF-interacting system in the $(W/d^2, n_e)$ -plane . . . . .	82
7.1	Measured Hall conductance in the $(V_g, B)$ -plane . . . . .	87
7.2	$\sigma_{xy}$ for a spinless non-interacting system with disorder strength $W/d^2 = 2.5\text{meV}$ in the $(B, n_e)$ -plane . . . . .	94
7.3	$\sigma_{xy}$ for the lowest two spin levels of a HF-interacting system with disorder strength $W/d^2 = 2.5\text{meV}$ in the $(B, n_e)$ -plane . . . . .	95
7.4	$\sigma_{xy}$ for the lowest two orbital Landau levels of a HF-interacting system with disorder strength $W/d^2 = 2.5\text{meV}$ in the $(B, n_e)$ -plane . . . . .	96
7.5	Same as Figure 7.3 but with disorder strength $W/d^2 = 1.25\text{meV}$ and for a different disorder configuration . . . . .	97
7.6	Same as Figure 7.4 but with disorder strength $W/d^2 = 1.25\text{meV}$ and for a different disorder configuration . . . . .	98

7.7	$\sigma_{xy}$ for non-interacting and HF-interacting system for different disorder strengths as a function of electron density, $n_e$ . . . . .	99
8.1	Tunneling in STS measurements . . . . .	102
8.2	Effective impurity potential at $z = 0\text{nm}$ . . . . .	105
8.3	Measured and calculated LDOS for lowest four spin-split Landau levels	106
8.4	LDOS for HF-interacting system for different tip and interaction strengths	110
8.5	Measured and calculated LDOS and their Fourier transforms . . . . .	111



# Acknowledgments

I am glad to finally have the opportunity to express my gratitude to a number of people. Firstly, I am very grateful for the moral, financial, and scientific support I received generously from my supervisor Rudolf Andreas Römer, and the motivation to come to Warwick in the very first place. I am indebted to the Department of Physics for the financial support without which I wouldn't have made it. A big thanks also to Katsushi Hashimoto and Markus Morgenstern for the exciting and productive collaboration as well as numerous discussions greatly broadening my field of view. Particular gratitude goes to Alexander Croy for countless, stimulating discussions with a lot of really bright ideas I nicked off him. Furthermore, I wish to express my appreciation for many valuable discussion with Nick d'Ambrumenil, Nigel Cooper, John Chalker, Bodo Huckestein, and David Leadley. I owe credit to the Centre for Scientific Computing (especially Christine, Matt, and Grok) for the pleasant surroundings and the UK National Grid Service for catering for my outrageous needs for computing resources.

Outside the office, I would like to give a big credit to my mum for being so supportive during the years, Yoshi and Wing for the time we lived and laughed together and for introducing me to fields of research where  $\hbar$  is absurdly insignificant (ludicrous!), and of course Kristin for curing my headaches during the final year of my PhD. Ultimately, this list would be fairly incomplete without acknowledging important contributions by Lavazza, Budget Gazebos Ltd., DMR, Google, the guy who invented Japanese curry, Keith Jarrett and The Surfkings for delicious food, Linda also for delicious food, and the guy that actually invented delicious food. Thanks.

# Declarations

I hereby declare that this thesis represents my own work and to the best of my knowledge it contains no materials previously published or written by another person, nor material which to a substantial extent has been accepted for the award of any other degree at The University of Warwick or any other educational institution, except where the acknowledgement is made in the thesis. Any contribution made to the research by others, with whom I have worked at The University of Warwick or elsewhere, is explicitly acknowledged in the thesis.

Parts of this work were and will be published in conference proceedings and peer-reviewed journals:

- (i) Compressibility in the Integer Quantum Hall Effect within Hartree-Fock Approximation, C. Sohrmann and R. A. Römer, *phys. stat. sol. (c)* **3**, 334-338 (2005)
- (ii) Compressibility stripes for mesoscopic quantum Hall samples, C. Sohrmann and R. A. Römer, *New J. Phys.* **9**, 97 (2007)
- (iii) Kubo conductivity in the IQHE regime within Hartree-Fock, C. Sohrmann and R. A. Römer, submitted to *phys. stat. sol.*

- (iv) Quantum percolation in the quantum Hall regime, C. Sohrmann, J. Oswald, and R. A. Römer, invited review for "Lecture Notes in Physics" (Springer), in preparation
- (v) Interaction effects for the Integer Quantum Hall Effect, C. Sohrmann and R. A. Römer, submitted to phys. stat. sol.
- (vi) Real-space spectroscopy of Spin and Landau Levels in the Integer Quantum Hall Regime, K. Hashimoto, C. Sohrmann, M. Morgenstern, J. Wiebe, R. A. Römer, and R. Wiesendanger, in preparation

# Abstract

This thesis captures a numerical study of the interplay between disorder and electron-electron interactions within the integer quantum Hall effect, a regime where the presence of a strong magnetic field and two-dimensional confinement of the electrons profoundly affects the electronic properties. Prompted by recent novel experimental results, we particularly emphasise the behaviour of the electronic compressibility as a joint function of magnetic field and electron density, which appears to be insufficiently accounted for by the widely used independent-particle model. Our treatment of the electron-electron interactions relies on the Hartree-Fock approximation so as to achieve system sizes comparable to the experimental situation. We find numerical evidence for various interaction-mediated effects, such as non-linear screening, local charging, and  $g$ -factor enhancement. Important implications for the phase diagram may arise, although a study of the scaling of the participation ratio seems to imply a universal critical behaviour independent of interactions. Furthermore, we examine the Hall conductivity in a similar fashion, which also displayed interaction-promoted features in transport measurements. Our mesoscopic simulations only reproduce some of the observed features, suggesting the presence of effects beyond numerical tractability. Finally, we model scanning tunneling spectroscopy experiments and systematically investigate the influence of the tip induced potential as well as the interactions among the electrons. Our results show a strong dependence on the filling factor and may greatly assist the interpretation of such spectroscopy data.

# Abbreviations

		page
2DES/2DEG	Two-dimensional electron system/gas	24
DOS	Density of states	52
EOM	Equation of motion	10
FQHE	Fractional quantum Hall effect	3
HF	Hartree-Fock	28
IQHE	Integer quantum Hall effect	2
LDOS	Local density of states	56
LL	Landau level	12
LS	Level-shifting algorithm	41
MIT	Metal-to-insulator transition	5
MOSFET	Metal-oxide-semiconductor field-effect-transistor	1
ODA	Optimal damping algorithm	44
PBC	Periodic boundary conditions	11
QH	Quantum Hall	5
QD	Quantum dot	67
RHF	Restricted Hartree-Fock	34
SET	Single electron transistor	64
STS	Scanning tunneling spectroscopy	5
TDDOS	Thermodynamic density of states	52
UHF	Unrestricted Hartree-Fock	34

$i$	Imaginary unit defined by $i^2 = -1$	11
$\chi_n(x)$	Harmonic oscillator eigenfunction	12
$\varphi_{n,k}(\mathbf{r})$	Landau wave function	13
$H_n(x)$	Hermite polynomials	12
$L$	Linear dimension of square sample	13
$N_\phi$	Number of flux quanta	13
$N_{LL}$	Number of Landau levels	26
$N_e$	Number of electrons	13
$n_e(\mathbf{r})$	Charge density at position $\mathbf{r}$	27
$n_e$	Average charge density in the sample	8
$\nu$	Filling factor	13
$n_0$	Landau level density	26
$\mathbf{C}$	Matrix of eigenvectors	30
$\mathbf{C}^{\alpha,\sigma}$	Eigenvector $\alpha$ with spin $\sigma$	36
$\mathbf{D}^\sigma$	Spin dependent density matrix	31
$\partial_x$	Derivative with respect to $x$	10
$\dot{x}$	Time derivative of $x$	10
$\epsilon_F$	Fermi energy	30
$f(\epsilon)$	Fermi function defined by $f(\epsilon) = [\exp^{(\epsilon - \epsilon_F)/k_B T} + 1]^{-1}$	39
$f_\alpha$	Fermi function of state $\alpha$ , i.e. $f(\epsilon_\alpha)$	30
$\mu_B$	Bohr magneton	24
$g^*$	effective $g$ -factor	24
$m^*$	effective electron mass	10
$k_B$	Boltzmann constant	53
$l_c$	Magnetic length	12
$\tilde{\nu}$	Critical exponent	14
$\rho(E)$	Density of states at energy $E$	14
$\text{LDOS}(E, \mathbf{r})$	Local density of states at $\mathbf{r}$ and energy $E$	56

$H_{2\text{DES}}^\sigma$	Spin dependent Hamiltonian	24
$V_I$	Electron-impurity interaction	24
$V_C$	Electron-electron interaction	24
$v(\mathbf{q})$	Fourier transform of electron-electron interaction	29
$\mathcal{H}$	General Hamiltonian	26
$\mathcal{H}_{\text{e-e}}$	General electron-electron interaction Hamiltonian	26
$\mathcal{H}_{\text{e-bg}}$	General electron-background interaction Hamiltonian	26
$\mathcal{H}_{\text{bg-bg}}$	General background-background interaction Hamiltonian	26
$\mathcal{H}_0$	General one-particle Hamiltonian	26
$\mathcal{H}_1$	General two-particle Hamiltonian	26
$\gamma$	Interaction strength	25
$\zeta, \xi, \eta$	Cyclotron coordinates	11
$\mathbf{R}, X, Y$	Guiding centre coordinates	11
$\varepsilon$	Small parameter for numerical purposes	37
$\phi(\mathbf{r})$	Electrostatic potential	

# Chapter 1

## Introduction

The advent of semiconducting devices and their use in integrated circuits was nothing short of a social revolution and clearly marked the brink of a new era. Transistors and diodes became indispensable as they made their way into pretty much all areas of everyday life, opening up a world of instant communication and pervasive access to information. Solid state physics can certainly be regarded as one key player in the race for an interconnected, educated society, since technical progress especially in this field requires a thorough and profound knowledge of the underlying microscopic phenomena. Indeed, physics has come a long way ever since. Yet, our understanding is still far from complete. In this work we attempt to contribute a small bit. Using numerical methods, we focus on one particularly interesting phenomenon which triggered many new developments in condensed matter physics. In 1980, an altogether unexpected discovery was made by Klaus von Klitzing and coworkers [1] when carrying out Hall measurements on a *metal-oxide-semiconductor field-effect transistor* (MOSFET). They discovered that for a system of electrons confined to two dimensions and subject to a strong, perpendicular magnetic field,  $B$ , the resistivity tensor,  $\rho$ , and the conductivity tensor,  $\sigma$ , can freeze to the form

$$\rho = \begin{pmatrix} 0 & h/e^2 i \\ -h/e^2 i & 0 \end{pmatrix} \quad \text{and} \quad \sigma = \begin{pmatrix} 0 & -ie^2/h \\ ie^2/h & 0 \end{pmatrix}, \quad (1.1)$$



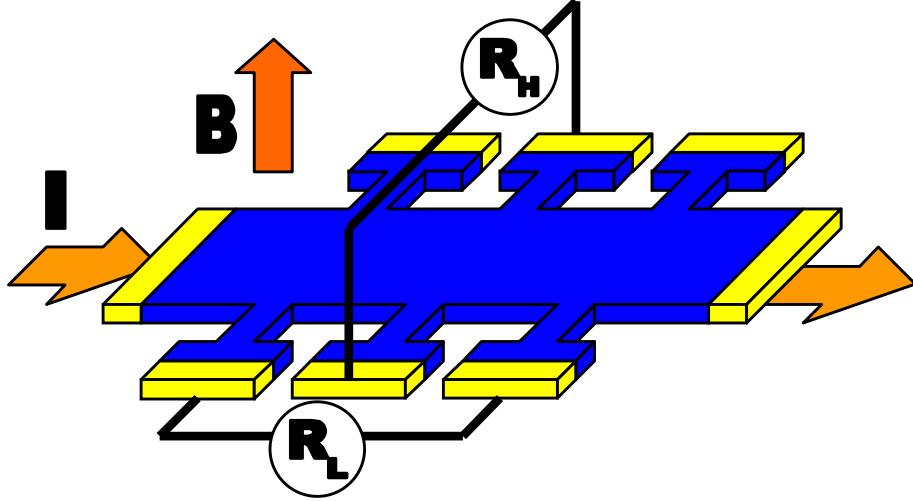


Figure 1.1: Schematic sketch of a Hall bar geometry for the measurement of the longitudinal and the Hall resistance. The current flows from the so-called source to the drain, indicated by the arrow on the left and on the right, respectively.

with  $i$  being an integer. Astonishingly, it turned out that this quantisation holds over a wide range of  $B$  or the applied voltage, forming quantised plateaus, and is completely independent of the sample geometry and choice of material. A commonly adopted geometry is, for instance, the Hall bar, as sketched in Figure 1.1. In between those plateaus, the Hall conductivity,  $\sigma_{xy}$ , performs a transition and the longitudinal conductivity,  $\sigma_{xx}$ , assumes a finite value of  $e^2/h$ , as shown schematically in Figure 1.2. This was the fruitful discovery of the *integer quantum Hall effect* (IQHE). Contrary to the classically expected linear relation between  $\rho_{xy}$  and  $B$ , this quantisation of transport sets in at very low temperatures and high sample quality. The importance of the discovery lies in the precision and resilience of the quantisation and allowed for a high precision determination of the fine structure constant, defined as  $\alpha = e^2/(2\epsilon_0 hc)$ , where  $c$  is the vacuum speed of light and  $\epsilon_0$  the vacuum permittivity. Ultimately, the IQHE was adopted as a metrological standard, defining the international reference resistance as

$$R_{K-90} = h/e^2 = 25812.807\Omega , \quad (1.2)$$

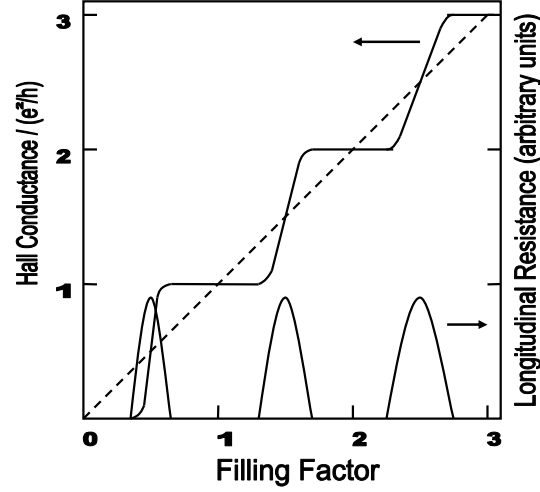


Figure 1.2: Schematic sketch of the plateau structure of the Hall conductance as well as the finite longitudinal resistance at the plateau transitions in the IQHE.

with an absolute error of  $\pm 5 \cdot 10^{-3} \Omega$  [2]. For the importance of this discovery von Klitzing was awarded the Nobel prize in 1985. The original measurements are depicted in Figure 1.3. The IQHE was soon followed by another unexpected, even more surprising finding. When carrying out Hall measurements on even cleaner samples, higher fields, and lower temperatures, Tsui, Störmer, and Gossard discovered in 1982 [3] that the Hall conductivity becomes quantised also at intermediate magnetic fields or voltages and acquires certain fractional values of  $e^2/h$ , such as  $1/3$ ,  $2/3$ ,  $2/5$ , and so on. Owing to the logic, this effect was called *fractional quantum Hall effect* (FQHE) and rewarded with a Nobel prize in 1998. Whereas the IQHE was soon motivated with a gauge argument in a non-interacting system of electrons [4], the FQHE turned out to be far more complicated and could only be explained with correlated many-body states [5] or collective excitations with fractional charge [6,7], albeit still lacking a firm, microscopic derivation. The scope of this work will be limited to the IQHE for which single-particle models [4,8–16] have successfully been able to reproduce general features such as the position and height of the plateaus. However, interactions become an essential part when trying to interpret experimental results such as recently observed patterns in the

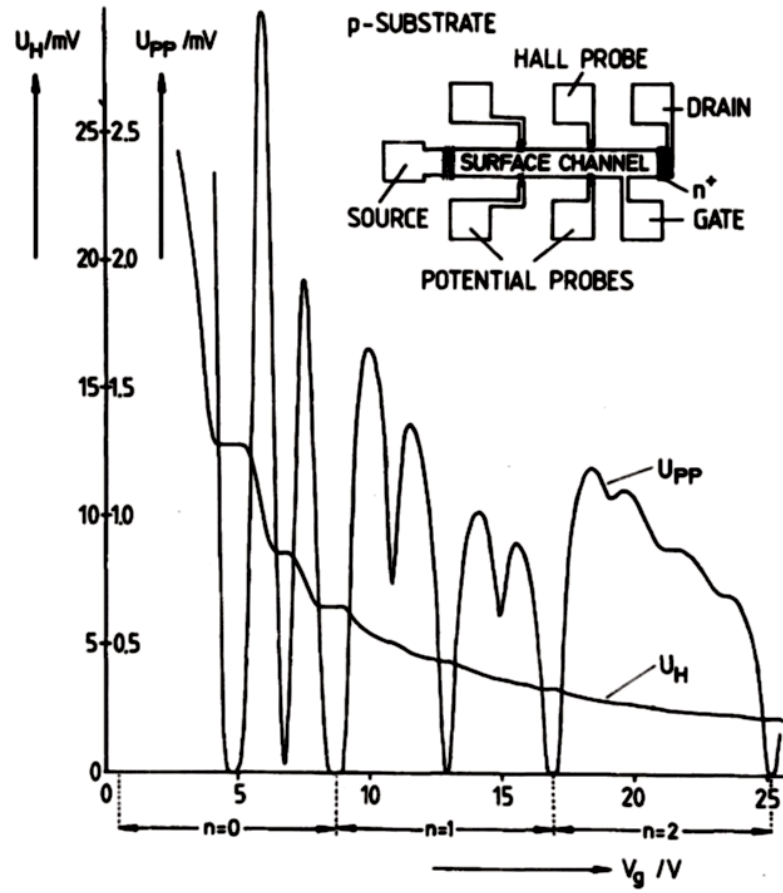


Figure 1.3: Measurement of the Hall voltage ( $U_H$ ) and longitudinal voltage ( $U_{PP}$ ) as a function of applied gate voltage, which is proportional to the electron density [1]. Wherever a plateau is formed by the Hall voltage, the longitudinal voltage drops to zero.

compressibility (see Figure 1.4) [17,18] or the conductance [19,20], enhancement of the  $g$ -factor [21], negative compressibility [22], filling factor dependence of the Landau level width [23], or the Hall insulator [24]. In this work we outline our numerical investigations of such electron-electron interaction related effects using a mean-field HF-approach and thereby neglecting higher correlations among the electrons. Since HF accounts for Thomas-Fermi screening effects while at the same time leading to a critical exponent  $\tilde{\nu}$  whose value is found to be consistent with results of non-interacting approaches [25,26], this appears to be a reasonable starting point.

We now outline the structure of this work: In **Chapter 2** we review the behaviour of electrons in the quantum Hall (QH) regime. **Chapter 3** gives a brief overview over some numerical methods which have been very successful in reproducing the main features of the integer quantum Hall effect, although mostly in a single-particle picture. In **Chapter 4**, we turn to the derivation and implementation of the HF-approximation. We discuss convergence properties of three different algorithms. In **Chapter 5** we outline important properties of two-dimensional electron systems and compare numerical results for the non-interacting and the HF-interacting case. We also touch the question of universality of the metal-to-insulator transition (MIT). In **Chapter 6** we present our numerical results on the compressibility in the  $(B, n_e)$ -plane and compare the experimental findings [17,18] with our non-interacting and HF-interacting simulations. **Chapter 7** is dedicated to further experimental evidence for electron-electron interaction effects in the IQH regime deduced from transport experiments. We derive an expression for the Hall conductivity of a HF-interacting system and present simulation results also as a joint function of  $B$  and  $n_e$ . In **Chapter 8** we focus on scanning spectroscopy microscopy (STS) experiments, where the influence of the scanning tip on the imaging data is unclear. We present a systematic investigation of how the tip potential and the electron-electron interaction affect the measured LDOS data. Finally, we summarise our results in **Chapter 9**.

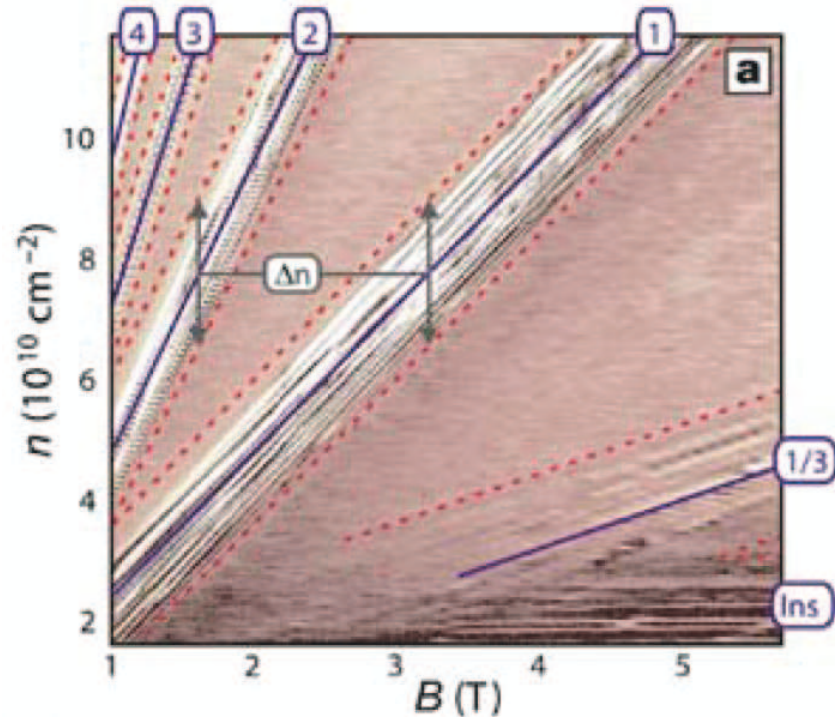


Figure 1.4: Compressibility patterns found by Ilani et al. [17] in SET measurements on high-mobility samples. The visible lines correspond to charging of strongly localised states suggesting the relevance of electron-electron interactions also in the IQH regime.

## Chapter 2

# The Integer Quantum Hall Effect

### 2.1 Electrons in a Magnetic Field

The first quantitative investigations on the behaviour of electrons in a magnetic field were carried out back in the 19th century. Edwin Hall discovered during his dissertation in 1879 [27] that when he placed a conductor in a magnetic field with a direction perpendicular to the flowing current, a voltage drop could be picked up along the direction perpendicular to both the field *and* the current. What must have come as a surprise back then was the discovery of the nowadays well-known classical Hall effect and has its origin in the Lorentz force,  $\mathbf{F}_L$ , which acts on a moving charge,  $-e$ , having velocity  $\mathbf{v}$ , subjected to a magnetic field,  $\mathbf{B}$ , as follows

$$\mathbf{F}_L = -e\mathbf{v} \times \mathbf{B} . \quad (2.1)$$

The carriers that are deflected into the direction of this Lorentz force accumulate at the edge of the sample and thereby create an induced electric field,  $\mathbf{E}_H$ , perpendicular to the current and the magnetic field. This field exerts a force,  $\mathbf{F}_H = -e\mathbf{E}_H$ , on the carriers which compensates the Lorentz force such that

$$\mathbf{F}_L + \mathbf{F}_H = 0 . \quad (2.2)$$

Hall expected his experiments to reveal a dependence of the resistivity along the current direction on the magnetic field, which he did not find due to the compensating Hall field [28]. Along the direction of this Hall field a voltage,  $U_H$ , could be measured which displayed an astonishing independence of the experimental set up [29]. How this comes about becomes clear if we relate this *Hall voltage* to the geometry and the applied current as follow. We assume the magnetic field perpendicular to the current and measure the Hall voltage in the direction of the Hall field,  $\mathbf{E}_H = \mathbf{v} \times \mathbf{B}$ , and our particular set-up gives  $|\mathbf{E}_H| = |\mathbf{v}||\mathbf{B}|$ . Now the sample can be viewed as a capacitor which obeys  $|\mathbf{E}_H| = U_H/W$ , where  $W$  is the dimension of the sample into the Hall direction. Assuming the validity of the Drude model [29], we take the current density to be

$$\mathbf{j} = -en_e\mathbf{v} , \quad (2.3)$$

where  $n_e$  is the carrier concentration, and the current  $I = A|\mathbf{j}|$  with  $A$  being the cross-section of the sample, we finally obtain

$$U_H = -\frac{I|\mathbf{B}|W}{en_eA} = A_H\frac{I|\mathbf{B}|W}{A} , \quad (2.4)$$

with the Hall coefficient for electrons,  $A_H = -(en_e)^{-1}$ . This coefficient results from microscopic sample properties and will thus only depend on the chosen material and not be affected by the experimental set-up. Therefore the Hall effect can be used to obtain information about charge transport properties such as carrier concentration or mobility of the carriers in a material. Especially the sign of the Hall coefficient (in our case a minus sign) can change if holes are involved in charge transport. This is used as a way of distinguishing electron and hole transport [30]. In electronics, the Hall effect is exploited in so-called Hall sensors which are used to determine magnetic field strengths, angles, positions, velocities, or currents [30].

For the following considerations we lift the constraint of the experimental set-up above and allow for an arbitrary direction of the current, which means that we have to switch to a tensor description for the transport parameters. We will also drop one dimension,

having transport in the two dimensional  $(x,y)$ -plane only. This is experimentally realised for instance in heterostructures, cleaved semiconductor surfaces, MOSFETs, graphene, just to name a few [31]. Now we define the tensors that link the applied field and the resulting current. We define a resistivity tensor,  $\boldsymbol{\rho}$ , and a conductivity tensor,  $\boldsymbol{\sigma}$ , as

$$\boldsymbol{\rho} = \begin{pmatrix} \rho_{xx} & \rho_{xy} \\ \rho_{yx} & \rho_{yy} \end{pmatrix} \quad \text{and} \quad \boldsymbol{\sigma} = \boldsymbol{\rho}^{-1} = \begin{pmatrix} \sigma_{xx} & \sigma_{xy} \\ \sigma_{yx} & \sigma_{yy} \end{pmatrix}, \quad (2.5)$$

where  $\sigma_{xy} = -\sigma_{yx}$  is the *Hall conductivity*,  $\rho_{xy} = -\rho_{yx}$  the *Hall resistivity*,  $\sigma_{xx} = \sigma_{yy}$  the longitudinal conductivity, and  $\rho_{xx} = \rho_{yy}$  the longitudinal resistivity. The conductivity tensors thereby describes the current response to the field,

$$\mathbf{j} = \boldsymbol{\sigma} \mathbf{E}. \quad (2.6)$$

which is Ohm's law. Hence we have as

$$\sigma_{xx} = \frac{\rho_{xx}}{\rho_{xx}^2 + \rho_{xy}^2} \quad \text{and} \quad \sigma_{xy} = -\frac{\rho_{xy}}{\rho_{xx}^2 + \rho_{xy}^2}. \quad (2.7)$$

What we have discussed so far are material parameters that are not directly accessible to measurements. The conversion from the actually measured *Hall conductance*,  $G_H$ , and *Hall resistance*,  $R_H$ , involves geometric factors such as the cross-section or the length of the sample. However, under certain circumstances, two dimensional systems are a beautiful exception. If we apply an external field  $\mathbf{E} = (E_x, 0)$ , resulting in a current  $\mathbf{j} = (j_x, 0)$ , a Hall field  $\mathbf{E}_H = (0, E_H)$  is induced. With  $U_H = E_H W$  and  $E_H = -\rho_{xy} j_x = -\rho_{xy} I / W$  obtained through Equation (2.6), we find  $U_H = -\rho_{xy} I$ , and thus  $R_H = -\rho_{xy}$ , independent of any geometry parameters. However, one assumption which remains is that the Hall voltage has to be measured precisely on opposite sites of the sample. In the following we will see under which circumstances even this becomes irrelevant for the measurement.

## 2.2 The Quantised Hall Effect

The geometric corrections usually involved in the Hall effect can be eliminated by applying a strong magnetic field, such that the *Hall angle*, defined by  $\tan \theta_H = E_H / E_x$ ,



becomes  $\theta_H \rightarrow 90^\circ$ . In this case,  $\sigma_{xx} = 0$ , and no voltage drops along the sample and therefore the Hall voltage may be picked up at two arbitrary points on the edges of the sample. Thereby making true material parameters, namely the '**-ivities**' instead of the '**-ances**', experimentally accessible. The discovery of this exceptional effect, the *integer quantum Hall effect* (IQHE), by von Klitzing was awarded with the Nobel prize in 1985.

In this section we will focus on the origin of the IQHE. Therefore we first turn back to the classical picture for a two-dimensional system with perpendicular magnetic field  $\mathbf{B} = (0, 0, B)$ . We assume the same set-up as before, where  $E_H = R_H j_x$ . Now plugging in the Drude current density from Equation (2.3), as well as  $E_H = v_x B$ , we find for the classical Hall resistance

$$R_H = \frac{B}{en_e} . \quad (2.8)$$

Thus, for a fixed carrier density, in the classical picture one would expect a linear relation between the Hall resistance and the magnetic field. It is very instructive to first study the dynamics of the electrons purely classical before we turn to a quantum mechanical description. Assuming the magnetic field again in  $z$ -direction, the classical equation of motion (EOM) reads

$$\frac{\partial^2 \mathbf{r}}{\partial t^2} = \begin{pmatrix} \ddot{r}_x \\ \ddot{r}_y \end{pmatrix} = -\frac{e}{m^*} (\mathbf{E} + \mathbf{v} \times \mathbf{B}) = -\omega_c \left[ \frac{\mathbf{E}}{B} + \begin{pmatrix} \dot{r}_y \\ -\dot{r}_x \end{pmatrix} \right] , \quad (2.9)$$

where we have introduced the frequency  $\omega_c = eB/m^*$ , the meaning of which will become clear very soon. With a field  $\mathbf{E} = (E, 0)$ , as usual, we find the solution

$$\mathbf{r}(t) = \frac{E}{\omega_c B} \begin{pmatrix} \cos \omega_c t \\ \sin \omega_c t \end{pmatrix} - \frac{E}{B} \begin{pmatrix} 0 \\ t \end{pmatrix} + \mathbf{r}_0 , \quad (2.10)$$

with the arbitrary constant of integration  $\mathbf{r}_0$ . As expected, Equation (2.10) describes a cyclotron motion with angular frequency  $\omega_c$ , which will thus be called *cyclotron frequency*, superimposed onto a drift motion into  $y$ -direction. If the cyclotron motion is very fast we can take a time average,

$$\langle \mathbf{r} \rangle_t = \lim_{\Delta \rightarrow \infty} \Delta^{-1} \int_{-\Delta/2}^{\Delta/2} dt' \mathbf{r}(t + t') , \quad (2.11)$$

and only the drift motion will remain. Thus no force is acting on the electrons on average, i.e.  $\ddot{\mathbf{r}} = 0$ , and we recover Equation (2.2).

Let's now turn to a quantum mechanical description. The stability of the plateaus strongly points to an effect due to the quantisation of the electron movement in the magnetic field. We will neglect any edge effects and study the bulk Hamiltonian for the 2D electrons, which can be written as

$$h_0 = \frac{1}{2m^*}(\mathbf{p} - e\mathbf{A})^2 = \frac{1}{2m^*}\boldsymbol{\pi}^2, \quad (2.12)$$

where  $\mathbf{p}$  is the momentum and  $\mathbf{A}$  the vector potential of the magnetic field determined by  $\mathbf{B} = \nabla \times \mathbf{A}$ . We have introduced the *canonical momentum*  $\boldsymbol{\pi} = \mathbf{p} - e\mathbf{A}$ . The choice of the vector potential will of course be irrelevant for any observable quantity, but will make a difference to the symmetry of the eigenfunctions of the Hamiltonian. For purposes of numerical implementation, a convenient choice should be according to the geometry. For a square sample with periodic boundary conditions (PBC) the Landau gauge,

$$\mathbf{A} = B(0, x)^T, \quad (2.13)$$

appears most convenient and will be employed throughout this work. Assuming a similar behaviour in the quantum case as we found for the classical case, we compute the EOM as

$$\begin{pmatrix} \dot{\pi}_x \\ \dot{\pi}_y \end{pmatrix} = \frac{i}{\hbar}[h_0, \boldsymbol{\pi}] = \omega_c \begin{pmatrix} \pi_y \\ -\pi_x \end{pmatrix}, \quad (2.14)$$

and find an equivalent expression to the classical Equation (2.9). Thus we introduce the *cyclotron coordinate*  $\boldsymbol{\zeta}$ , as well as the *guiding centre* coordinates  $\mathbf{R}$ , as

$$\boldsymbol{\zeta} = \begin{pmatrix} \xi \\ \eta \end{pmatrix} \quad \text{and} \quad \mathbf{R} = \begin{pmatrix} X \\ Y \end{pmatrix}, \quad (2.15)$$

respectively. The true electron motion can now be written as  $\mathbf{r} = \mathbf{R} + \boldsymbol{\zeta}$ . Integrating the EOM we find

$$\boldsymbol{\pi} = m\omega_c \begin{pmatrix} \eta \\ -\xi \end{pmatrix} \quad (2.16)$$

and we can write the Hamiltonian as

$$h_0 = \frac{\hbar\omega_c}{2l_c}\zeta^2 = \frac{\hbar\omega_c}{2l_c}(\eta^2 + \xi^2) . \quad (2.17)$$

Thus, the clean Hamiltonian commutes with  $\mathbf{R}$  and therefore does not lead to a drift motion. The wave functions describing the cyclotron motion can be found from the Schrödinger equation

$$h_0\varphi(\mathbf{r}) = E\varphi(\mathbf{r}) . \quad (2.18)$$

In Landau gauge  $h_0$  is independent of  $y$ , thus commutes with  $p_y = -i\hbar\partial_y$  which is therefore conserved. This also implies that  $h_0$  and  $p_y$  have common eigenstates and eigenvalues, which we call  $k_y$ . Hence for the states we immediately find  $\varphi(\mathbf{r}) = \xi(y)\chi(x)$  with  $\xi(y) = \exp[(i/\hbar)k_y y]$ . Inserting these eigenstates into the Schrödinger equation we find for the  $x$ -dependent part

$$h_0\chi(x) = \left[ -\frac{\hbar^2}{2m^*}\frac{\partial^2}{\partial x^2} - \frac{m^*\omega_c^2}{2}\left(x - \frac{k_y}{eB}\right)^2 \right] \chi(x) = E\chi(x) , \quad (2.19)$$

This is just a 1D harmonic oscillator in a quadratic potential in  $x$ -direction around the guiding centre  $X = kl_c^2$ , where we have introduced  $k = k_y/\hbar$  and the *magnetic length*  $l_c = \sqrt{\hbar/eB}$ . The frequency of the oscillation is – just as in the classical case – the cyclotron frequency  $\omega_c$ . The eigenvalue of the 1D harmonic oscillator are thus the eigenvalues of our Hamiltonian, which are given by

$$E_n = (n + 1/2)\hbar\omega_c , \quad (2.20)$$

with  $n = 0, 1, 2, \dots$  labeling the number of nodes, called the *Landau level*. Similarly we find the eigenstates as

$$\chi_n(x) = \frac{1}{\sqrt{2^n n! \sqrt{\pi} l_c}} \exp\left[-\frac{x^2}{2l_c^2}\right] H_n\left(\frac{x}{l_c}\right) , \quad (2.21)$$

with  $\chi(x) = \chi_n(x - X)$  and  $H_n(x)$  being the Hermite polynomials. We still have the freedom to choose the centre coordinate,  $X$ , which will finally be determined by the

requirement of PBCs. In a square geometry of size  $L \times L$ , the PBC in  $y$ -direction require  $\exp(ikL) = 1$  and therefore

$$k = \frac{2\pi}{L}j, \quad (2.22)$$

with  $j$  being an integer. For the centre coordinate this means  $X = (2\pi l_c^2/L)j$ , which has to lie within the geometry, i.e.  $X \in (0, L]$  and thus  $j \in [1, L^2/2\pi l_c^2]$ . By the above considerations we found the number of states per Landau level

$$N_\phi = \frac{L^2}{2\pi l_c^2}, \quad (2.23)$$

which is also the number of *magnetic flux quanta*,  $\Phi_0 = h/e$ , that penetrate the area  $L^2$  at a magnetic field  $B$ , as given by  $N_\phi = L^2 B / \Phi_0$ . This is probably not too surprising since for a spin-polarised system there can be precisely one state per flux quantum in each Landau level. In summary, the Schrödinger equation (2.18) with the magnetic Hamiltonian of Equation (2.12) in Landau gauge (2.13) is obeyed by the degenerate Landau functions [32]

$$\varphi_{n,k}(\mathbf{r}) = \langle \mathbf{r} | \varphi_{n,k} \rangle = \frac{1}{\sqrt{2^n n!} \sqrt{\pi} l_c L} \exp \left[ iky - \frac{(x - kl_c^2)^2}{2l_c^2} \right] H_n \left( \frac{x - kl_c^2}{l_c} \right), \quad (2.24)$$

with the eigenenergies  $E_n = (n + 1/2)\hbar\omega_c$ , where  $n$  labels the Landau level index and  $k = 2\pi j/L$  with  $j = 1, \dots, N_\phi$  the momentum. So far we have only taken into account the periodicity in  $y$ -direction. For the torus geometry we will adapt in this work, another modification will have to be made which we will discuss later. Now that we have determined the number of states per Landau level, it proves very useful to define a quantity that characterises the filling of the system, called the *filling factor*  $\nu$ , by

$$\nu = \frac{N_e}{N_\phi}, \quad (2.25)$$

where  $N_e$  is the *number of electrons* in the system. The spectrum of  $h_0$  consists of a sequence of  $\delta$ -peaks at energies  $E_n$ , where each energy corresponds to an  $N_\phi$ -fold degenerate state.

## 2.3 Disorder, Scaling, and Electron-Electron Interactions in 2D

In contrast, real systems will inevitably contain a certain amount of disorder due to, for instance, impurities, imperfections, or surface contamination. Having disorder in the system will lift the degeneracy by broadening the  $\delta$ -peaked Landau levels into bands. For a smooth disorder potential compared to the magnetic length, especially in the limit  $B \rightarrow \infty$ , it can be shown [33] that the eigenstates will follow equipotential lines of the disorder potential at the corresponding eigenenergies and the average density of states will then equal the overall distribution of energies in the potential, i.e.  $\rho(E) = P[V]$ . The problem of the MIT reduces to a percolation problem and it becomes clear why there is only a single extended state in a disordered 2D energy landscape [16]. The problem of whether a state is localised or extended can be captured with the *localisation length*,  $\xi(E)$ , a quantity which characterises the spatial spread of the wave function [33]. It has been shown [34] that at the MIT the localisation length diverges as a power,

$$\xi(E) = |E - E_c|^{-\tilde{\nu}} , \quad (2.26)$$

where  $\tilde{\nu}$  is the critical exponent [34]. This exponent characterises the transition and is believed to be independent of microscopic details of the impurity potential. The idea of a percolating state has been exploited in the so-called Chalker-Coddington model [14], which we will briefly review in one of the following sections. Up to today there exists no perfectly conclusive theory of the MIT in the quantum Hall regime. The existence of extended states in a 2D system was rather surprising given the fact that using a scaling theory, Wegner [35, 36] and Abrahams et al. [37] were able to argue convincingly that all states in 2D are localised. The effect of the magnetic field leads to a delocalisation at a singular energy in the centre of the Landau band. This is, however, not a true metallic phase but rather a quantum critical point that exhibits critical fluctuations [36, 38, 39]. In absence of a rigorous mathematical description of this localisation-delocalisation transition in more than one dimensions, a wealth of numerical approaches

have been stressed to provide quantitative results (see, e.g. , [34, 40–45]). However, recently an perturbative formula for the localisation length for stacked 1D chains (quasi-1D) has been given [46]. Scaling theory is a powerful tool to extract information about localisation behaviour in disordered electronic system and gives very strong qualitative results even with very few and straightforward assumption. The scaling approach for disordered system is based on the idea that the conductance of a sample,  $g(L)$ , solely depends on the conductance of a smaller part of the sample, i.e.  $g(nL) = f(n, g(L))$ , where one usually considers a hypercube in  $d$  dimensions with volume  $L^d$  [37, 47, 48]. This is called the *one-parameter scaling assumption*. For the analysis it is convenient to introduce the so-called  $\beta$ -function, essentially defined as the change of the dimensionless conductance  $g$  with changing the sample size  $L$ ,

$$\beta[g(L)] = \frac{L}{g(L)} \frac{dg(L)}{dL} = \frac{d \ln g(L)}{d \ln L} , \quad (2.27)$$

where the prefactor is introduced such that the  $\beta$ -function becomes dimensionless. Obviously, a metallic system must have  $\beta > 0$ , such that the conductivity does not vanish for  $L \rightarrow 0$ , whereas insulating behaviour will display  $\beta < 0$ . Contemplating a metallic system, Ohm's law can be applied if  $g \gg g_c$  with  $g_c \approx \pi^{-2}$  [47] and the  $\beta$ -function behaves to leading order as  $g/(e^2/\hbar) \approx \sigma L^{d-2}$ . Thus for  $g \rightarrow \infty$ , we expect  $\beta = d - 2$ . In case of an insulator, i.e.  $g \ll g_c$ , it seems reasonable to assume an exponential decay,  $g \approx g_c \exp(-L/\xi)$ , which yields  $\beta = \ln(g/g_c)$ . Hence we find the result that in 1D the  $\beta$ -function is always smaller than zero and no MIT can exist. For 3D a crossing of zero does exist and so does the MIT. The 2D case, however, is not so straightforward – even in this simple picture. For weak disorder, a perturbative expansion of  $\beta$  in  $1/g$  as the small parameter yields  $\beta = (d - 2) - c/g$  with a negative first order correction [49], implying that the  $\beta$ -function will not cross zero. Integration of the  $\beta$ -function  $dg/(d \ln L) = -c$  yields  $g = \sigma - c \ln(L/L_0)$ , which shows a logarithmic decrease of the conductivity as the system size increases. By the plausible assumption that the  $\beta$ -function is monotonic, the  $\beta$ -function can be sketched as in Figure 2.3. Scaling is of course not restricted to the conductivity. Scaling of the *localisation length*, the *participation ratio*, the *Thouless*

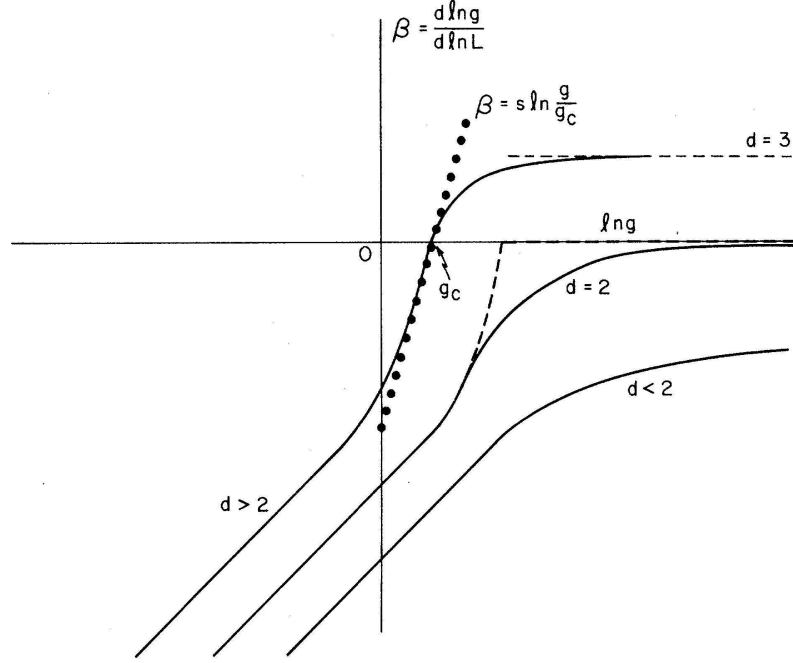


Figure 2.1: Schematic sketch of the  $\beta$ -function versus  $\ln g$  for several spatial dimensions of the system [37]. The dotted line shows the small- $g_c$  approximation for  $d > 2$ . It is argued that the dotted line is an unlikely scenario due to the smoothness requirement.

number, or the *Chern number* is also common practise in obtaining information about a system [43]. We will numerically investigate the MIT in a later chapter of this work. The one-parameter scaling assumption implies a single exponent governing the phase transition [50]. For the IQHE, Levine et al. [51] have show the breakdown of one-parameter scaling. Instead, a two-parameter scaling arises, where both,  $\sigma_{xx}$  and  $\sigma_{xy}$  scale with  $L$ . Finally we want to add that in the diffusive regime, delocalisation is enhanced in the presence of a magnetic field as compared to the  $B = 0$  case. The reason is the suppression of weak localisation [33, 49]. Considering  $B = 0$ , the return probability of an electron carrying out a diffusive motion in a disordered landscape is the square of the sum of the probability amplitudes for all possible closed paths returning to the starting point. Classically, all the cross terms between different loops would average out. In a completely phase coherent environment, however, contributions

from time-reversed paths will not average to zero but yield a contribution due to the constructive interference of these paths. Therefore the return probability increases in a phase coherent system. This effect is known as weak localisation [33]. With a vector potential present, an electron picks up a path-dependent phase along the way it travels. A time-reversed path will have a different phase back at the starting point. With this so-called broken time-reversal-symmetry the return probability is reduced and delocalisation enhanced compared to the coherent case without a vector potential. This is also true for any dephasing process, such as inelastic scattering for instance with phonons, photons, or other electrons. The question of how electron-electron interactions affect the electronic properties will be the main subject of this work. Analytical methods are sparse and usually describe a certain aspect only approximately. Numerical methods, for instance, can treat disorder and interactions exactly. Some approximations of the electron system are, however, still required. In our simulation, the underlying crystal structure will be incorporated as a renormalisation of the electron mass [49] and the interaction with crystal defects and dopants as a smooth, random disorder potential. The ions are treated as a smooth background charge providing overall charge neutrality for the system. Regarding the electron-electron interactions, it has been shown that by virtue of *super universality* and  $\mathcal{F}$  invariance, universality is retained even with interactions present [52–54]. Therefore we expect this universality to also be supported by our numerical calculations. We will, however, put more emphasis on comparisons to experimental data and expect to observe distinct differences between interacting and non-interacting model, for instance due to exchange enhanced spin splitting. In Figure 2.2 we depict the electron density of a HF-interacting system in the weak disorder limit at half filling. Crystallisation occurs and a square lattice is formed on account of the periodic boundary conditions.



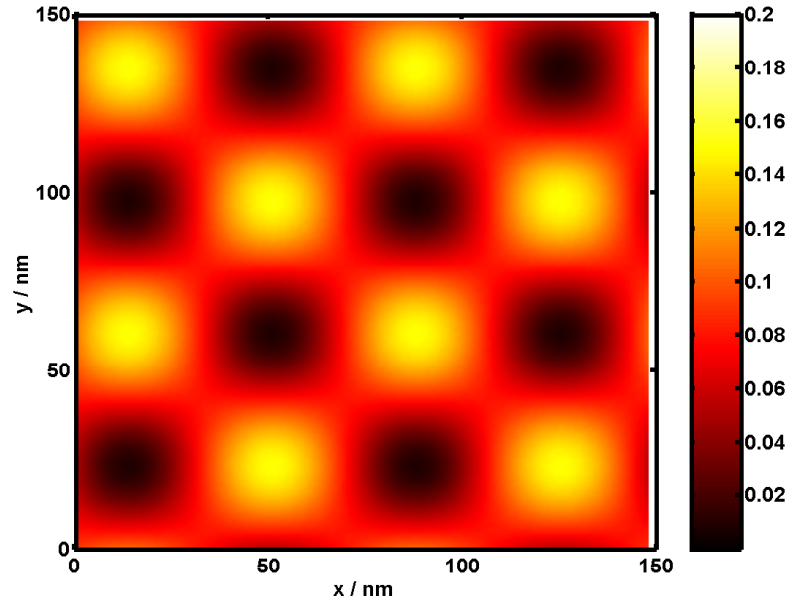


Figure 2.2: Spatial distribution of HF-interacting electron density for weak disorder at  $\nu = 1/2$ . The 2DEG forms a Wigner lattice which changes from an electron to a hole lattice. Lighter areas correspond to a high charge density whereas darker areas show low charge density. The symmetry is determined by the boundary conditions.

## Chapter 3

# Modelling the IQHE

The quest for a correct and comprehensive description of IQH physics has led to a vast number of numerical approaches and model systems. In this Chapter we want to briefly address a few interesting methods in order to give a brief overview and to explain some important features about IQH physics. These models have been used extensively for investigating universality, extracting critical exponents, or conductance distributions with high accuracy. Knowledge of the existing numerical methods is essential in choosing the correct model for a particular problem, since each model has its advantages and disadvantages. Methods that should be mentioned but which will not be discussed any further are for instance tight binding lattice models [55, 56], the transfer matrix method [57–61], the recursive Green’s function method [42], level statistics [44, 62], or Monte Carlo [63] approaches.

### 3.1 Chalker-Coddington Network and RG Approach

Probably one of the most successful numerical schemes for the IQHE is the network model introduced by Chalker and Coddington [14]. The network model is very simple and elegant in the respect that it contains only the most necessary ingredients to describe the localisation-delocalisation transition of non-interacting electrons, namely the quantum

mechanical tunneling and confinement. The basic form of the network model has a completely classical interpretation. The idea to map the IQHE onto a network can be justified most easily in the high-field limit,  $B \rightarrow \infty$ , i.e.  $l_c \rightarrow 0$ . In this limit the cyclotron radius of the electrons vanishes and the centre coordinates take the role of the ordinary spatial coordinates. In the following we want to briefly sketch the justification. We assume a Hamiltonian of the form  $H = h_0 + V(\mathbf{r})$ , where  $V(\mathbf{r})$  is a disorder potential due to the electron-impurity interaction. Furthermore, we assume the eigenstates of this Hamiltonian,  $\phi_\alpha(\mathbf{r})$ , are linear combinations of Landau states, i.e.  $\phi_\alpha(\mathbf{r}) = \sum_{n,k} C_{n,k}^\alpha \varphi_{n,k}(\mathbf{r})$ . The coefficients can be found from the Schrödinger equation,  $H|\phi\rangle = E|\phi\rangle$ , which reads in matrix form

$$\sum_{n',k'} \langle \varphi_{nk} | V | \varphi_{n'k'} \rangle C_{n',k'}^\alpha = E'_\alpha C_{n,k}^\alpha, \quad (3.1)$$

and which by virtue of the form of the matrix elements,

$$\langle \varphi_{nk} | V | \varphi_{n'k'} \rangle = \int d^2\mathbf{r} \chi_n(x - kl_c^2) V(\mathbf{r}) \chi_{n'}(x - k'l_c^2) \exp[-iy(k - k')] \quad (3.2)$$

in matrix form  $\sum_{n',k'} \langle \varphi_{nk} | V | \varphi_{n'k'} \rangle C_{n',k'}^\alpha = E'_\alpha C_{n,k}^\alpha$ . With the high-field approximation, the coupling between different Landau levels may be neglected and the problem can be solved for each level individually, i.e. the  $n$ -index can be left out of the discussion. For easier analytical treatment, the sum will be replaced by an integral, i.e.  $\sum_{k'} = (L/2\pi) \int dk'$ , and the coefficient is substituted by its Taylor expansion as  $C(k') = \exp[(k - k')d/dq]C(q)|_{q=k}$ . With some algebra [16, 64] and the limit  $l_c \rightarrow 0$ , one can state the problem as a differential equation. The solution yields parametrised orbits,  $V(X, Y(X)) = E'$  along the equipotential lines of the disorder potential at the respective eigenenergies  $E'$ . In this approximation, it becomes apparent that only states along percolating equipotential lines will be extended, which for a smooth potential is a singular energy and thus only a single state will be extended in the limit  $L \rightarrow \infty$  [16]. Thus, the problem of the IQHE can be mapped to a classical percolation problem [14].

In Figure 3.1 we show the charge density of a single state at the bottom and in the middle of the band, respectively. Evidently, the states align along equipotentials

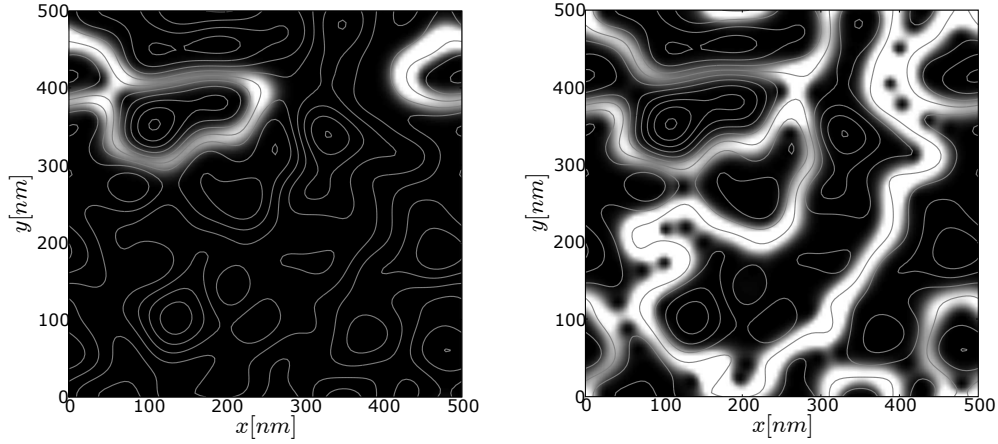


Figure 3.1: Non-interacting charge density of a single localised (left figure) and delocalised (right figure) state for a system of size  $L = 500\text{nm}$  at  $B = 6\text{T}$ . States are located at around  $\nu = 0.1$  and  $\nu = 0.5$ , respectively. The disorder potential is indicated by the equipotential lines.

of the disorder potential and thus the guiding centre approximation give a good account of the situation. The difference to the classical problem of percolation is quantum mechanical tunneling, which may allow transmission through the system away from the classically critical point. Clearly, tunneling will occur wherever different contour lines come very close. These points are the saddle points in the potential landscape. The basic idea of Chalker and Coddington was to map the saddle points of the potential to a regularly spaced network, shown in Figure 3.2, and account for tunneling by a quantum mechanical scattering matrix at each node. A clear requirement of the model is a smoothly varying potential according to  $|\nabla V(\mathbf{r})| \ll \hbar\omega_c/l_c$ . In the original model [14], each node has two incoming and two outgoing links. The presence of the magnetic field requires a unique flow direction and thus imposes a certain chirality on the nodes, depicted on the right hand side of Figure 3.2. The randomness is incorporated as a random phase the electron acquires when being scattered at a node. This accounts for the mapping of random distances to the regular network. One can then construct an overall transfer matrix from the individual nodes. The Chalker-Coddington network

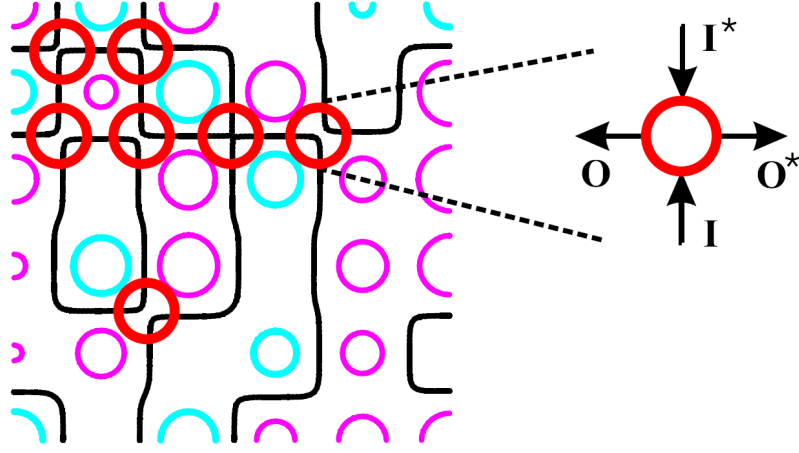


Figure 3.2: Chalker-Coddington network of saddle points [65]. The black lines indicate equipotential lines in the disordered landscape. The red circles indicate saddle points wherever the equipotential lines come close to each other. They are modeled as scatterers connecting two incoming and two outgoing waves. The nodes are eventually linked up to form a network. Right: Saddle point represented as a scatterer connecting two incoming with two outgoing channels. Purple and blue circles are potential extrema.

has been successfully employed to determine the localisation length exponent, yielding a value of  $\nu = 2.5 \pm 0.5$  [14], in agreement with other methods [16]. A renormalisation scheme has moreover been introduced [44, 66], which avoids the computation of the transfer matrix of the entire network that are replaced by a smaller ensemble of nodes, called a *super node*, as depicted in Figure 3.3. This super node is then renormalised by putting the result back into each of the nodes, thus constructing a new super node, and the procedure is repeated until the physical quantities have converged. With this scheme very large system sizes can be achieved conveniently using a few nodes only. This method yields a very accurate value for the critical exponent of  $\nu = 2.39 \pm 0.01$  [65]. The idea of tunneling at saddle points remains a useful concept even in the presence of correlations among the electrons [67], and may for instance be used in an effective description of highly correlated states, as in the FQHE [68].

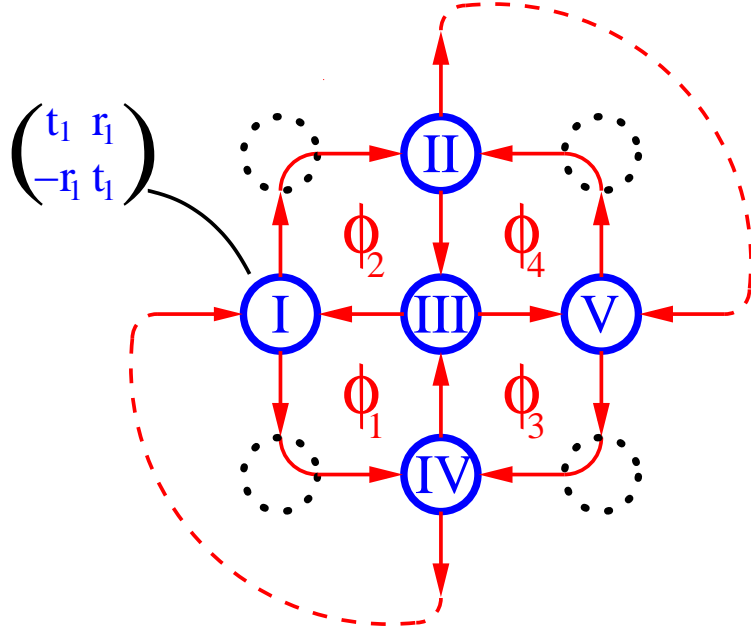


Figure 3.3: Renormalisation-group structure (super node) for the Chalker-Coddington network [65] consisting of five individual nodes. Blue nodes indicate individual scatterers. The dotted nodes are neglected such that five super nodes can be joined together. Dashed lines indicate boundary conditions.

## 3.2 Random Landau Matrix Model

The random Landau matrix (RLM) method may be classified as a statistical approach to IQHE physics [34, 69]. It is based on the argument that the full amount of underlying microscopic information is inessential for the physics and the observed electronic behaviour. It is argued that the phase transition associated with the IQHE is captured by a few statistical properties of the disorder potential only, such as the correlation function  $\langle V(\mathbf{r})V(\mathbf{r}') \rangle_{\text{ensemble}}$ . Then the system is sufficiently described by a matrix obeying the correct statistics, namely  $\langle \mathbf{V}_{k_1, n_1; k_2, n_2} \mathbf{V}_{k_3, n_3; k_4, n_4} \rangle_{\text{ensemble}}$  with the matrix elements  $\mathbf{V}_{k, n; k', n'} = \langle \varphi_{k, n} | V | \varphi_{k', n'} \rangle$ . In this approach the correlation between the matrix elements is explicitly computed, and then decomposed such that the individual matrix elements obey precisely this correlation. The advantage of the method is the restriction

to the relevant information while at the same time providing access to a whole class of systems. For instance by introducing a parameter for the correlation length of the potential, the RLM can be tuned smoothly from a white noise limit to a slowly varying disorder potential [69]. The construction of the RLM can be very efficient in terms of computational complexity. However, for the purpose of this work, where sample-specific, microscopic properties are of importance, this method is unfortunately unsuitable due to its purely statistical character.

### 3.3 Hamiltonian Diagonalisation

A diagonalisation of the complete Hamiltonian may be regarded as one of the less effective method in terms of computational efficiency. On the other hand, very few assumptions are needed and therefore one usually refers to such calculations as "ab initio" calculations. One is, however, faced with the problem of choosing a suitable basis in which the Hamiltonian has to be represented. After calculating the matrix elements of the Hamiltonian in these basis states, a diagonalisation is performed, in most cases numerically. This method offers perhaps the most flexibility. In addition to universal properties obtained by averaging over different ensemble configurations, one has direct access to microscopic properties of the 2DES for each disorder realisation. Therefore this method seems most natural for the purpose of modeling an experimental situation and will be used in this work. In order to model a high-mobility heterostructure in the QH regime, we again consider a 2DES in the  $(x, y)$ -plane subject to a perpendicular magnetic field  $\mathbf{B} = B\mathbf{e}_z$ . A single electron in such a system can be described by a Hamiltonian of the form

$$H_{2\text{DES}}^\sigma = h^\sigma + V_C = \frac{(\mathbf{p} - e\mathbf{A})^2}{2m^*} + \frac{\sigma g^* \mu_B B}{2} + V_I(\mathbf{r}) + V_C(\mathbf{r}, \mathbf{r}') , \quad (3.3)$$

where  $\sigma = \pm 1$  is a spin degree of freedom,  $V_I$  is a smooth random potential modeling the effect of the electron-impurity interaction,  $V_C$  represents the electron-electron interaction term and  $m^*$ ,  $g^*$ , and  $\mu_B$  are the effective electron mass,  $g$ -factor, and Bohr magneton,

respectively. In order to avoid edge effects we impose a torus geometry of size  $L \times L$  onto the system [70]. The electron-impurity interaction is modeled by an electrostatic potential due to a remote impurity density separated from the plane of the 2DES by a spacer-layer of thickness  $d$ , as found for instance in modulation-doped GaAs-GaAlAs heterojunctions [71, 72]. Within the plane of the 2DES, this creates a random, spatially correlated potential with a typical length scale  $d$ . We use  $N_I$  Gaussian-type "impurities", randomly distributed at  $\mathbf{r}_s$ , with random strengths  $w_s \in [-W, W]$ , and a fixed width  $d$ , such that  $V_I(\mathbf{r}) = \sum_{s=1}^{N_I} (w_s/\pi d^2) \exp[-(\mathbf{r} - \mathbf{r}_s)^2/d^2] = \sum_{\mathbf{q}} V_I(\mathbf{q}) \exp(i\mathbf{q} \cdot \mathbf{r})$  with

$$V_I(\mathbf{q}) = \sum_{s=1}^{N_I} \frac{w_s}{L^2} \exp\left(-\frac{d^2|\mathbf{q}|^2}{4} - i\mathbf{q} \cdot \mathbf{r}_s\right), \quad (3.4)$$

where  $q_{x,y} = 2\pi j/L$  and  $j = -N_\phi, -N_\phi - 1, \dots, N_\phi$ . The areal density of impurities therefore is given by  $n_I = N_I/L^2$ . The limit  $d \rightarrow 0$  yields a potential of  $\delta$ -type that would be more adequate for modeling low-mobility structures [31, 73]. The electron-electron interaction potential has the form  $V_C(\mathbf{r}, \mathbf{r}') = \gamma e^2/4\pi\epsilon_0|\mathbf{r} - \mathbf{r}'| = \sum_{\mathbf{q}} V_C(\mathbf{q}) \exp[i\mathbf{q} \cdot (\mathbf{r} - \mathbf{r}')] ,$  with

$$V_C(\mathbf{q}) = \frac{e^2}{4\pi\epsilon_0 l_c} \frac{\gamma}{N_\phi |\mathbf{q}| l_c}. \quad (3.5)$$

The parameter  $\gamma$  will allow to continually adjust the interaction strength;  $\gamma = 1$  corresponds to the bare Coulomb interaction. Choosing the vector potential in Landau gauge,  $\mathbf{A} = Bx\mathbf{e}_y$ , the kinetic part of the Hamiltonian is diagonal in the Landau functions [32] of Equation (2.24), as we derived earlier in Section 2.2. These functions are extended and  $L$ -periodic in  $y$ -direction and localised in  $x$  direction. In the following chapter we discuss the treatment of the electron-electron interaction in detail. For completeness we now briefly focus on the single particle basis states suitable for diagonalising the Hamiltonian. The system's many-body state,  $|\Phi\rangle$ , is assumed to be an anti-symmetrised product of single particle wave-functions  $\psi_\alpha^\sigma(\mathbf{r})$  (Slater determinant) [74, 75], which we choose as a linear combination of Landau states

$$\psi_\alpha^\sigma(\mathbf{r}) = \sum_{n=0}^{N_{LL}-1} \sum_{k=0}^{N_\phi-1} \mathbf{C}_{n,k}^{\alpha,\sigma} \chi_{n,k}(\mathbf{r}), \quad (3.6)$$



with  $N_{LL}$  being the number of Landau levels and the periodic Landau functions

$$\chi_{n,k}(\mathbf{r}) = \sum_{j=-\infty}^{\infty} \varphi_{n,k+jL/l_c^2}(\mathbf{r}), \quad (3.7)$$

in order to meet the boundary conditions. The number of flux quanta piercing the 2DES of size  $L \times L$  is given by  $N_\phi = L^2/2\pi l_c^2$ , yielding a total number of  $M = N_{LL}N_\phi$  states per spin direction. The filling of the system is characterised by the filling factor  $\nu = N_e/N_\phi$ , with  $N_e$  being the number of electrons in the system and areal density  $n_e = N_e/L^2$ . The total Landau level density is given by  $n_0 = eB/h$ . One problem arises, however, when using the bare Coulomb term of Equation 3.5. The Fourier transform describes an infinitely replicated system whose interaction energy tends to infinity [76]. This effect is condensed in the  $\mathbf{q} = 0$  term which leads to a divergence and has to be handled with care [77]. We can make some progress by investigating the interaction of the 2DEG with the background. The Hamiltonian is split into a one and a two-electron part as follows,

$$\mathcal{H} = \mathcal{H}_0 + \mathcal{H}_1. \quad (3.8)$$

The two-electron part can be further decomposed as

$$\mathcal{H}_1 = \mathcal{H}_{e-e} + \mathcal{H}_{e-bg} + \mathcal{H}_{bg-bg}, \quad (3.9)$$

where the electron-background, and the background-background interaction. For the Hartree case this interaction Hamiltonian can be written as

$$\mathcal{H}_1 = \frac{1}{2} \int \int d^2\mathbf{r} d^2\mathbf{r}' \left[ \frac{n_e(\mathbf{r})n_e(\mathbf{r}')}{|\mathbf{r} - \mathbf{r}'|} + 2 \frac{n_e(\mathbf{r})n_{bg}(\mathbf{r}')}{|\mathbf{r} - \mathbf{r}'|} + \frac{n_{bg}(\mathbf{r})n_{bg}(\mathbf{r}')}{|\mathbf{r} - \mathbf{r}'|} \right] \quad (3.10)$$

$$= \frac{1}{2} \sum_{\mathbf{q}} v(\mathbf{q}) [n_e(\mathbf{q})n_e(-\mathbf{q}) + 2n_e(\mathbf{q})n_{bg}(-\mathbf{q}) + n_{bg}(\mathbf{q})n_{bg}(-\mathbf{q})]. \quad (3.11)$$

Assuming a homogeneous background charge distribution,  $n_{\text{bg}}(\mathbf{r}) = -eN_e/L^2$ , with the Fourier transform  $n_{\text{bg}}(\mathbf{q}) = -e^2N_e/L^2\delta_{\mathbf{q},0}$ , the Hamiltonian becomes

$$\mathcal{H}_1 = \frac{1}{2} \sum_{\mathbf{q}} v(\mathbf{q}) \left[ n_e(\mathbf{q})n_e(-\mathbf{q}) - 2n_e(\mathbf{q})\frac{eN_e}{L^2}\delta_{\mathbf{q},0} + \frac{e^2N_e^2}{L^4}\delta_{\mathbf{q},0} \right] \quad (3.12)$$

$$= \frac{1}{2} \sum_{\mathbf{q}} v(\mathbf{q}) \left[ n_e(\mathbf{q})n_e(-\mathbf{q}) - \frac{e^2N_e^2}{L^4}\delta_{\mathbf{q},0} \right] \quad (3.13)$$

$$= \frac{1}{2} \sum_{\mathbf{q} \neq 0} v(\mathbf{q})n_e(\mathbf{q})n_e(-\mathbf{q}) . \quad (3.14)$$

Thus, for a system of interacting electrons the interaction with and among the neutralising background charge exactly cancels the divergent  $\mathbf{q} = 0$  term, which is a consequence of the Fourier transform that replicates the unit cell infinitely. In conclusion, unless  $L \rightarrow \infty$ , a neutralising background charge is required to prevent the Coulomb energy from diverging.

## Chapter 4

# Hartree-Fock Approximation

In the following we will introduce the theory of Hartree-Fock (HF) [78], which is an effective one-particle mean-field approximation to the full many-body problem. In order to treat interacting electron systems on the mesoscopic or even macroscopic scale, an approximation to the immensely time-consuming many-body problem is imperative. Hartree-Fock theory provides such an approximation which allows for reasonable system sizes and at the same time giving a good quantitative account of most effects due to the interactions [79–82]. The theory has been reviewed as well as refined as early as 1951 by Roothaan in the article [78]. Up to today HF theory is successfully employed to numerous problems in solid state physics or quantum chemistry [75,83]. In this Chapter we will derive the HF-equations adapted to our system, and discuss the questions of convergence and efficient computation.

### 4.1 Derivation of the HF Equations

There exist several ways of deriving the HF equation. A very neat and appealing approach is based on a hierarchical construction of the reduced density matrices of the full many-body problem [84–87]. We will, however, describe the variational approach which is more often referred to [28,29,88]. Therefore we start by writing down the exact many-body

Hamiltonian for the electron-electron interaction  $V(\mathbf{r}, \mathbf{r}')$  in terms of the field operators,

$$\hat{\psi}^\dagger(\mathbf{r}) = \sum_{\alpha} \psi_{\alpha}^*(\mathbf{r}) \hat{a}_{\alpha}^{\dagger}, \quad \text{and} \quad \hat{\psi}(\mathbf{r}) = \sum_{\alpha} \psi_{\alpha}(\mathbf{r}) \hat{a}_{\alpha}, \quad (4.1)$$

where  $\hat{a}_{\alpha}^{\dagger}$  and  $\hat{a}_{\alpha}$  creates and annihilates an electron in state  $\alpha$ , respectively. The interaction Hamiltonian which reads

$$\mathcal{H}_{e-e} = \frac{1}{2} \iint d^2\mathbf{r} d^2\mathbf{r}' \hat{\psi}^\dagger(\mathbf{r}) \hat{\psi}^\dagger(\mathbf{r}') V(\mathbf{r}, \mathbf{r}') \hat{\psi}(\mathbf{r}') \hat{\psi}(\mathbf{r}) \quad (4.2)$$

can thus be rewritten as

$$\mathcal{H}^{e-e} = \frac{1}{2} \sum_{\alpha\beta\vartheta\delta} F_{\alpha\beta\vartheta\delta} \hat{a}_{\alpha}^{\dagger} \hat{a}_{\vartheta}^{\dagger} \hat{a}_{\delta} \hat{a}_{\beta}, \quad (4.3)$$

where we have introduced

$$F_{\alpha\beta\vartheta\delta} = \iint d^2\mathbf{r} d^2\mathbf{r}' \psi_{\alpha}^*(\mathbf{r}) \psi_{\vartheta}^*(\mathbf{r}') V(\mathbf{r}, \mathbf{r}') \psi_{\delta}(\mathbf{r}') \psi_{\beta}(\mathbf{r}). \quad (4.4)$$

Assuming translational invariance of the interaction, as for the Coulomb interaction, i.e.  $V(\mathbf{r}, \mathbf{r}') = V(\mathbf{r} - \mathbf{r}')$ , we can insert the Fourier transform

$$V(\mathbf{r} - \mathbf{r}') = \sum_{\mathbf{q}} v(\mathbf{q}) e^{i\mathbf{q}(\mathbf{r}-\mathbf{r}')} , \quad (4.5)$$

and we get

$$F_{\alpha\beta\vartheta\delta} = \sum_{\mathbf{q}} v(\mathbf{q}) \langle \psi_{\alpha} | e^{i\mathbf{q}\mathbf{r}} | \psi_{\beta} \rangle \langle \psi_{\vartheta} | e^{-i\mathbf{q}\mathbf{r}} | \psi_{\delta} \rangle . \quad (4.6)$$

In the case of Coulomb interactions,  $v(\mathbf{q})$  is given as

$$v(\mathbf{q}) = \int \frac{d^2\mathbf{r}}{L^2} V(\mathbf{r} - \mathbf{r}') e^{-i\mathbf{q}\mathbf{r}} = \frac{c}{N_{\phi} |\mathbf{q}| l_c}, \quad \text{with} \quad c = \frac{e^2}{4\pi\epsilon\epsilon_0 l_c}. \quad (4.7)$$

So far we still have a full many-body problem where the number of possible states with  $N_e$  electrons is  $\binom{N_{\phi}}{N_e}$ . This means  $\binom{20}{5} = 15504$  many-body states for 5 electrons in a system with 20 flux quanta. Thus, it is evident that an approximation is needed. For HF, we assume the system to be in its many-body ground state and thereby reduce the

size of the basis to  $N_\phi$ . We write the many-body state  $|\Phi\rangle$  as a Slater determinant, an anti-symmetrised product of single particle states,

$$|\Phi\rangle = \prod_{\eta}^{\epsilon_\eta \leq \epsilon_F} \hat{a}_\eta^\dagger |0\rangle, \quad (4.8)$$

where  $|0\rangle$  is the vacuum, and  $\epsilon_F$  the Fermi level. Next, we find those wave functions,  $\psi_\alpha(\mathbf{r})$ , which are a minimiser of the total energy in the ground state. This energy is given as

$$\langle \Phi | \mathcal{H}_{e-e} | \Phi \rangle = \langle \mathcal{H} \rangle = \frac{1}{2} \sum_{\alpha\beta\vartheta\delta} F_{\alpha\beta\vartheta\delta} \langle \hat{a}_\alpha^\dagger \hat{a}_\vartheta^\dagger \hat{a}_\delta \hat{a}_\beta \rangle \quad (4.9)$$

$$= \frac{1}{2} \sum_{\alpha\beta\vartheta\delta} F_{\alpha\beta\vartheta\delta} f_\alpha f_\vartheta (\delta_{\alpha\beta} \delta_{\vartheta\delta} - \delta_{\alpha\delta} \delta_{\beta\vartheta}) \quad (4.10)$$

$$= \frac{1}{2} \sum_{\alpha\vartheta} f_\alpha f_\vartheta (F_{\alpha\alpha\vartheta\vartheta} - F_{\alpha\vartheta\vartheta\alpha}). \quad (4.11)$$

where  $\delta_{\alpha\beta}$  is the Kronecker delta and  $f_\alpha$  is the Fermi function. In the following we will chose a basis in which we expand the eigenstates. The clean Hamiltonian without interactions is diagonal in the Landau functions  $|\varphi_{n,a}\rangle$  of (2.24) and we choose the ansatz of linear combinations of Landau states,

$$|\psi_\alpha\rangle = \sum_{n=0}^{N_{LL}-1} \sum_{a=1}^{N_\phi} \mathbf{C}_{n,a}^\alpha |\varphi_{n,a}\rangle \quad \text{and} \quad \langle \psi_\alpha | = \sum_{n=0}^{N_{LL}-1} \sum_{a=1}^{N_\phi} \mathbf{C}_{n,a}^{\alpha *} \langle \varphi_{n,a} | \quad (4.12)$$

where the normalisation condition implies the unitarity of the matrix  $\mathbf{C}$ , i.e.

$$\sum_{n=0}^{N_{LL}-1} \sum_{a=1}^{N_\phi} \mathbf{C}_{n,a}^{\alpha *} \mathbf{C}_{n,a}^\beta = \delta_{\alpha,\beta}. \quad (4.13)$$

Using the expansion we find for the ground state energy

$$\langle \mathcal{H}_{e-e} \rangle = \frac{1}{2} \sum_{\alpha\vartheta} \sum_{n,m,n',m'} \sum_{k,l,k',l'} f_\alpha f_\vartheta \mathbf{C}_{n,k}^{\alpha *} \mathbf{C}_{n',k'}^\alpha \mathbf{C}_{m,l}^{\vartheta *} \mathbf{C}_{m',l'}^\vartheta \left( G_{n,k;n',k'}^{m,l;m',l'} - G_{n,k;m',l'}^{m,l;n',k'} \right) \quad (4.14)$$

where

$$G_{n,k;n',k'}^{m,l;m',l'} = \sum_{\mathbf{q}} v(\mathbf{q}) \langle \varphi_{n,k} | e^{i\mathbf{q}\mathbf{r}} | \varphi_{n',k'} \rangle \langle \varphi_{m,l} | e^{-i\mathbf{q}\mathbf{r}} | \varphi_{m',l'} \rangle. \quad (4.15)$$

The basic idea of HF is now to find expansion coefficients which minimise the total energy. By applying the variational principle, we can find an eigenvalue equation to determine the matrix  $\mathbf{C}$ . Thereby the orthonormality, i.e.  $\sum_n \mathbf{C}_{\mu n}^* \mathbf{C}_{\mu n} = 1$  has to be taken care of as a constraint in the optimisation procedure. For the sake of clarity we will omit the Landau level indices in the further derivation and use the Latin indices as double-indices to indicate both momentum *and* level index. The variational equation now reads

$$\sum_{\mu m} \frac{\delta}{\delta \mathbf{C}_m^\mu} \left[ \langle \mathcal{H}_{e-e} \rangle - \lambda_\mu \left( \sum_n \mathbf{C}_n^\mu * \mathbf{C}_n^\mu - 1 \right) \right] \delta \mathbf{C}_m^\mu = 0 . \quad (4.16)$$

The coefficients and their complex conjugates can thereby be treated as independent variables, which follows from the independence of the real and imaginary parts. Therefore we focus on one of the two,

$$\begin{aligned} \sum_{\mu m} \left[ \frac{1}{2} \sum_{\alpha \vartheta} f_\alpha f_\vartheta \sum_{abcd} \mathbf{C}_a^\alpha * \mathbf{C}_c^\vartheta * \left( \delta_{\mu\alpha} \delta_{mb} \mathbf{C}_d^\vartheta + \delta_{\mu\vartheta} \delta_{md} \mathbf{C}_b^\alpha \right) \left( G_{a;b}^{c;d} - G_{a;d}^{c;b} \right) \right. \\ \left. - \lambda_\mu \mathbf{C}_m^\mu * \right] \delta \mathbf{C}_m^\mu = 0 . \end{aligned} \quad (4.17)$$

The complex conjugate is derived in the same way. The two terms in the first bracket are equal and by summing over  $\vartheta$  and  $d$  we get

$$\sum_{\mu m} \left[ \sum_\alpha f_\alpha \sum_{abc} \mathbf{C}_a^\alpha * \mathbf{C}_b^\alpha \mathbf{C}_c^\mu * \left( G_{a;b}^{c;m} - G_{a;m}^{c;b} \right) - \lambda_\mu \mathbf{C}_m^\mu * \right] \delta \mathbf{C}_m^\mu = 0, \quad (4.18)$$

which can only hold if the terms in angular brackets vanish identically. From here onwards we will not use double-indices anymore and write out the Landau level explicitly. Introducing the density matrix

$$\mathbf{D}_{n,a;m,b} = \sum_\alpha f_\alpha \mathbf{C}_{n,a}^\alpha \mathbf{C}_{m,b}^{\alpha *} \quad (4.19)$$

we find the HF equations which determine the matrix  $\mathbf{C}$  optimally with respect to the total ground state energy as

$$\sum_{n',k'} \sum_{l',m',l,m} \mathbf{D}_{m,l;m',l'}^{\sigma'} \left( G_{n,k;n',k'}^{m,l;m',l'} - G_{n,k;m',l'}^{m,l;n',k'} \right) \mathbf{C}_{n',k'}^{\mu *} = \lambda_\mu \mathbf{C}_{n,k}^{\mu *} . \quad (4.20)$$

This equation is a self-consistent eigenvalue equation for determining  $\mathbf{C}$ , which thus has to be solved iteratively until convergence. However, the problem of constructing the matrix according to this equation is the memory requirement as well as the complexity. The complexity of constructing  $G$  is  $\mathcal{O}(N_{\text{LL}}N_\phi^4)$  or  $\mathcal{O}(N_{\text{LL}}L^8)$  in terms of the system size, which is rather impractical if  $N_\phi$  becomes much bigger than 100. Therefore we have to simplify the evaluation of  $G$ , which can be done using the knowledge of the basis functions as follows. The Landau states are again given by Equation 2.24. For simplicity we will work in magnetic units from here onwards, i.e.  $l_c = 1$ . Thus, any length is given in units of  $l_c$  and any momentum in  $l_c^{-1}$ . The matrix elements of the plane waves hence read

$$\begin{aligned} \langle \varphi_{n,i} | \exp(\mathbf{i}\mathbf{q} \cdot \mathbf{r}) | \varphi_{m,j} \rangle &= \frac{1}{L\sqrt{2^{n+m}n!m!\pi}} \times \\ &\int d^2\mathbf{r} \exp \left[ \mathbf{i}\mathbf{q} \cdot \mathbf{r} + \mathbf{i}(k_j - k_i)y - \frac{1}{2}(x - k_i)^2 - \frac{1}{2}(x - k_j)^2 \right] H_n(x - k_i) H_m(x - k_j) . \end{aligned} \quad (4.21)$$

After carrying out the Fourier transform in  $y$ -direction and substitution of  $x = z + K_+$  where  $K_\pm = (k_i \pm k_j)/2$  we find

$$\begin{aligned} \langle \varphi_{n,i} | \exp(\mathbf{i}\mathbf{q} \cdot \mathbf{r}) | \varphi_{m,j} \rangle &= \frac{1}{\sqrt{2^{n+m}n!m!\pi}} \delta'_{q_y, 2K_-} \exp \left( -K_-^2 + \mathbf{i}q_x K_+ - \frac{q_x^2}{4} \right) \times \\ &\int_{-\infty}^{\infty} dz \exp \left[ - \left( z - \frac{\mathbf{i}q_x}{2} \right)^2 \right] H_n(z - K_-) H_m(z + K_-) \end{aligned} \quad (4.22)$$

where the  $\delta'$ -function is a periodic Kronecker delta function as given in Appendix E. With the substitution  $x = z + \mathbf{i}q_x/2$  this yields a standard integral (see Formula 7.377 in [89]) that can be solved analytically. After some manipulation we find for  $m \leq n$

$$\langle \varphi_{n,i} | \exp(\mathbf{i}\mathbf{q} \cdot \mathbf{r}) | \varphi_{m,j} \rangle = \delta'_{q_y, k_i - k_j} \sqrt{\frac{2^n m!}{2^m n!}} \exp \left[ -\frac{\mathbf{q}^2}{4} + \frac{\mathbf{i}}{2} q_x (k_i + k_j) \right] \times \quad (4.24)$$

$$\left( \frac{\mathbf{i}q_x - q_y}{2} \right)^{n-m} L_m^{n-m} \left( \frac{\mathbf{q}^2}{2} \right) , \quad (4.25)$$

and for  $m > n$ ,

$$\langle \varphi_{n,i} | \exp(i\mathbf{q} \cdot \mathbf{r}) | \varphi_{m,j} \rangle = \delta'_{q_y, k_i - k_j} \sqrt{\frac{2^m n!}{2^n m!}} \exp \left[ -\frac{\mathbf{q}^2}{4} + \frac{i}{2} q_x (k_i + k_j) \right] \times \quad (4.26)$$

$$\left( \frac{i q_x + q_y}{2} \right)^{m-n} L_n^{m-n} \left( \frac{\mathbf{q}^2}{2} \right), \quad (4.27)$$

where  $L_n^a(x)$  is the generalised Laguerre polynomial. Now we can simplify the computation of the spinless *Fock matrix*,  $\mathbf{F}$ , which reads as

$$\mathbf{F}_{n,k;n',k'} = \sum_{l,m,l',m'} \left( G_{n,k;n',k'}^{m,l;m',l'} - G_{n,k;m',l'}^{m,l;n',k'} \right) \mathbf{D}_{m',l';m,l}, \quad (4.28)$$

where the first term (Hartree term) corresponds to the classical Coulomb repulsion and the second (Fock term) to the quantum mechanical exchange interaction, the only other two-particle correlation effect. Using Equation (4.25) we can introduce

$$M_K^{n,n',m,m'}(q_y) = \sum_{q_x} v(\mathbf{q}) \sqrt{\frac{2^n n'!}{2^{n'} n!}} \sqrt{\frac{2^m m'!}{2^{m'} m!}} \exp \left( -\frac{\mathbf{q}^2}{2} + \frac{i}{2} q_x K \right) \times \\ \left( \frac{i q_x - q_y}{2} \right)^{n-n'} \left( \frac{-i q_x + q_y}{2} \right)^{m-m'} L_{n'}^{n-n'} \left( \frac{\mathbf{q}^2}{2} \right) L_{m'}^{m-m'} \left( \frac{\mathbf{q}^2}{2} \right) \quad (4.29)$$

where due to the exponential decay we can restrict the sum over  $q_x$  as

$q_x^2 < \max[0, -2 \ln(\epsilon) - q_y]$ , with an accuracy  $\epsilon$ . Now we can write the Hartree term as

$$\sum_{l,m,l',m'} G_{n,k;n',k'}^{m,l;m',l'} \mathbf{D}_{m',l';m,l} \quad (4.30)$$

$$= \sum_{l,m,l',m'} \mathbf{D}_{m',l';m,l} \sum_{q_y} \delta'_{q_y, k-k'} \delta'_{q_y, l'-l} M_{k+k'-l-l'}^{n,n',m,m'}(q_y) \quad (4.31)$$

$$= \sum_{l,m,m'} \mathbf{D}_{m',l+k-k';m,l} M_{2(k'-l)}^{n,n',m,m'}(k-k'), \quad (4.32)$$

and the exchange term as

$$- \sum_{l,m,l',m'} G_{n,k;m',k'}^{m,l;n',l'} \mathbf{D}_{m',l';m,l} \quad (4.33)$$

$$= - \sum_{l,m,m'} \mathbf{D}_{m',l+k-k';m,l} M_{2(k-k')}^{n,m',m,n'}(k-l'). \quad (4.34)$$



The field  $M$  can be precomputed prior to the iteration and by putting the terms together we efficiently compute the Fock matrix as

$$\mathbf{F}_{n,k;n',k'} = \sum_{l,m,m'} \left[ M_{2(k'-l)}^{n,n',m,m'}(k-k') - M_{2(k-k')}^{n,m',m,n'}(k-l') \right] \mathbf{D}_{m',l+k-k';m,l} . \quad (4.35)$$

The storage requirements for  $M$  are only of the order  $\mathcal{O}(N_{\text{LL}}^4 N_{\phi}^2)$  and the constructing of the full Fock matrix  $\mathcal{O}(N_{\text{LL}}^4 N_{\phi}^3)$ , or  $\mathcal{O}(N_{\text{LL}}^4 L^6)$  in terms of the system size.

So far we derived the HF equations for spinless electrons. In order to incorporate spin one can now adapt either of the two most common procedures, the *restricted Hartree-Fock* (RHF) and the *unrestricted Hartree-Fock* (UHF) method [83]. In quantum chemistry, these different approaches are also called closed-shell and open-shell calculations, respectively. The electron states are constructed with a spatial and a spin part. Thereby the RHF method is the more straightforward approach by suggesting a double-occupation for each state with a spin up and a spin down electron. The spatial component is now independent of spin and will be equal in each doubly-occupied state. Clearly, for a spin-dependent Hamiltonian this is a severe simplification. The interaction of the electrons with the magnetic field, which leads to a spin-dependent Zeemann energy, will not be treated correctly. More realistically, one assumes the total independence of electrons with different spin, leading to the UHF procedure. The system will consist of two different species of electrons, with *up* spin ( $\sigma = 1/2$ ) and *down* spin ( $\sigma = -1/2$ ). Hence, the number of electrons is  $N_e = N_e^{\uparrow} + N_e^{\downarrow}$ . The spatial component of a state,  $\psi_{\alpha}^{\sigma}(\mathbf{r})$ , is assumed to also depend on the spin. The expansion in terms of Landau functions now reads

$$\psi_{\alpha}^{\sigma}(\mathbf{r}) = \sum_{n,a} \mathbf{C}_{n,a}^{\alpha,\sigma} \varphi_{n,a}(\mathbf{r}) , \quad (4.36)$$

with spin-dependent expansion coefficients. Using the spin-dependent states, a variation of the total energy just as for spineless electrons (Section 4.1) will yield the intuitive result [90] that different spin states interact only via the Coulomb interaction. Therefore the UHF equations, sometimes called *Pople-Nesbet* equations, are two self-consistent

eigenvalue problems, one for each spin, which are coupled through the Coulomb interaction. The exchange interaction is restricted to electrons of equal spin, which has the physically plausible explanation that a particular state of spin  $\sigma$  cannot exchange with an electron of spin  $-\sigma$  and will therefore not feel an energy reduction if such an unoccupied state should exist. In the following Chapters we will adapt the UHF procedure and introduce the respective spin-dependent equations.

Finally we want to mention one disadvantage of the UHF procedure which might lead to problems in quantitative considerations regarding the spin. The UHF method cannot guarantee the orthonormality between states of different spin. Such a restriction would in fact yield RHF states [91]. The states are no proper eigenfunctions of the total spin operator which leads to so-called *spin contamination* [92, 93]. The quality of the result can be checked after the calculation by computing the expectation value of the total spin operator. However, we do not expect relevant deviations in quantities such as charge density or compressibility, which we are going to investigate. Therefore, we neglect the time-consuming additional corrections and checks associated with this issue.

## 4.2 Solving the HF Equations with Spin

This chapter will be dedicated to the numerical solution of the HF problem. We will discuss the algorithms, issues of convergence and reliability, as well as their implementation. Clearly, the solver has to be efficient and give correct results under any setting of parameters. However, this turns out to be far from trivial. Turning back to the HF problem, we are now left with finding the correct spin-dependent expansion coefficients  $C_{n,k}^{\alpha,\sigma}$  [74, 75, 94, 95]. The spin-dependent Hamiltonian is represented in matrix form using the periodic Landau states  $|nk\rangle$  and we have

$$\begin{aligned} \mathbf{H}_{n,k;n',k'}^{\sigma} &= \langle \varphi_{n,k} | H_{2\text{DES}}^{\sigma} | \varphi_{n',k'} \rangle \\ &= \left( n + \frac{1}{2} + \frac{\sigma g^* m^*}{4 m_e} \right) \hbar \omega_c \delta_{n,n'} \delta_{k,k'} + \mathbf{V}_{n,k;n',k'} + \mathbf{F}_{n,k;n',k'}^{\sigma} \end{aligned} \quad (4.37)$$

with the cyclotron energy  $\hbar\omega_c = \hbar eB/m^*$ . The disorder matrix elements are given by  $\mathbf{V}_{n,k;n',k'} = \sum_{\mathbf{q}} V_I(\mathbf{q}) S_{n,k;n',k'}(\mathbf{q})$ , where mixing of Landau levels is included. The explicit form of the plane wave matrix elements  $S_{n,k;n',k'}(\mathbf{q}) = \langle \varphi_{nk} | \exp(i\mathbf{q} \cdot \mathbf{r}) | \varphi_{n'k'} \rangle$  is computed in Appendix E. The elements of the Fock matrix  $\mathbf{F}$  are

$$\mathbf{F}_{n,k;n',k'}^\sigma = \sum_{\sigma'} \sum_{l,m,l',m'} \left( G_{n,k;n',k'}^{m,l;m',l'} - \delta_{\sigma,\sigma'} G_{n,k;n',k'}^{m,l;m',l'} \right) \mathbf{D}_{m',l';m,l}^{\sigma'} \quad , \quad (4.38)$$

where the first term is the Hartree and the second the Fock contribution. The bi-electronic integrals  $G_{n,k;n',k'}^{m,l;m',l'} = \sum_{\mathbf{q} \neq 0} V_C(\mathbf{q}) S_{n,k;n',k'}(\mathbf{q}) S_{m,l;m',l'}(-\mathbf{q})$  can be further simplified as also given in Appendix E. A homogeneous, positive background is assumed that neutralises the charge of the electrons and thereby prevents the Coulomb term from diverging as  $|\mathbf{q}| \rightarrow 0$ . In fact, this interaction with the background can be shown to cancel with the term  $|\mathbf{q}| = 0$  in  $\mathbf{F}$  up to a contribution of the order of  $L^{-1}$  due to the finite system size [77]. The density matrix is given by

$$\mathbf{D}_{m,l;m',l'}^\sigma = \sum_{\alpha=1}^M f(\epsilon_\alpha^\sigma) \mathbf{C}_{m,l}^{\alpha\sigma} (\mathbf{C}_{m',l'}^{\alpha,\sigma})^* \quad , \quad (4.39)$$

with  $\text{Tr}(\mathbf{D}) = N_e$  and  $\mathbf{D}^\sigma \mathbf{D}^\sigma = \mathbf{D}^\sigma$ . Here  $f(\epsilon)$  denotes the Fermi function. A variational minimization of  $\langle \Psi | H_{2\text{DES}} | \Psi \rangle$  with respect to the coefficients as presented earlier yields the Hartree-Fock-Roothaan equation [78], a self-consistent, coupled eigenvalue problem which in compact form can be written as

$$\mathbf{H}^\sigma \mathbf{C}^\sigma = \mathbf{C}^\sigma \mathbf{E}^\sigma \quad , \quad (4.40)$$

with  $\mathbf{C}^\sigma = (\mathbf{C}_1^\sigma, \dots, \mathbf{C}_M^\sigma)$  being the matrix of eigenvectors and  $\mathbf{E}^\sigma = \text{diag}(\epsilon_1^\sigma, \dots, \epsilon_M^\sigma)$  the diagonal matrix of the eigenvalues  $\epsilon_1^\sigma \leq \epsilon_2^\sigma \leq \dots \leq \epsilon_M^\sigma$ . The equations are coupled through the Hamiltonian which depends on the electron densities of both spins. Following the aufbau principle [96], the density matrix is constructed starting from the energetically lowest lying state up to the Fermi level  $\epsilon_F$ . In our calculations, we keep  $N_e$  fixed and compute  $\epsilon_F$  as the energy of the highest occupied state afterwards. Since the Fock matrix depends on the density matrix, which in turn depends on the full solution

of the problem, (4.40) has to be calculated self-consistently which is numerically quite challenging. In the first step we use the solution of the non-interacting Hamiltonian  $\mathbf{h}^\sigma = \langle \varphi_{n,k} | h^\sigma | \varphi_{n',k'} \rangle$  as a starting guess for the coefficients  $\mathbf{C}^\sigma$ . From this solution,  $\mathbf{C}^{(0)}$ , we construct the density and Fock matrices and finally the full Hamiltonian. Diagonalisation yields an improved solution,  $\mathbf{C}^{(1)}$ . The process continues until convergence of the density matrix has been achieved. In practice, we compute the norm of the difference between successive density matrices  $\|\mathbf{D}^{(n+1)} - \mathbf{D}^{(n)}\| < \varepsilon$ . Here  $\|\cdot\|$  denotes the Hilbert-Schmidt norm defined as  $\|\mathbf{A}\| = \text{Tr}(\mathbf{A}\mathbf{A}^*)^{1/2}$ .

In each HF step, assembling the dense Fock matrix  $\mathbf{F}^\sigma$  scales as  $\mathcal{O}(N_{\text{LL}}^4 N_\phi^3)$  and is clearly very time-consuming. Any improvement, even though generally possible, is of little advantage since the diagonalisation is of similar complexity. Algorithms have been suggested to circumvent the costly diagonalisation [97, 98]. For the calculation of a particular disorder configuration and magnetic field, a self-consistent run has to be made for each of the  $M$  possible filling factors. Hence, the complexity of a complete HF calculation is of the order  $\mathcal{O}(2KN_{\text{LL}}^5 N_\phi^4)$  with  $K$  the number of iterations until convergence. The dependence on the system size is therefore  $\mathcal{O}(L^8)$ . For system sizes of  $L \sim 300\text{nm}$ , we find  $K \sim 100 - 1000$ . In all results presented here, convergence of the HF scheme is assumed for  $\varepsilon \leq 10^{-6}$ .

### 4.3 Calculation of the Total HF Energy

After having obtained the HF states, we need to calculate the total energy, which is the expectation value of the Hamiltonian of Equation (4.37) in the ground state,  $|\Phi\rangle$ . Splitting the Hamiltonian into a one-electron part,  $h$ , and a two-electron part,  $F$ , we calculate this expectation value individually. We can write for the one-electron Hamiltonian

$$h = \sum_{\sigma} \sum_{\alpha, \beta} \langle \psi_{\sigma}^{\sigma} | h^{\sigma} | \psi_{\beta}^{\sigma} \rangle \hat{a}_{\alpha, \sigma}^{\dagger} \hat{a}_{\beta, \sigma} . \quad (4.41)$$

With the expectation value of the one-electron operator,  $\langle \phi | \hat{a}_{\alpha,\sigma}^\dagger \hat{a}_{\beta,\sigma} | \phi \rangle = f_\alpha \delta_{\alpha,\beta}$ , as well as the expansion of the wave functions, the one-electron energy reads

$$E^{1e} = \langle \phi | h | \phi \rangle = \sum_{\sigma} \sum_{\alpha,\beta} \sum_{k,n,k',n'} (\mathbf{C}_{n,k}^{\alpha,\sigma})^* \mathbf{C}_{n',k'}^{\beta,\sigma} \langle \varphi_{n,k} | h^\sigma | \varphi_{n',k'} \rangle \langle \phi | \hat{a}_{\sigma,\alpha}^\dagger \hat{a}_{\sigma,\beta} | \phi \rangle \quad (4.42)$$

$$= \sum_{\sigma} \sum_{\alpha,\beta} \sum_{k,n,k',n'} (\mathbf{C}_{n,k}^{\alpha,\sigma})^* \mathbf{C}_{n',k'}^{\beta,\sigma} \langle \varphi_{n,k} | h^\sigma | \varphi_{n',k'} \rangle f_\alpha \delta_{\alpha,\beta} \quad (4.43)$$

$$= \sum_{\sigma} \sum_{n,k,n',k'} \langle \varphi_{n,k} | h^\sigma | \varphi_{n',k'} \rangle \mathbf{D}_{n',k';n,k}^\sigma. \quad (4.44)$$

The two electron part of the Hamiltonian can be written as

$$F = \frac{1}{2} \sum_{\sigma,\sigma'} \sum_{\alpha,\beta,\vartheta,\delta} \langle \psi_\alpha^\sigma \psi_\vartheta^{\sigma'} | F^{\sigma,\sigma'} | \psi_\delta^{\sigma'} \psi_\beta^\sigma \rangle \hat{a}_{\alpha,\sigma}^\dagger \hat{a}_{\vartheta,\sigma'}^\dagger \hat{a}_{\delta,\sigma'} \hat{a}_{\beta,\sigma}. \quad (4.45)$$

With the usual expansion as well as the expectation value of the two electrons operator,

$$\langle \phi | \hat{a}_{\sigma,\alpha}^\dagger \hat{a}_{\sigma',\vartheta}^\dagger \hat{a}_{\sigma',\delta} \hat{a}_{\sigma,\beta} | \phi \rangle = f_\alpha f_\vartheta (\delta_{\alpha,\beta} \delta_{\vartheta,\delta} - \delta_{\sigma,\sigma'} \delta_{\alpha,\delta} \delta_{\beta,\vartheta}), \quad (4.46)$$

the two electron energy yields

$$E^{2e} = \langle \phi | F | \phi \rangle \quad (4.47)$$

$$= \frac{1}{2} \sum_{\sigma} \sum_{k,n,k',n'} \mathbf{D}_{n',k';n,k}^\sigma \sum_{\sigma'} \sum_{l,m,l',m'} \left( G_{n,k;n',k'}^{m,l;m',l'} - \delta_{\sigma,\sigma'} G_{n,k;m',l'}^{m,l;n',k'} \right) \mathbf{D}_{m',l';m,l}^{\sigma'} \quad (4.48)$$

where  $G$  is the bielectronic integral. Putting both together, we obtain the result for the total HF energy as

$$E_{\text{HF}}^{\text{tot}} = \frac{1}{2} \sum_{\sigma} \sum_{n,k;n',k'} (2\mathbf{h}_{n,k;n',k'}^\sigma + \mathbf{F}_{n,k;n',k'}^\sigma) \mathbf{D}_{n',k';n,k}^\sigma, \quad (4.49)$$

where  $\mathbf{h}$  is the sum of all one-particle terms in the Hamiltonian in Landau basis, and  $\mathbf{F}$  the two particle term, respectively.

## 4.4 The Roothaan Algorithm

The Roothaan algorithm is the simplest fixed point iteration scheme for the solution of the self-consistent HF eigenvalue problem. Unlike iterative subspace methods [99],

for the following algorithms we only need to keep track of two consecutive matrices during the iteration procedure. Therefore we will apply the subindices *old* and *new* to the matrices. First, we will briefly recall the set of equations in question.

$$\mathbf{H}^\sigma(\mathbf{D})\Phi^\sigma = \Phi^\sigma \mathbf{E}^\sigma, \quad (4.50)$$

$$(\Phi^\sigma)^\dagger \Phi^\sigma = \mathbf{I}_M, \quad (4.51)$$

$$\mathbf{D}^\sigma = \Phi^\sigma \Omega^\sigma (\Phi^\sigma)^\dagger, \quad (4.52)$$

with  $\Phi^\sigma = (\mathbf{C}_1^\sigma, \dots, \mathbf{C}_M^\sigma)$  being the matrix of eigenvectors with the corresponding matrix  $\mathbf{E}^\sigma = \text{diag}(\epsilon_1^\sigma, \dots, \epsilon_M^\sigma)$  of eigenvalues in *ascending order*, belonging to the linear eigenvalue equation

$$\mathbf{H}^\sigma(\mathbf{D})\mathbf{C}_\alpha^\sigma = \epsilon_\alpha^\sigma \mathbf{C}_\alpha^\sigma, \quad (4.53)$$

and the occupation matrix  $\{\Omega^\sigma\}_{\alpha,\beta} = \delta_{\alpha,\beta} f(\epsilon_\alpha^\sigma)$ , where  $f(\epsilon)$  is the Fermi function. The density matrix is thus constructed from the  $N_e$  energetically lowest eigenvector. This scheme is known as the *aufbau* principle. For notational convenience we use the notation  $\mathbf{D} = (\mathbf{D}^\uparrow, \mathbf{D}^\downarrow)$  and  $\mathbf{F} = (\mathbf{F}^\uparrow, \mathbf{F}^\downarrow)$ .

Convergence is established if the difference between two consecutive density matrices is smaller than a specified threshold, i.e.

$$\|\mathbf{D}_{\text{new}}^\sigma - \mathbf{D}_{\text{old}}^\sigma\| < \epsilon_{\text{conv}}. \quad (4.54)$$

We sketch the Roothaan algorithm now in Algorithm 1 ( $\forall \sigma \in \{\uparrow, \downarrow\}$  is understood in each line). Thus, we use the non-interacting density matrix as our initial guess.

As a matter of fact convergence of the Roothaan algorithm [78] is rather poor. In most cases it runs into an oscillating limit cycle. We will briefly sketch the proof now with a plausibility argument using Figure 4.4. It can be shown [83] that the Roothaan algorithm converges to a critical point  $(\mathbf{D}_{\text{new}}^\sigma, \mathbf{D}_{\text{old}}^\sigma) \rightarrow (\mathbf{D}_\infty, \mathbf{D}'_\infty)$ , where the density matrices are mutual solutions of each others HF eigenproblem. Now if this point lies on the diagonal, i.e.  $\mathbf{D}_\infty = \mathbf{D}'_\infty$ , the iteration will converge in the sense that  $\|\mathbf{D}_{\text{new}}^\sigma - \mathbf{D}_{\text{old}}^\sigma\| \rightarrow 0$ . More often, however, this point will not lie on the diagonal and the difference between the

---

**Algorithm 1** Roothaan Algorithm (Initialisation and iteration)

---

```
1: AssembleSingleParticleMatrix( $\sigma$ )  $\rightarrow \mathbf{h}^\sigma$ 
2: Solve  $\mathbf{h}^\sigma \Phi^\sigma = \Phi^\sigma \mathbf{E}^\sigma$ 
3: AssembleOccupationMatrix( $\mathbf{E}^\sigma$ )  $\rightarrow \Omega^\sigma$ 
4:  $\Phi^\sigma \Omega^\sigma (\Phi^\sigma)^\dagger \rightarrow \mathbf{D}_{\text{old}}^\sigma$ 
5: AssembleFockMatrix( $\mathbf{D}_{\text{old}}$ )  $\rightarrow \mathbf{F}_{\text{old}}^\sigma$ 
6:  $\mathbf{h} + \mathbf{F}_{\text{old}} \rightarrow \mathbf{H}_{\text{old}}$ 
7:  $0 \rightarrow k$ 
8: loop
9:   Solve  $\mathbf{H}_{\text{old}}^\sigma \Phi^\sigma = \Phi^\sigma \mathbf{E}^\sigma$ 
10:  AssembleOccupationMatrix( $\mathbf{E}^\sigma$ )  $\rightarrow \Omega^\sigma$ 
11:   $\Phi^\sigma \Omega^\sigma (\Phi^\sigma)^\dagger \rightarrow \mathbf{D}_{\text{new}}^\sigma$ 
12:  AssembleFockMatrix( $\mathbf{D}_{\text{new}}$ )  $\rightarrow \mathbf{F}_{\text{new}}^\sigma$ 
13:   $\mathbf{h} + \mathbf{F}_{\text{new}} \rightarrow \mathbf{H}_{\text{new}}$ 
14:  if  $\max(\|\mathbf{D}_{\text{new}}^\uparrow - \mathbf{D}_{\text{old}}^\uparrow\|, \|\mathbf{D}_{\text{new}}^\downarrow - \mathbf{D}_{\text{old}}^\downarrow\|) < \epsilon_{\text{conv}}$  OR  $k > N_{\text{max}}$  then
15:    EXIT
16:  end if
17:   $\mathbf{D}_{\text{new}} \rightarrow \mathbf{D}_{\text{old}}$ 
18:   $\mathbf{H}_{\text{new}} \rightarrow \mathbf{H}_{\text{old}}$ 
19:   $k + 1 \rightarrow k$ 
20: end loop
```

---

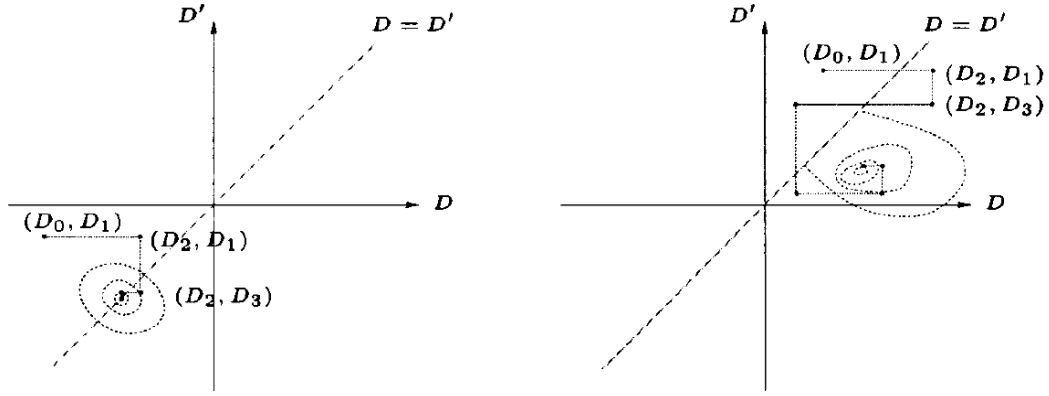


Figure 4.1: Oscillatory behaviour of the Roothaan algorithm [96]. Left: Critical point lies on the diagonal and the iteration converges without oscillations. Right: Critical point lies on the off-diagonal which leads to oscillations of the algorithm. The two density matrices are mutually solutions to the respective HF-problem.

consecutive density matrices converges to a finite constant. This behaviour is mainly observed with filling factors close to an integer value and is due to the mixing of occupied and unoccupied states. More specifically, neglecting the divergent  $\mathbf{q} = 0$  term in the Coulomb potential can lead to a situation where an unoccupied states has lower energy than the occupied state. Therefore, in course of the iteration and by virtue of the aufbau principle, an electron would try to occupy the energetically lower state. However, the old, now unoccupied site, has in turn a lower energy and will be favoured by the electron. Clearly this situation will not lead to convergence. We have illustrated that behaviour in the top row of Figure 4.2 by showing the HF-potential along the  $x$ -axis,  $U_{\text{HF}}(x)$ , resulting from the two electrons, for two subsequent steps of the iteration. The system has a size of  $L = 400\text{nm}$  and is periodic in  $x$ -direction. The broken lines are periodic reproductions of the full line (calculated potential). Initially, the two electrons are sitting close to each other around  $x = L/2$  and the system has a corresponding density matrix  $\mathbf{D}_{\text{old}}$ . The left column shows  $U_{\text{HF}}(x)$  according to this initial density matrix  $\mathbf{D}_{\text{old}}$ , and the right column according to the subsequent density matrix  $\mathbf{D}_{\text{new}}$  of the Roothaan



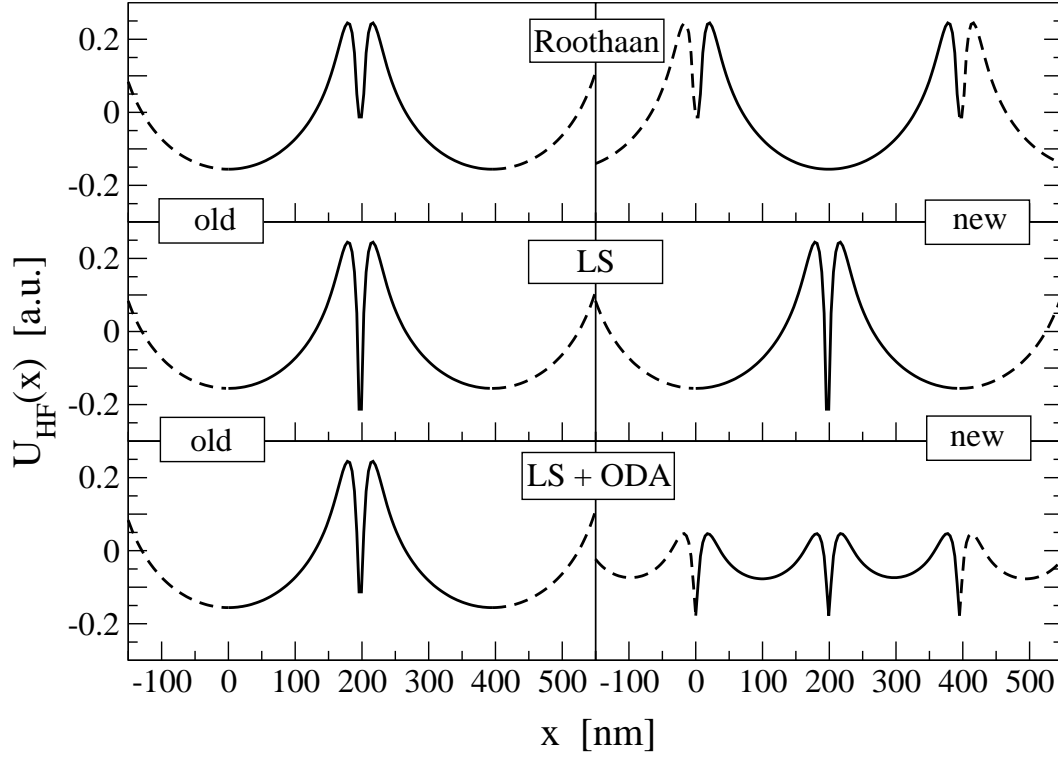


Figure 4.2: Cross-section of the HF-potential due to two close-by electrons before and after the first iteration of the Roothaan, the LS, and LS + ODA (different rows). The left column shows the initial state, the right shows the state after one step of iteration of the respective algorithm.

iteration. After this first iteration, the electrons have adapted their states according to the aufbau principle and populated the lowest two states around  $x = 0$ . By virtue of the PBC, the distribution has mapped back into itself. A following iteration will then restore the initial  $\mathbf{D}_{\text{old}}$  state. Thus, the electrons will not become separated. They move in synch during the iterator process and we cannot achieve convergence for this system. We will discuss a remedy in the following section.

## 4.5 The Level Shifting Algorithm

A natural attempt to avoid the oscillations in the Roothaan algorithm is to introduce an energy penalty for the aforementioned off-diagonal fixpoints by minimising a penalised energy functional

$$E'(\mathbf{D}_{\text{old}}, \mathbf{D}_{\text{new}}) = E(\mathbf{D}_{\text{old}}, \mathbf{D}_{\text{new}}) + b \|\mathbf{D}_{\text{old}} - \mathbf{D}_{\text{new}}\|^2, \quad (4.55)$$

instead of the actual HF energy functional. The corresponding HF eigenproblem now changes in a way that not  $\mathbf{F}$  is diagonalised but rather  $\mathbf{F}' = \mathbf{F} - b\mathbf{D}$ . By doing so, the eigenvalues shift by  $\epsilon_i^\sigma \rightarrow \epsilon_i^\sigma - b \quad \forall \quad \epsilon_i^\sigma \leq \epsilon_F$ , but the eigenstates remain unaffected. This can be seen as follows. Writing the eigenvalue equation as

$$\mathbf{C}_\beta^* \mathbf{H}' \mathbf{C}_\beta = \sum_{c,d} \mathbf{h}_{cd} \mathbf{C}_{c\beta}^* \mathbf{C}_{d\beta} + \sum_{c,d} \mathbf{F}'_{cd} \mathbf{C}_{c\beta}^* \mathbf{C}_{d\beta} = \epsilon'_\beta \quad (4.56)$$

and

$$\epsilon'_\beta = \epsilon_\beta - b \sum_{c,d} \mathbf{D}_{cd} \mathbf{C}_{c\beta}^* \mathbf{C}_{d\beta} \quad (4.57)$$

$$= \epsilon_\beta - b \sum_{\alpha} f_{\alpha} \sum_{c,d} \mathbf{C}_{c\alpha} \mathbf{C}_{d\alpha}^* \mathbf{C}_{c\beta}^* \mathbf{C}_{d\beta} \quad (4.58)$$

$$= \epsilon_\beta - b f_{\beta}. \quad (4.59)$$

Hence, by subtracting the density matrix with a prefactor  $b$ , all the occupied eigenvalues (below  $\epsilon_F$ ) shift by  $b$ . This algorithm favours already occupied states and for a big enough parameter  $b$ , oscillations are successfully suppressed. Interestingly, quite a different approach has also led to this algorithm [100] which is called the Level-Shifting-Algorithm (LS) and  $b$  the level-shift parameter. As we have seen in the previous section, the shortcoming of the Roothaan algorithm is a mixing of occupied and unoccupied states. The initial idea behind the LS algorithm was simply to separate the so called real and virtual orbitals energetically to avoid this behaviour. Subtracting a small multiple of the density matrix off the Fock matrix accomplishes this trick. It can be shown that the LS algorithm converges for  $b \geq b_0$ . However, there exists no rigorous value for

$b_0$ . Moreover, even if  $b$  is chosen generously large, it turns out that in some cases this trick still does not yield a physical solution. In the middle row of Figure 4.2 we have illustrated this effect of the level shifting. Again, the left figure shows the initial configuration corresponding to  $\mathbf{D}_{\text{old}}$ . If  $b$  is chosen too small, we recover the situation of the Roothaan algorithm. In the middle row we have chosen a large  $b$ . In the right column we depicted the potential after one iteration of the LS algorithm, i.e. according to  $\mathbf{D}_{\text{new}}$ . Due to the level shifting, the electrons are already in the lowest state and the aufbau principle does not change the occupation. The level shifting has *pinned* the states. Thus, we have found a converged solution which is, however, unphysical. The two electrons are still too close to each other.

## 4.6 The Optimal Damping Algorithm

The two algorithms detailed above proved rather inadequate. The Roothaan algorithm tends to run into oscillations and the LS algorithm yields unphysical solutions. Another promising class of algorithms are the *relaxed constraints* algorithms. The naming is due to the non-linear constraint  $\mathbf{D}\mathbf{D} = \mathbf{D}$  being relaxed during the iteration to the inequality  $\mathbf{D}\mathbf{D} \leq \mathbf{D}$ . Upon convergence the equality is recovered [96]. According to the authors, this algorithm is not based on any physical arguments but rather comes from empirical studies to force convergence. The algorithm we want to discuss in this section is called the *Optimal Damping Algorithm* (ODA). The iteration is carried out just as in the Roothaan algorithm, only that the new density matrix is a mixture of the old and the new density matrix, i.e.

$$\mathbf{D} = (1 - \lambda)\mathbf{D}_{\text{old}} + \lambda\mathbf{D}_{\text{new}} , \quad (4.60)$$

with a damping parameter  $\lambda$  which is chosen optimally according to the direction of steepest descent in the total HF energy. Now we will demonstrate how to derive the optimal  $\lambda$  in a generalisation of the RHF ODA approach [96], applicable for the UHF procedure. Recall that in the UHF approach, electrons of different spin are treated

separately, yielding separate density matrices which we label with  $\sigma$ . Thus, we will have spin dependent damping parameters and the new density matrices are constructed as the convex linear combination

$$\mathbf{D}^\sigma = \mathbf{D}_{\text{old}}^\sigma + \lambda^\sigma (\mathbf{D}_{\text{new}}^\sigma - \mathbf{D}_{\text{old}}^\sigma) . \quad (4.61)$$

For reasons of notational convenience we adapt the abbreviation  $\mathbf{D} = \{\mathbf{D}^\uparrow, \mathbf{D}^\downarrow\}$ . With those notational conventions we write the total energy functional as

$$E_{\text{tot}}[\mathbf{D}] = \sum_{\sigma} \text{Tr} \left[ \mathbf{h}^\sigma \mathbf{D}^\sigma + \frac{1}{2} \mathbf{F}^\sigma(\mathbf{D}) \mathbf{D}^\sigma \right] , \quad (4.62)$$

where the trace is excluding the spin. Moreover we define a partial Fock matrix,  $\mathbf{P}$ , by  $\mathbf{F}^\sigma(\mathbf{D}) = \sum_{\sigma'} \mathbf{P}^{\sigma, \sigma'}(\mathbf{D}^{\sigma'})$ , where we can later make use of the symmetry property

$$\text{Tr}[\mathbf{P}^{\sigma, \sigma'}(\mathbf{D}^{\sigma'}) \mathbf{D}^\sigma] = \text{Tr}[\mathbf{P}^{\sigma, \sigma'}(\mathbf{D}^\sigma) \mathbf{D}^{\sigma'}] . \quad (4.63)$$

The new energy with the density matrix of Equation (4.61) reads

$$E_{\text{tot}}[\mathbf{D}] = \sum_{\sigma} \{ \text{Tr}[\mathbf{h}^\sigma \mathbf{D}_{\text{old}}^\sigma] + \lambda^\sigma \text{Tr}[\mathbf{h}^\sigma (\mathbf{D}_{\text{new}}^\sigma - \mathbf{D}_{\text{old}}^\sigma)] \} + \quad (4.64)$$

$$\frac{1}{2} \sum_{\sigma, \sigma'} \text{Tr} \{ \mathbf{P}^{\sigma, \sigma'}(\mathbf{D}_{\text{old}}^{\sigma'} + \lambda^{\sigma'} [\mathbf{D}_{\text{new}}^{\sigma'} - \mathbf{D}_{\text{old}}^{\sigma'}]) [\mathbf{D}_{\text{old}}^\sigma + \lambda^\sigma (\mathbf{D}_{\text{new}}^\sigma - \mathbf{D}_{\text{old}}^\sigma)] \} . \quad (4.65)$$

With the total Hamiltonian matrix  $\mathbf{H} = \mathbf{h} + \mathbf{F}$ , this can be rewritten as

$$E_{\text{tot}}[\mathbf{D}] = E_{\text{tot}}[\mathbf{D}_{\text{old}}] + \sum_{\sigma} \lambda^\sigma \text{Tr}[\mathbf{H}^\sigma (\mathbf{D}_{\text{new}}^\sigma - \mathbf{D}_{\text{old}}^\sigma)] + \quad (4.66)$$

$$\frac{1}{2} \sum_{\sigma, \sigma'} \lambda^\sigma \lambda^{\sigma'} \text{Tr}[\mathbf{P}^{\sigma, \sigma'}(\mathbf{D}_{\text{new}}^{\sigma'} - \mathbf{D}_{\text{old}}^{\sigma'}) (\mathbf{D}_{\text{new}}^\sigma - \mathbf{D}_{\text{old}}^\sigma)] . \quad (4.67)$$

This quadratic form is our main result of the ODA for UHF and can be conveniently written as

$$E_{\text{tot}}[\mathbf{D}] = E_{\text{tot}}[\mathbf{D}_{\text{old}}] + \vec{\lambda} \cdot \vec{s} + \frac{1}{2} \vec{\lambda}^T \cdot \mathbf{c} \cdot \vec{\lambda} , \quad (4.68)$$

where we have defined

$$\vec{\lambda} = \begin{pmatrix} \lambda^\uparrow \\ \lambda^\downarrow \end{pmatrix} \quad (4.69)$$

and

$$\vec{s} = \begin{pmatrix} \text{Tr}[\mathbf{H}^\uparrow (\mathbf{D}_{\text{new}}^\uparrow - \mathbf{D}_{\text{old}}^\uparrow)] \\ \text{Tr}[\mathbf{H}^\downarrow (\mathbf{D}_{\text{new}}^\downarrow - \mathbf{D}_{\text{old}}^\downarrow)] \end{pmatrix} \quad (4.70)$$

and the  $2 \times 2$  matrix  $\mathbf{c}$  with the matrix elements

$$\mathbf{c}^{\sigma, \sigma'} = \text{Tr}[\mathbf{P}^{\sigma, \sigma'} (\mathbf{D}_{\text{new}}^{\sigma'} - \mathbf{D}_{\text{old}}^{\sigma'}) (\mathbf{D}_{\text{new}}^\sigma - \mathbf{D}_{\text{old}}^\sigma)] . \quad (4.71)$$

The problem which has to be solved is finding the optimal  $\vec{\lambda}_{\text{ODA}}$  that yields the lowest energy for the next iteration step, i.e.

$$\vec{\lambda}_{\text{ODA}} = \arg \inf \left\{ E_{\text{tot}}(\mathbf{D}), \vec{\lambda} \in [0, 1] \otimes [0, 1] \right\} . \quad (4.72)$$

Equation (4.68) therefore has a non-trivial minimum only if the quadratic form is positive semi-definite. Otherwise, if the extremum is a saddle point the solution has to lie at the border of the constraint region  $[0, 1] \otimes [0, 1]$ , and is readily found.

In the following we schematically sketch the full ODA procedure, where  $\forall \sigma, \sigma' \in \{\uparrow, \downarrow\}$  is understood in each line where the indices appear. The ODA ensures by construction that a decrease of the total HF energy is realised in each step, since we are searching in the direction of steepest descent. However, there are some issues with ODA, too. Under certain conditions the decrease in energy can switch from being linear in the smallest level spacing to being quadratic [83]. Clearly, with a quadratic dependence, the decrease becomes rather unnoticeable for small level spacings. Moreover, we found cases of oscillatory behaviour of the ODA. The ODA will oscillate with a cycle of four iterations. The problem can be understood by treating the physics with a bit more care. In Section 3.3 we established that the divergent  $\mathbf{q} = 0$  term in the Hamiltonian cancels with the neutralising background charge, which is indeed true for Hartree-interacting electrons. Now one might be tempted to assume a similar situation for the HF Hamiltonian (4.37).

---

**Algorithm 2** ODA (Initialisation and iteration)

---

```

1: AssembleSingleParticleMatrix( $\sigma$ )  $\rightarrow \mathbf{h}^\sigma$ 
2: Solve  $\mathbf{h}^\sigma \Phi^\sigma = \Phi^\sigma \mathbf{E}^\sigma$ 
3: AssembleOccupationMatrix( $\mathbf{E}^\sigma$ )  $\rightarrow \Omega^\sigma$ 
4:  $\Phi^\sigma \Omega^\sigma (\Phi^\sigma)^\dagger \rightarrow \mathbf{D}_{\text{old}}^\sigma$ 
5: AssembleFockMatrix( $\mathbf{D}_{\text{old}}^\sigma$ )  $\rightarrow \mathbf{F}_{\text{old}}^\sigma$ 
6: AssemblePartialFockMatrix( $\mathbf{D}_{\text{old}}^{\sigma'}, \sigma$ )  $\rightarrow \mathbf{P}_{\text{old}}^{\sigma, \sigma'}$ 
7:  $\mathbf{h}^\sigma + \mathbf{F}_{\text{old}}^\sigma \rightarrow \mathbf{H}_{\text{old}}^\sigma$ 
8:  $0 \rightarrow k$ 
9: loop
10:   Solve  $\mathbf{H}_{\text{old}}^\sigma \Phi^\sigma = \Phi^\sigma \mathbf{E}^\sigma$ 
11:   AssembleOccupationMatrix( $\mathbf{E}^\sigma$ )  $\rightarrow \Omega^\sigma$ 
12:    $\Phi^\sigma \Omega^\sigma (\Phi^\sigma)^\dagger \rightarrow \mathbf{D}_{\text{new}}^\sigma$ 
13:   AssembleFockMatrix( $\mathbf{D}_{\text{new}}^\sigma$ )  $\rightarrow \mathbf{F}_{\text{new}}^\sigma$ 
14:   AssemblePartialFockMatrix( $\mathbf{D}_{\text{new}}^{\sigma'}, \sigma$ )  $\rightarrow \mathbf{P}_{\text{new}}^{\sigma, \sigma'}$ 
15:    $\mathbf{h}^\sigma + \mathbf{F}_{\text{new}}^\sigma \rightarrow \mathbf{H}_{\text{new}}^\sigma$ 
16:   if  $\max(\|\mathbf{D}_{\text{new}}^\uparrow - \mathbf{D}_{\text{old}}^\uparrow\|, \|\mathbf{D}_{\text{new}}^\downarrow - \mathbf{D}_{\text{old}}^\downarrow\|) < \epsilon_{\text{conv}}$  OR  $k > N_{\text{max}}$  then
17:     EXIT
18:   end if
19:    $\text{Tr}[\mathbf{H}_{\text{old}}^\sigma (\mathbf{D}_{\text{new}}^\sigma - \mathbf{D}_{\text{old}}^\sigma)] \rightarrow \mathbf{s}^\sigma$ 
20:    $\text{Tr}[(\mathbf{P}_{\text{new}}^{\sigma, \sigma'} - \mathbf{P}_{\text{old}}^{\sigma, \sigma'}) (\mathbf{D}_{\text{new}}^\sigma - \mathbf{D}_{\text{old}}^\sigma)] \rightarrow \mathbf{c}^{\sigma, \sigma'}$ 
21:   OptimizeQuadraticForm( $\mathbf{c}, \mathbf{s}$ )  $\rightarrow \lambda$ 
22:    $(1 - \lambda^\sigma) \mathbf{D}_{\text{new}}^\sigma + \lambda^\sigma \mathbf{D}_{\text{old}}^\sigma \rightarrow \mathbf{D}_{\text{old}}^\sigma$ 
23:   AssembleFockMatrix( $\mathbf{D}_{\text{old}}^\sigma$ )  $\rightarrow \mathbf{F}_{\text{old}}^\sigma$ 
24:   AssemblePartialFockMatrix( $\mathbf{D}_{\text{old}}^{\sigma'}, \sigma$ )  $\rightarrow \mathbf{P}_{\text{old}}^{\sigma, \sigma'}$ 
25:    $\mathbf{h}^\sigma + \mathbf{F}_{\text{old}}^\sigma \rightarrow \mathbf{H}_{\text{old}}^\sigma$ 
26:    $k + 1 \rightarrow k$ 
27: end loop

```

---

However, as we can easily verify, that is not the case for a system of finite size. Since we assume overall charge neutrality, an electron interacts with  $N_e$  positive charges of the homogeneous background, but only with  $N_e - 1$  electrons. Let us turn to the HF case now. The matrix elements of the electron-electron part of the HF Hamiltonian without the  $\mathbf{q} = 0$  part are

$$\langle \varphi_c | \mathcal{H}_{e-e} | \varphi_d \rangle = \mathbf{F}_{cd} = \sum_{\alpha} f_{\alpha} \sum_{\mathbf{q} \neq 0} v(\mathbf{q}) \left[ \langle \alpha | e^{i\mathbf{q}\mathbf{r}} | \alpha \rangle \langle \varphi_c | e^{-i\mathbf{q}\mathbf{r}'} | \varphi_d \rangle - \langle \alpha | e^{i\mathbf{q}\mathbf{r}} | \varphi_d \rangle \langle \varphi_c | e^{-i\mathbf{q}\mathbf{r}'} | \alpha \rangle \right]. \quad (4.73)$$

We rewrite the eigenvalue equation as

$$\mathbf{C}_{\beta}^* \mathbf{H} \mathbf{C}_{\beta} = \sum_{c,d} \mathbf{h}_{cd} \mathbf{C}_{c\beta}^* \mathbf{C}_{d\beta} + \sum_{c,d} \mathbf{F}_{cd} \mathbf{C}_{c\beta}^* \mathbf{C}_{d\beta} = \epsilon_{\beta}, \quad (4.74)$$

and find that by including the  $\mathbf{q} = 0$  term,  $\epsilon_{\beta}$  changes to  $\tilde{\epsilon}_{\beta}$  as follows

$$\tilde{\epsilon}_{\beta} = \epsilon_{\beta} + v(0) \sum_{\alpha} f_{\alpha} [\langle \alpha | \alpha \rangle \langle \beta | \beta \rangle - \langle \alpha | \beta \rangle \langle \beta | \alpha \rangle] \quad (4.75)$$

$$= \epsilon_{\beta} + v(0) \sum_{\alpha} f_{\alpha} (1 - \delta_{\alpha,\beta}) \quad (4.76)$$

$$= \epsilon_{\beta} + v(0)(N_e - f_{\beta}). \quad (4.77)$$

As again easily verified, the contribution of the background interaction is precisely

$$\sum_{c,d} \langle \varphi_c | \mathcal{H}_{el-bg} + \mathcal{H}_{bg-bg} | \varphi_d \rangle \mathbf{C}_{c\beta}^* \mathbf{C}_{d\beta} = -v(0)N_e \quad (4.78)$$

and thus we find for the correct eigenvalues,

$$\tilde{\epsilon}_{\beta} = \epsilon_{\beta} - v(0)f_{\beta}. \quad (4.79)$$

The interpretation of this result is, that interaction takes place only with electrons below  $\epsilon_F$ . Thereby an occupied state,  $\epsilon_{\beta} \leq \epsilon_F$ , interacts with all other electrons apart from itself, whereas an unoccupied state, i.e.  $\epsilon_{\beta} > \epsilon_F$ , interacts with *all* electrons and therefore has a correspondingly higher energy. The energy shift for a square system of size  $L \times L$

can be found by integrating over the area,

$$v(0) = \frac{e^2}{4\pi\epsilon\epsilon_0} \int_{L \times L} \frac{d^2\mathbf{r}}{L^2} \frac{1}{|\mathbf{r}|} \approx \frac{1.76}{L} \frac{e^2}{4\pi\epsilon\epsilon_0}. \quad (4.80)$$

For an infinite system, this correction goes to zero. In our finite size case, however, we need to take care of this expression. We can identify Equation (4.79) with Equation 4.59, the LS algorithm. Thus,  $v(0)$  takes on the role of the level-shifting parameter. As it turns out in our numerical calculations, this is precisely the correct value of the shift-parameter to prevent occupied and unoccupied states from mixing together or likewise prevents electrons from getting pinned down. Thus by combining the ODA with the LS algorithm, we have found a stable scheme which converges in any case. In the bottom row of Figure 4.2 we depict two subsequent iteration steps of a combined ODA + LS algorithm. The two charge densities of the close-by electrons separates with the correct distance of  $L/2$ . In conclusion, combining the ODA and the LS algorithm with a level shift parameter of  $v(0)$  seems to guarantee convergence under any circumstances. It might be an interesting mathematical issue whether there exists a more rigorous derivation of this empirical observation.

## 4.7 Convergence

In general it is very difficult to prove convergence properties for those algorithms [83]. Therefore numerical checks are useful for establishing a performance evaluation. As it turns out the performance also depends strongly on the interaction strength and the position of the Fermi level. For some filling factors and choices of parameters, we might find fast convergence with one of the algorithms described above. However, over the whole range of filling factors only a combination of ODA and LSA can give good convergence. In Figure 4.3 we have depicted the convergence behaviour for a typical HF run at four different filling factors. Note, that we have plotted the convergence precision as defined by Equation (4.54), rather than the total HF energy, which is also sometimes used as a measure. In comparison to the energy which acquires a finite value



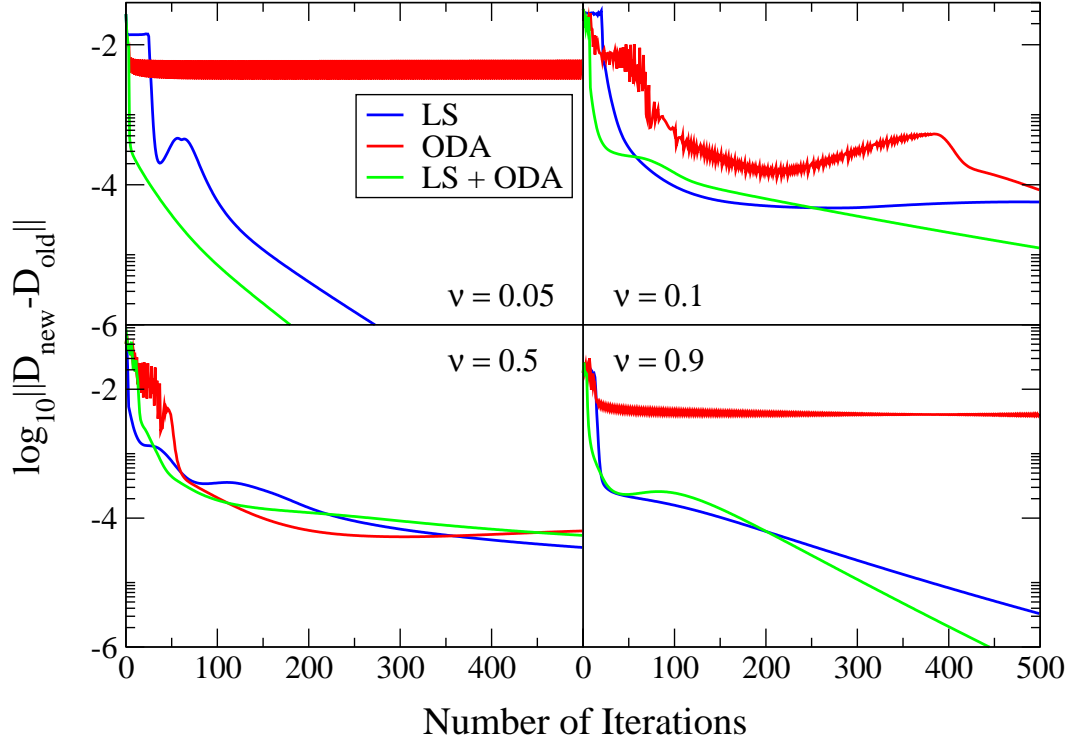


Figure 4.3: Convergence behaviour of the three algorithms during the first 500 iterations. Almost similar behaviour is found for other configurations (system size, magnetic field, disorder strength). The combined ODA + LS algorithm shows overall the best convergence properties.

at convergence, the precision should always converge to zero.

## 4.8 Further Improvements

A possible further improvement of convergence can be achieved when considering not only the previous density matrix but also density matrices before that. This scheme is called direct inversion in the iterative subspace (DIIS) algorithm [96, 99]. The idea is to construct the new density matrix  $\mathbf{D}_{\text{new}} = \mathbf{D}_{k+1}$  as a convex linear combination of several previous density matrices,  $\mathbf{D}_i$ , i.e.

$$\mathbf{D}_{\text{new}} = \sum_{i=0}^{k+1} c_i \mathbf{D}_i, \quad (4.81)$$

with the constraint  $0 \leq c_i \leq 1$  and  $\sum_i c_i = 1$ . Similarly to the ODA, an optimal set of  $c_i$ 's can be found. Moreover there exist quadratically convergent algorithms [96] that might accelerate convergence towards the end of the iteration. However, the extra effort and the increased memory requirements might not outweigh the performance gain in our case. Other so-called linear scaling approaches have been proposed [97, 98] that replace the time consuming construction and diagonalisation of the Fock matrix, such as conjugate gradient search or polynomial expansion. They seem to work best for large molecules and no effort has been made in this work to verify performance gain for our system. This could be a starting point for further research.

## Chapter 5

# Properties of the 2DEG

### 5.1 Density of States and Mobility

The term density of states is usually used in two different contexts. One has to specify whether the single-particle property, the tunneling density of states (DOS) or the thermodynamic density of states (TDDOS) is meant. The former is related to the tunneling probability of a single electron into the 2DEG, without allowing for redistribution of the charge density. The latter, on the other hand, is a property obtained after the collective relaxation and is related to the electronic compressibility, which is discussed in the next section [28, 29]. In this section we focus on the tunneling DOS defined as

$$\rho(E) = \sum_{\alpha} \delta(E - E_{\alpha}) . \quad (5.1)$$

Evidently, knowledge of the distribution of energy levels is required. This is intimately related to the electron-impurity interaction and thus the electron lifetime. We start by tuning our parameters for the electron-impurity interaction to realistic values by estimating the zero field mobility, defined as  $\mu_0 = e\tau/m^*$ , with  $\tau$  being the transport scattering time [28, 29]. The mobility is experimentally determined by constant source-drain-voltage conductance measurements using the relation  $\sigma_{SD} = n_e e \mu_0$  [29] or theoretically calculated via the Boltzmann transport equation [28, 29]. Generally speak-

ing it is desirable to have samples with low effective mass and high mobility, since the observability of quantisation requires

$$\hbar\omega_c = \frac{\hbar eB}{m^*} > k_B T \quad (5.2)$$

which be satisfied at much lower magnetic fields. For a short-range  $\delta$ -impurity potential,  $\tau$  is identical to the single-particle momentum relaxation time,  $\tau_s$ , which determines the level broadening,  $(\Gamma/2)^2 = \hbar\omega_c \hbar / 2\pi\tau_s$  [31]. For a long-range potential, however, these two times can be very different [101] and knowledge about the level broadening does not necessarily imply knowledge about the mobility and vice versa. In fact, for a smooth potential with  $d \gg l_c$  we have  $(\Gamma/2)^2 = \left\langle [V_I(\mathbf{r}) - \langle V_I(\mathbf{r}) \rangle_{\mathbf{r}}]^2 \right\rangle_{\mathbf{r}}$ , which does not depend on  $B$ . In that case, we can determine the mobility from the transport cross-section calculated in Born approximation [31, 32]. Since the transport scattering time is momentum dependent, we take the low temperature limit, where the relevant scattering time is the one for electrons having Fermi momentum  $k_F = (2\pi n_e)^{1/2}$ . With a radially symmetric electron-impurity interaction potential for a single scatterer,  $u(\mathbf{r})$ , we obtain for the transport scattering time (see Appendix B)

$$\tau^{-1} = \frac{n_I m^*}{2\pi \hbar^3} \int_0^{2\pi} d\theta [1 - \cos(\theta)] |\tilde{u}(2k_F \sin(\theta/2))|^2, \quad (5.3)$$

with the Fourier transform  $u(\mathbf{k}) = \int d^2\mathbf{r} u(\mathbf{r}) \exp(-i\mathbf{r} \cdot \mathbf{k})$  and  $\tilde{u}(k) = u(|\mathbf{k}|)$ . In case of  $\delta$ -interaction and uniformly distributed strengths, we simply have  $\tilde{u}(k) = W/\sqrt{3}$  and the  $\cos(\theta)$  term in (5.3) vanishes. Without it (5.3) becomes the expression for  $\tau_s$  which proves the equivalence of  $\tau$  and  $\tau_s$  for short-range potentials. For long-range potentials, however, forward (small  $\theta$ ) scattering receives less weight since it hardly impairs the electron movement and  $\tau/\tau_s \gg 1$ . In order to model a situation comparable to the experiments of [17], we use material parameters for GaAs [102–104] ( $g^* = -0.44$  for the effective  $g$ -factor,  $m^* = 0.067m_e$  for the effective mass) and impurity parameters of  $W/\text{nm}^2 \simeq 4\text{eV}$  with a concentration of  $n_I = 3.2 \cdot 10^{11}\text{cm}^{-2}$  (e.g.  $N_I = 288$  for  $L = 300\text{nm}$  or  $N_I = 392$  for  $L = 350\text{nm}$ ). Assuming  $n_e \approx n_I$ , for the  $\delta$ -potential this yields a mobility of  $\mu_0 \simeq 10^3\text{cm}^2/\text{Vs}$ , whereas for  $d = 40\text{nm}$  ( $\approx$  spacer layer thickness)

we get  $\mu_0 \simeq 10^6 \text{cm}^2/\text{Vs}$  — a value which is reasonable for a high mobility sample such as a GaAs-GaAlAs heterojunction. The effect on the DOS and in particular the broadening of the lowest Landau levels is readily computed when having several additive scatterers, and thus a potential of the form

$$V(\mathbf{r}) = \sum_{i=1}^S V_i(\mathbf{r}) , \quad (5.4)$$

yielding an impurity concentration of  $n_I = S/L^2$ . In self-consistent Born approximation one finds for the width of the LL [73, 105]

$$\Gamma_0^2 = \frac{2n_I \text{Var}(V_i)}{\pi(d^2 + l_c^2)} , \quad (5.5)$$

where  $\text{Var}(V_i)$  is the variance of the distribution of impurity strengths. For predominantly short-range scattering, i.e.  $\delta$ -impurities, one can take the limit  $d \rightarrow 0$ , whereas for long-range scattering, i.e. a very smooth potential, we find the limit  $l_c \rightarrow 0$ , confirming the previous statement that the LL width becomes  $B$  independent. In the following we present calculations of the tunneling DOS in the lowest Landau level by averaging over at least 1000 samples in the non-interacting and the interacting system. In Figure 5.1 we show results for Gaussian and  $\delta$ -impurities for three system sizes  $L = 400, 500$ , and  $600\text{nm}$  for the non-interacting case as well as the interacting case. Within the accuracy of the calculation, we find the DOS to be independent of the system size, irrespective of interactions, as one would expect for such a disorder model as ours. Furthermore, in the interacting case, we find a strong suppression of the DOS at the Fermi level. The formation of this Coulomb gap and its non-criticality has been studied previously [25, 26, 77, 106]. In case of Gaussian-type impurities we also observe a strong reduction of the band broadening due to screening of the impurity potential, while the bandwidth in systems with  $\delta$ -type impurities is hardly affected by interactions.

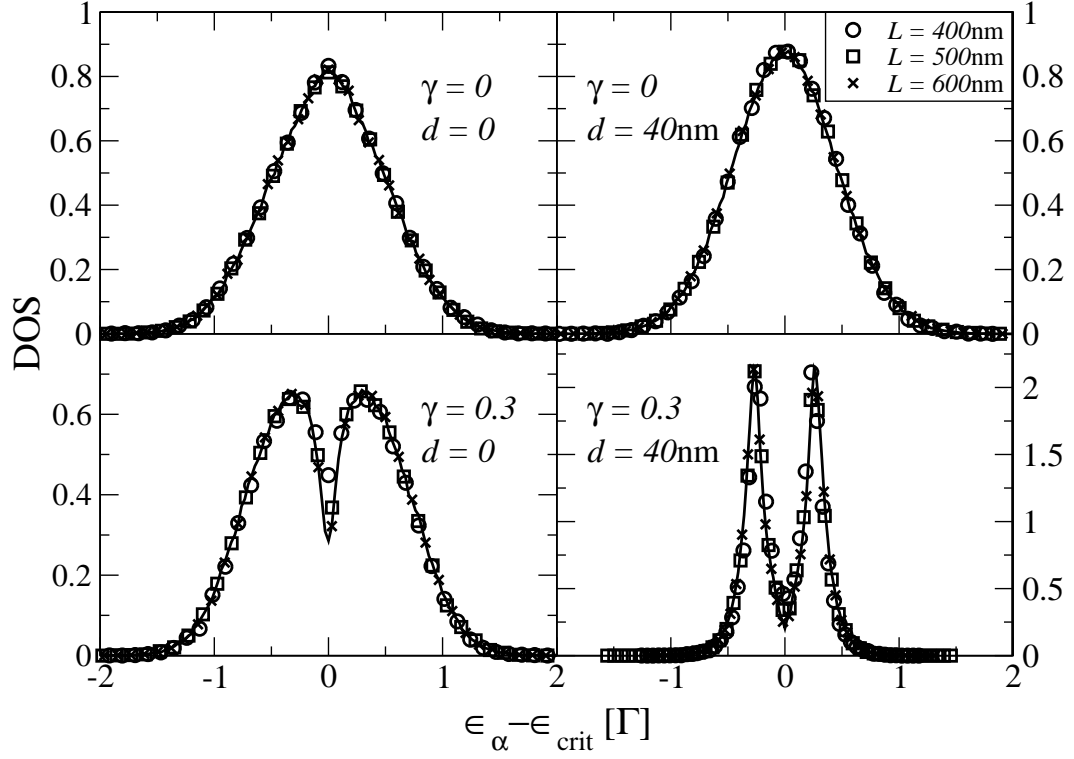


Figure 5.1: DOS at  $B = 3\text{T}$  for the lowest Landau level in a non-interacting (top row,  $\gamma = 0$ ) and a HF-interacting (bottom row,  $\gamma = 0.3$  at  $\nu = 1/2$ ) QH system for 3 system sizes as a function of energy  $\epsilon_\alpha$ , centred around the critical energy  $\epsilon_{\text{crit}}$  (centre of the band). The left column shows results for  $\delta$ -type impurities ( $d = 0$ ) with  $W/\text{nm}^2 = 2\text{eV}$ , the right column corresponds to Gaussian-type impurities with  $d = 40\text{nm}$  and  $W/\text{nm}^2 = 4\text{eV}$  ( $W/d^2 = 2.5\text{meV}$ ). The results in all cases are averaged over at least 1000 samples. Error bars are less than the symbol sizes. Note the strong Coulomb reduction of the DOS at the critical energy ( $\epsilon_\alpha = \epsilon_{\text{crit}}$ ) in the interacting cases.

## 5.2 Local Density of States

The local density of states (LDOS) is an interesting property since it is directly experimentally accessible via STS. The differential tunneling current between the STS tip and the sample is proportional to the density of existing states at a certain energy [107]. The LDOS is defined as the DOS weighted with the charge density at a spatial position  $\mathbf{r}$ , which reads as

$$\text{LDOS}(E, \mathbf{r}) = \sum_{\alpha} |\psi_{\alpha}(\mathbf{r})|^2 \delta(E - E_{\alpha}) , \quad (5.6)$$

which indeed obeys  $\int d^2\mathbf{r} \text{LDOS}(E, \mathbf{r}) = \sum_{\alpha} \delta(E - E_{\alpha}) = \rho(E)$ , where  $\rho(E)$  is the tunneling DOS as introduced in the previous section. In practice, however, the measured LDOS is broadened by temperature as well as an AC modulation voltage applied when using the lock-in technique in order to eliminate noise in the image [108]. The energy window can then be described by a semi-circle around  $E$  [108] with the broadening  $\Delta E$ , which is usually of the order of 1meV. Thus, the LDOS can be regarded as the charge density in a small energy interval and allows to study the charge distribution in the three dimensions (two spatial plus energy) experimentally and theoretically [108], as depicted in Figure (5.2).

## 5.3 Chemical Potential and Compressibility

The electronic compressibility  $\kappa = (\partial n_e / \partial \mu) / n_e^2$  reflects the ability of the 2DES to absorb electrons when changing the chemical potential. With  $\mu = \partial E_{\text{tot}} / \partial N_e$ , we find  $\partial \mu / \partial n_e = L^2 (\partial^2 E_{\text{tot}} / \partial N_e^2)$ . Hence, for finite sample calculations, we can obtain  $\kappa$  from  $E_{\text{tot}}(N_e)$  using

$$\frac{\partial \mu}{\partial n_e} \approx L^2 [E_{\text{tot}}(N_e + 1) - 2E_{\text{tot}}(N_e) + E_{\text{tot}}(N_e - 1)] . \quad (5.7)$$

Alternatively, at  $T = 0$ , we can compute the change in the chemical potential for  $N_e$  electrons by noting that the Fermi energy  $\epsilon_F(N_e) = \mu(N_e)$ . Thus we immediately have

$$\frac{\partial \mu}{\partial n_e} = L^2 [\epsilon_F(N + 1) - \epsilon_F(N)] . \quad (5.8)$$

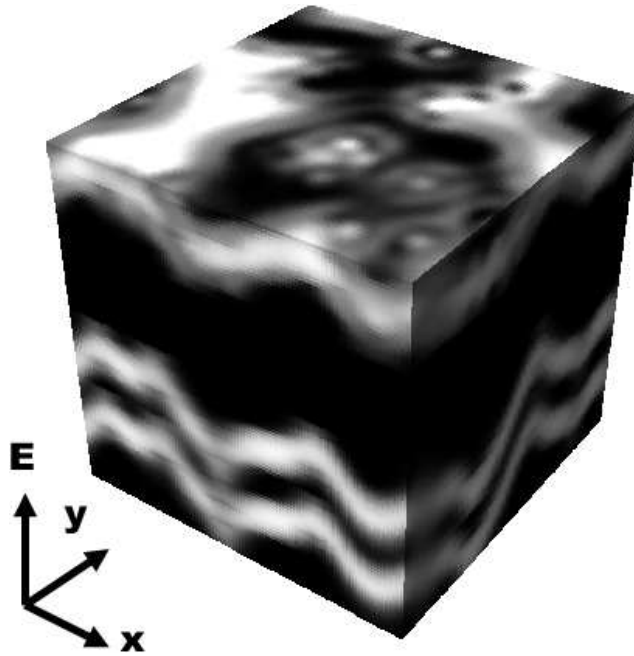


Figure 5.2: LDOS of non-interacting electrons at  $B = 5\text{T}$  as a function of position *and* energy for a system of size  $L = 300\text{nm}$ . The filling factor at the top corresponds to  $\nu \approx 3$ . White areas indicate high values of the LDOS.

This turns out to be numerically more stable than (5.7) and shall be used in the following. We would like to remark that for obvious reasons the measurement of the electronic compressibility is experimentally realised by changing the chemical potential instead of changing the electron number density. In our calculation, changing the number density is easier to control and therefore we make use of the inverse relation between the two functions.

As pointed out in Section 3.1 the distribution of levels for non-interacting electrons in a smooth potential can be approximately described by the distribution of energies in the disorder potential, which for a smooth potential must fall off in the tails. Since the compressibility is proportional to the tunneling DOS [28], in the region of highly localised states, it takes more energy to accommodate a new electron, and thus the compressibility is low. On the other hand, in a region of delocalised states where the



levels are more dense, a newly added electron is much more easily 'absorbed' and  $\kappa$  is high. At best we expected  $\kappa$  to exhibit a fan-like structure in the  $(B, n_e)$  diagram. In fact, the resonances visible in  $\kappa$  need not align with slopes equal to integer filling factors [109].

In the interacting case,  $\kappa$  is proportional to the TDDOS and the inverse screening length, and is associated with the collective relaxation after adding a new electron. Similar to the non-interacting case, we anticipate the highest  $\kappa$  in the band tails and lowest in the regime of extended states. We expect the neutralisation of the constant background to be more effective for a homogeneously distributed charge, i.e. if the Fermi level lies in the regime of extended states. We finally note that experimentally the change of the chemical potential is detected when changing the back gate voltage and hence the electron density at constant  $B$  [17, 18].

## 5.4 Participation Ratio

The participation ratio  $P_\alpha$  is defined as the inverse of the variance of the charge density in the state  $\alpha$ ,

$$P_\alpha = \left( L^2 \int d^2\mathbf{r} |\psi_\alpha(\mathbf{r})|^4 \right)^{-1}. \quad (5.9)$$

Large values of  $P_\alpha$  correspond to spatially extended states, while low values indicate a confined state [38, 39]. This is intuitively understood by the fact that the density of an extended state varies much less over space than a highly localised one. Thus  $P_\alpha$  is a measure of the degree of localization and may be computed in our system as

$$P_\alpha = \frac{l_c^2}{L^2} \sum_{\substack{n, n', m, m' \\ k, k', l, l'}} \sum_{\mathbf{q}} (\mathbf{C}_{n,k}^\alpha)^* \mathbf{C}_{n',k'}^\alpha (\mathbf{C}_{m,l}^\alpha)^* \mathbf{C}_{m',l'}^\alpha S_{n,k;n',k'}(\mathbf{q}) S_{m,l;m',l'}(-\mathbf{q}). \quad (5.10)$$

It has been shown that unscreened HF-interactions do not alter the critical exponent  $\tilde{\nu}$  while renormalising the dynamical scaling exponent to  $z = 1$  [25, 26, 110], which for instance characterises the scaling of the conductivity tensor in an applied AC field. The former has led to the conclusion that the HF theory should be within the same

universality class as the non-interacting theory. In fact, the reason for that has been well explained [111] with an additional global symmetry named  $\mathcal{F}$  invariance which is absent in case of short-ranged interactions and non-interacting electrons. As a check to our HF results, we calculate  $P_\alpha$  of spinless electrons in the lowest Landau level for the same samples as in Section 5.1. The participation ratio is expected to obey the single parameter scaling form [112]

$$P_\alpha = L^{D(2)-2} \Pi \left( L^{1/\tilde{\nu}} |\epsilon_\alpha - \epsilon_{\text{crit}}| \right), \quad (5.11)$$

with the anomalous diffusion coefficient  $D(2) \approx 1.6$  — related to the multifractal character of the critical states [45, 113, 114] — and the critical exponent  $\tilde{\nu} \approx 2.3$  [42]. Figure 5.3 shows the scaling function for the non-interacting and an interacting system at filling factor  $\nu = 1/2$ . The scaling function collapses reasonably well onto a single curve for both non-interacting and HF-interacting systems. We find  $D(2) = 1.62 \pm 0.10$  as typical average over both HF- and non-interacting systems as shown in Figure 5.4. This demonstrates the irrelevance of interactions and the type of disorder for the multifractal dimension of the critical state in very good agreement with previous results [26, 45, 115]. We note that this result might be limited to HF interactions. Multifractality has been argued to be absent (i.e.  $D(2)=2$ ) in case of spinless electrons with Coulomb interactions [116]. A similar fit in the tails of  $P_\alpha$  is numerically less accurate but still yields estimates for  $\tilde{\nu}$  between 2 and 2.4, compatible with the expected value  $2.34 \pm 0.04$  [34, 42].

## 5.5 Screening

The probably most important manifestation of electron-electron interactions for our system is the screening of the impurity potential. A positive charge placed in the electron gas attracts the negatively charged electrons which in turn reduce the field of the positive test charge. Similarly for a negative charge, electrons will be pushed away from it leaving a hole which is then positively charged, compared to the average charge density in the system. The electrons themselves can also be regarded as negative test

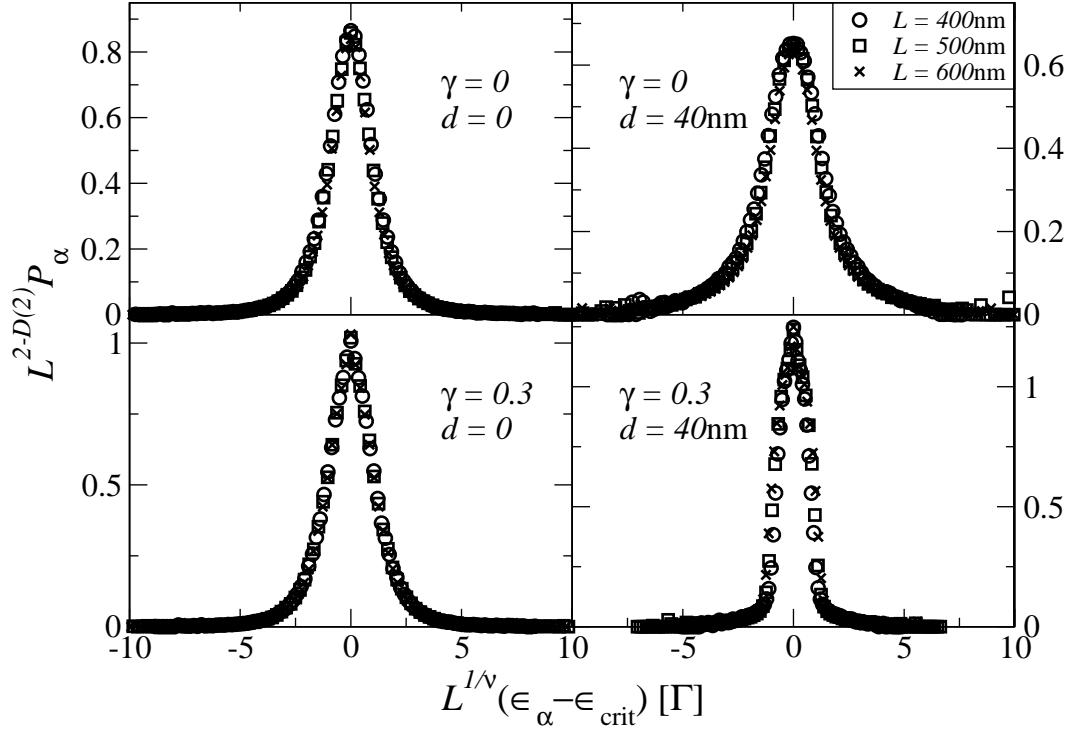


Figure 5.3: Scaling functions of the participation ratio  $P_\alpha$  at  $B = 3\text{T}$  for the non-interacting (top row,  $\gamma = 0$ ) and the HF-interacting (bottom row,  $\gamma = 0.3$  at  $\nu = 1/2$ ) systems averaged over at least 1000 samples and using  $D(2) = 1.62$ ,  $\tilde{\nu} = 2.34$ . The left column shows results for  $\delta$ -type impurities ( $d = 0$ ), the right column corresponds to Gaussian-type impurities with  $d = 40\text{nm}$ . Values for  $L$  have been scaled by the magnetic length. Fluctuations in the tails are due to a smaller number of data points.

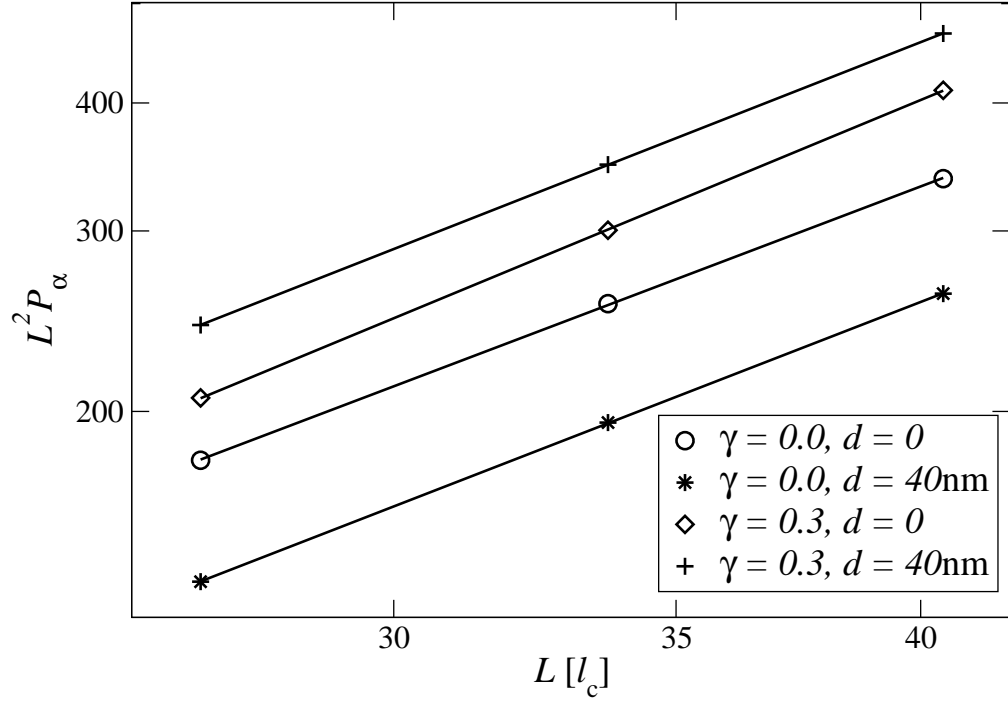


Figure 5.4: Power-law fit of the system size dependence of  $P_\alpha$  at  $B = 3\text{T}$  according to (5.11) for non-interacting and HF-interacting systems around  $\epsilon_\alpha = \epsilon_{\text{crit}}$ .  $\circ$  and  $\diamond$  denote  $\delta$ -type impurities ( $d = 0$ ) whereas  $*$  and  $+$  show results for Gaussian-type impurities with  $d = 40\text{nm}$ . The error bars for the data points are smaller than the symbol sizes. The  $D(2)$  values are  $1.57 \pm 0.2$  ( $\gamma = 0, d = 0$ ),  $1.6 \pm 0.1$  ( $\gamma = 0, d = 40\text{nm}$ ),  $1.7 \pm 0.1$  ( $\gamma = 0.3, d = 0$ ),  $1.62 \pm 0.05$  ( $\gamma = 0.3, d = 40\text{nm}$ ). Values for  $L$  are scaled by the magnetic length.

charges, hence the density will acquire a certain 'self-consistent' distribution. For a free electron gas which can adapt to any such test charge, this compensation process will continue until the field of test charges plus the field of the electrons completely cancels each other. This is often called perfect screening. The condition for the charge density,  $n_e(\mathbf{r})$ , to perfectly screen an impurity potential is an electrostatic problem. The charge density is the source of a field  $\phi(\mathbf{r})$ , which is given by

$$\phi(\mathbf{R}) = e \int d^3\mathbf{R}' \frac{n_e(x', y') \delta(z')}{4\pi\epsilon\epsilon_0 |\mathbf{R} - \mathbf{R}'|} . \quad (5.12)$$

The potential due to the impurities on the other hand is given by  $V(\mathbf{r})$  and shall be canceled by the electrons. Thus, the perfect screening condition is

$$V(\mathbf{r}) = -e\phi(x, y, 0) = -\frac{e^2}{4\pi\epsilon\epsilon_0} \int d^2\mathbf{r}' \frac{n(\mathbf{r}') - n_B}{|\mathbf{r}' - \mathbf{r}|} \quad (5.13)$$

where  $n_B$  is a constant background charge which in the following shall guarantee overall charge neutrality in the system, i.e. we choose  $n_B = \langle n_e(\mathbf{r}) \rangle$ . Splitting the charge density into two parts, a mean density and the fluctuations around the mean,  $n_e(\mathbf{r}) = \langle n_e(\mathbf{r}') \rangle_{\mathbf{r}'} + \delta n_e(\mathbf{r})$ , the background charge cancels away and only the fluctuations remain important for screening. A Fourier transform now yields

$$V(\mathbf{q}) = \int \frac{d^2\mathbf{r}}{L^2} e^{-i\mathbf{q}\cdot\mathbf{r}} V(\mathbf{r}) = -\frac{e^2}{4\pi\epsilon\epsilon_0} \iint d^2\mathbf{r} d^2\mathbf{r}' e^{-i\mathbf{q}\cdot\mathbf{r}} \frac{\delta n_e(\mathbf{r}')}{L^2 |\mathbf{r}' - \mathbf{r}|} \quad (5.14)$$

$$= -\frac{e^2}{4\pi\epsilon\epsilon_0} \iint d^2\mathbf{u} d^2\mathbf{r}' e^{-i\mathbf{q}\cdot(\mathbf{u}+\mathbf{r}')} \frac{\delta n_e(\mathbf{r}')}{L^2 |\mathbf{u}|} = -\frac{e^2}{2\epsilon\epsilon_0 |\mathbf{q}|} \delta n_e(\mathbf{q}) , \quad (5.15)$$

where  $\mathbf{q} \neq 0$  due to the background charge, avoiding a divergence on the right hand side. The  $1/\mathbf{q}$  can be brought over to the other side, giving an explicit expression for the charge density obeying the perfect screening condition. In contrast to the 2D result, a Fourier transform of the 3D Coulomb potential yields  $1/\mathbf{q}^2$ , and the inverse Fourier transform of the above equation is the Laplace equation,  $n_e^{3D}(\mathbf{R}) \propto \Delta V(\mathbf{R})$ . In 2D,

however, the 3D Laplace equation does not hold. Instead we find

$$\delta n_e(\mathbf{r}) = \sum_{\mathbf{q}} e^{i\mathbf{q}\cdot\mathbf{r}} \delta n_e(\mathbf{q}) = -\frac{2\epsilon\epsilon_0}{e^2} \sum_{\mathbf{q}} e^{i\mathbf{q}\cdot\mathbf{r}} |\mathbf{q}| V(\mathbf{q}) = -\frac{2\epsilon\epsilon_0}{e^2} \sum_{\mathbf{q}} e^{i\mathbf{q}\cdot\mathbf{r}} \frac{\mathbf{q}^2}{|\mathbf{q}|} V(\mathbf{q}) \quad (5.16)$$

$$= -\frac{2\epsilon\epsilon_0}{e^2} \sum_{\mathbf{q}, \mathbf{q}'} e^{i\mathbf{q}'\cdot\mathbf{r}} \frac{\mathbf{q}^2}{|\mathbf{q}'|} V(\mathbf{q}) \delta_{\mathbf{q}, \mathbf{q}'} = -\frac{2\epsilon\epsilon_0}{e^2} \sum_{\mathbf{q}, \mathbf{q}'} \frac{e^{i\mathbf{q}'\cdot\mathbf{r}}}{|\mathbf{q}'|} \int d^2\mathbf{r}' \Delta_{\mathbf{r}'} V(\mathbf{r}') e^{-i\mathbf{q}\cdot\mathbf{r}'} \delta_{\mathbf{q}, \mathbf{q}'} \quad (5.17)$$

$$= -\frac{2\epsilon\epsilon_0}{e^2} \int d^2\mathbf{r}' \sum_{\mathbf{q}} \frac{e^{i\mathbf{q}\cdot(\mathbf{r}-\mathbf{r}')}}{|\mathbf{q}|} \Delta_{\mathbf{r}'} V(\mathbf{r}') = -\frac{4\pi\epsilon\epsilon_0}{e^2} \int d^2\mathbf{r}' \frac{\Delta_{\mathbf{r}'} V(\mathbf{r}')}{|\mathbf{r}-\mathbf{r}'|} . \quad (5.18)$$

This expression may be defined as  $\delta n_e(\mathbf{r}) = \tilde{\Delta}_{\mathbf{r}} V(\mathbf{r})$ , with a redefined Laplace operator which we will pick up on in a later section. In summary, in the presence of a potential  $V(\mathbf{r})$ , an interacting, unrestricted 2DEG will adapt according to the quasi-Laplace equation. In presence of a magnetic field this cannot always be satisfied due to the quantising nature of the magnetic field, as we will see in the following chapters.

## Chapter 6

# Electronic Compressibility

### 6.1 Compressibility Patterns

In this chapter we address single electron transistor (SET) electrometer measurements on 2DEGs in high mobility QH samples [17,18]. The results from these experiments tell a very convincing story about the relevance of electron-electron interaction effects and hence question the widely used simplified single particle description of the IQHE. After an account of the experimental results and explanation, we will present our numerical calculations and show that the experimental features can be well-reproduced within a model of HF-interacting electrons. Thereby we give strong theoretical support for Coulomb blockade effects as well as linear and non-linear screening within the IQHE.

The compressibility measurements are carried out with an SET tip hovering over the 2DEG. A back gate voltage,  $V_{BG}$ , is applied to the sample and by varying  $V_{BG}$  the authors of [17] were able to detect the local change of the chemical potential,  $\delta\mu/\delta V_{BG}$ . The measurements were done over a wide range of magnetic fields,  $B$ , and carrier densities,  $n_e$ . The measured change of the chemical potential, which is proportional to the inverse electronic compressibility,  $\kappa^{-1}$ , as shown in Section 5.3, provides direct information about the degree of localization of QH states. As we demonstrate in the following chapters, single particle models fail to describe the results obtained from these

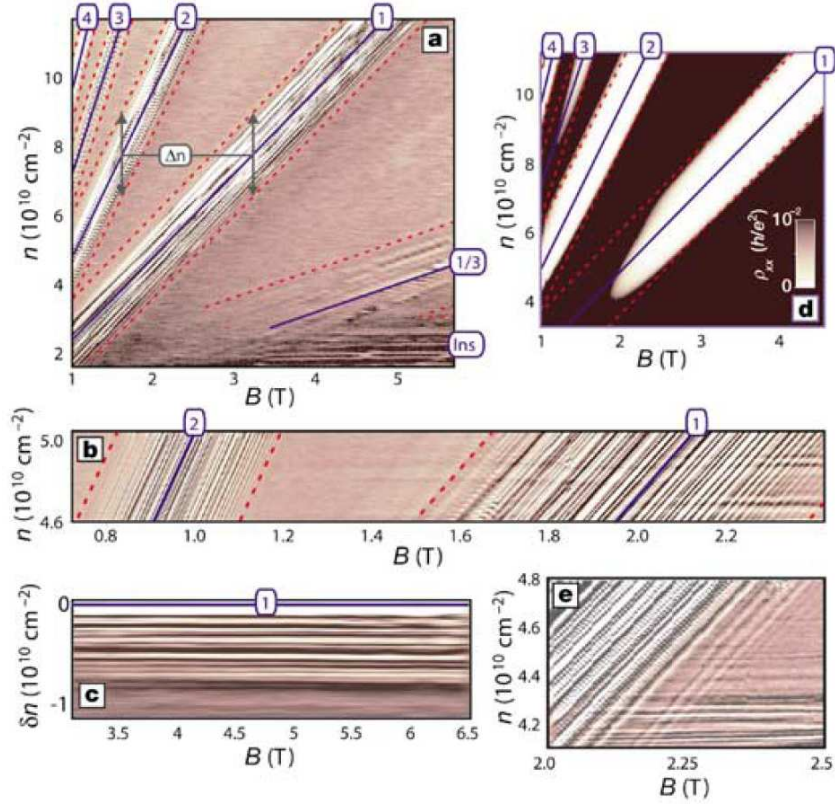


Figure 6.1: Measurement of the inverse electronic compressibility ( $\delta\mu/V_{\text{BG}}$ ) at an arbitrary position above the 2DEG as a function of magnetic field and carrier density [17]. For a detailed discussion see text.

measurements. Electron-electron interaction effects have to be considered in order to account for the observed effect. This might bear implications for the phase diagram of the IQH regime and will be put on a theoretical and numerical footing in the sections to follow. In Figure 6.1 we show the compressibility measurements of Ilani et al. [17]. Figures 6.1(a), 6.1(b), 6.1(c), and 6.1(e) show results from the SET compressibility measurements as a function of magnetic field and carrier density. The characteristic compressibility patterns around integer filling factors are believed to be due to charging of localised states at the Landau band edges. Figure 6.1(d) is a transport measurement of the longitudinal resistivity,  $\rho_{xx}$ , in the same parameter range and provides evidence that the compressibility patterns appear in fact only where localised states exist. Let us



recall the core results of [17] most relevant to our investigation. The compressibility in the  $(B, n_e)$ -plane

- (i) exhibits only little variation in regions close to the QH transitions at half-integer filling factors,
- (ii) show a strong variation between Landau bands at integer fillings which by virtue of the relation  $n_e = \nu e B / h$  correspond to lines of constant slope,
- (iii) these regions of strong variation seem to have a width which is  $B$  and Landau level index independent,
- (iv) within these stripes, thin lines of equal slope  $j e B / h$ ,  $j = 0, 1, \dots$  can be identified,
- (v) similar patterns are found for any position of the SET tip within the sample area.

Ilani and coworkers [17] argued that each of the small lines surrounding the integer filling factors reflects one particular localised state within the sample. Therefore it has been concluded from the measurements that above a certain minimal magnetic field, where the 2DEG is mostly interaction dominated, there exist a fixed number of localised states independent of magnetic field or Landau level index. This number of localised states only depends on the strength of the impurity potential within the plane of the 2DEG. In the following sections we will investigate whether such patterns can be reproduced by taking into account the electron-electron interactions in a mean-field approach. Moreover, we try to describe this effect more quantitatively.

## 6.2 Coulomb Blockade

In order to understand the experimental results we need to focus on the physics of the 2DEG near the Landau band edges. As opposed to the band centre, in this regime

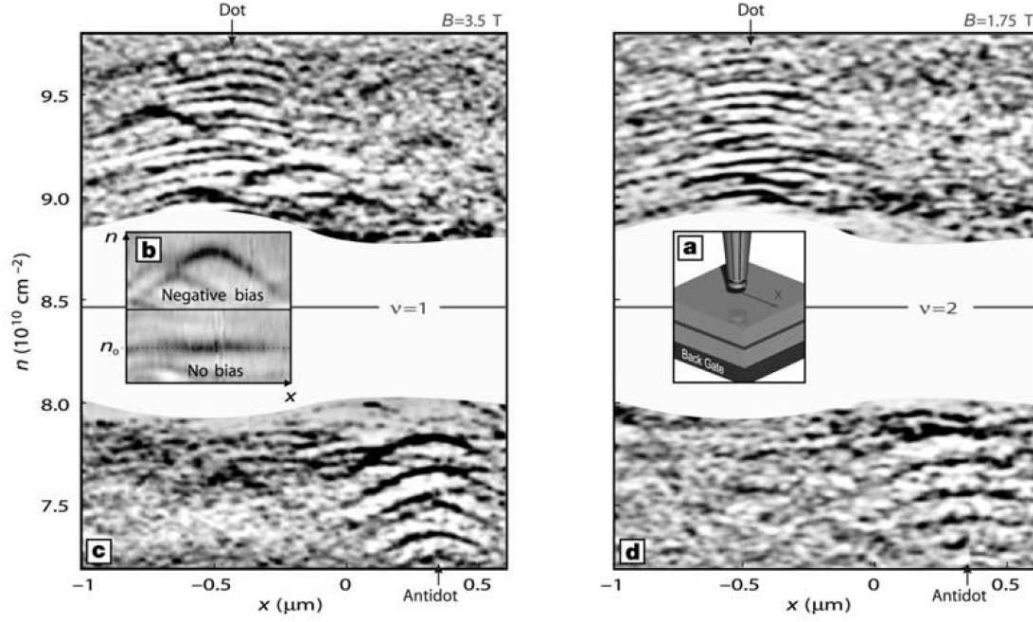


Figure 6.2: Spatial compressibility scans visualising localised states [17]. Dark regions correspond to low compressibility, bright regions show high compressibility. For a detailed discussion see text.

the measured compressibility exhibits very strong fluctuations as a function of electron density which is due to sharp jumps in the chemical potential upon varying the carrier density. A clearer picture of what the microscopic situation is can be obtained by a spatially resolved scan of  $\kappa^{-1}$ . Unlike the fixed-position  $(B, n_e)$ -scans, the SET tip will thereby pick up the spatial variations of the chemical potential change. In Figure 6.2 we present cross-section scans of the inverse electronic compressibility through the sample as measured by Ilani and coworkers. The measurement shows the compressibility  $\kappa^{-1}$  as a function of  $x$ -coordinate and carrier density,  $n_e$ . Spatially localised jumps of the chemical potential can be clearly identified which form bent segments within the  $(x, n_e)$ -plane. It is argued that these jumps are fingerprints of local charge accumulation and allow to conclude that quantum-dot-like structures [117] of electrons (near an empty Landau band) or holes (near a full Landau band) must be formed within the sample. A quantum dot (QH) is a structure of spatially confined electronic states. The multitude of lines

in the compressibility originating from the dots are indications of Coulomb blockade effects and provide information on the position, charging as well as spatial extent of the dots. Since the charge is confined to a small region within the sample, Coulomb repulsion amongst the particles requires a comparably large amount of energy for adding or removing an electron to or from the dot. An increase in the number of electrons is thus accompanied by equidistant jumps in the chemical potential. The bending of the compressibility patterns is a feature of the SET tip bias which acts as an additional potential at the tip site. As the tip scans across a particular dot, it affects its charging condition as a function of distance to the centre which results in the observed arc-like distortions.

Now we want to investigate whether our model is capable of producing dot spectra as found in the experiment. The change of the local chemical potential with respect to the electron density can be computed for our system by noting that the local chemical potential is the functional derivative of the total energy with respect to the electron density as a function of position

$$\mu(\mathbf{r}) = \frac{\delta E_{\text{tot}}[n]}{\delta n_e(\mathbf{r})} , \quad (6.1)$$

where the total energy functional reads

$$E_{\text{tot}}[n] = \iint d^2\mathbf{r} d^2\mathbf{r}' \frac{n_e(\mathbf{r})n_e(\mathbf{r}')}{|\mathbf{r} - \mathbf{r}'|} . \quad (6.2)$$

Thus, the local chemical potential yields

$$\mu(\mathbf{r}) = \int d^2\mathbf{r}' \frac{n_e(\mathbf{r}')}{|\mathbf{r} - \mathbf{r}'|} . \quad (6.3)$$

We check the result by writing  $n_\alpha(\mathbf{r})$  for the charge density of state  $\alpha$  and integrate over space which yields the expected result  $\int d^2\mathbf{r} \mu(\mathbf{r}) n_\alpha(\mathbf{r}) = \mu_\alpha = \epsilon_\alpha$ . Hence, we identify the local chemical potential with the electrostatic potential due to the electrons in the 2DES at the position  $\mathbf{r}$ . The expression for the electrostatic potential of the 2DES reads

$$\phi(\mathbf{r}) = L^{-2} \sum_{\sigma} \sum_{n,k,n',k'} \sum_{\mathbf{q}} V_C(\mathbf{q}) \mathbf{D}_{n,k;n',k'}^{\sigma} S_{n,k;n',k'}(\mathbf{q}) \exp(-i\mathbf{q}\mathbf{r}) \quad (6.4)$$

and the local inverse electronic compressibility can be evaluated as

$$\kappa^{-1}(\mathbf{r}) \propto \mu^{N+1}(\mathbf{r}) - \mu^N(\mathbf{r}) \propto \phi^{N+1}(\mathbf{r}) - \phi^N(\mathbf{r}). \quad (6.5)$$

We have calculated  $\kappa^{-1}(\mathbf{r})$  for the lowest two Landau levels for a system of size  $L = 500\text{nm}$  without spin as a function of position and carrier density at magnetic field  $B = 2\text{T}$ . The SET tip potential,  $V_{\text{tip}}(\mathbf{r})$ , has been approximated by a Gaussian function

$$V_{\text{tip}}(\mathbf{r}) = \frac{w_{\text{tip}}}{\pi d_{\text{tip}}^2} \exp[-(\mathbf{r} - \mathbf{R}_{\text{tip}})^2/d_{\text{tip}}^2] \quad (6.6)$$

with  $w_{\text{tip}}/\text{nm}^2 = 6\text{meV}$  and  $d_{\text{tip}} = 5\text{nm}$ . The sample is then "probed" along the  $x$ -axis at  $\mathbf{R}_{\text{tip}} = (i/50)L$ , where  $i = 1, \dots, 50$ . For each position of the tip the total potential has to be evaluated and a complete HF run is carried out since the tip affects the electron density at each position differently. The results are presented in Figure 6.3. We find remarkable agreement with the experimental results as shown in Figure 6.2. Distinct charging patterns appear at the Landau band edges, whereas in the centre of the bands the features are weaker. Thus, we have shown that our model 2DEG is able to exhibit Coulomb blockade patterns and therefore we also expect the  $(B, n_e)$ -calculations to carry charging patterns similar to the experimental results.

### 6.3 Numerical Results in the $(B, n_e)$ -Plane

In what follows, we present our numerical results on the electronic compressibility in the  $(B, n_e)$ -plane as outlined in Chapter 5.5. We are using a sample of size  $L = 300\text{nm}$  at magnetic fields between  $B = 0.2\text{T}$  and  $B = 6\text{T}$  and take into account the two lowest, spin-split Landau levels. In the next section, we present the results obtained for a system of non-interacting electrons. After that, we switch on Coulomb interactions. We will discuss the differences between the two cases and compare with the experimental results. Then we will put the focus on the underlying screening mechanism. We investigating the charge distribution and how the electron-electron interactions affect the effective

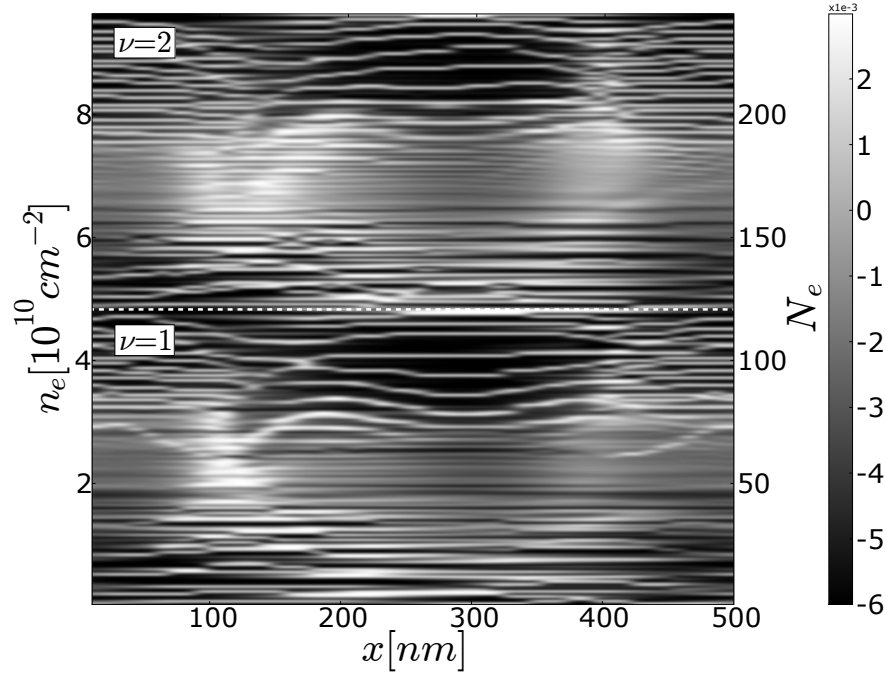


Figure 6.3: Inverse electronic compressibility  $\kappa^{-1}$  for a HF-interacting system of size  $L = 500\text{nm}$  as a function of position  $x$  and electron density  $n_e$  in the two lowest Landau levels without spin. The  $y$  coordinate has been fixed at  $250\text{nm}$ . The patterns correspond to jumps in the chemical potential due to charging of local charge puddles (see text for further details).

potential felt by the individual electrons. The Coulomb and the exchange term will be discussed individually.

Figure 6.4 shows our results for the *inverse* compressibility  $\kappa^{-1}$  of non-interacting ( $\gamma = 0$ ) electrons in the two lowest orbital Landau levels, including spin. Darker areas in the plot reflect states of higher compressibility, hence a more delocalised regime. Lighter areas are more strongly localised states. Due to the weak Zeemann splitting, we do not observe the two spin bands separately. Rather, both bands remain nearly degenerate and lie almost on top of each other. Hence, we only find a single, very strongly incompressible region between the first and the second orbital Landau level at  $\nu = 2$ . This broad line is due to the band gap and the highly localised states at the band

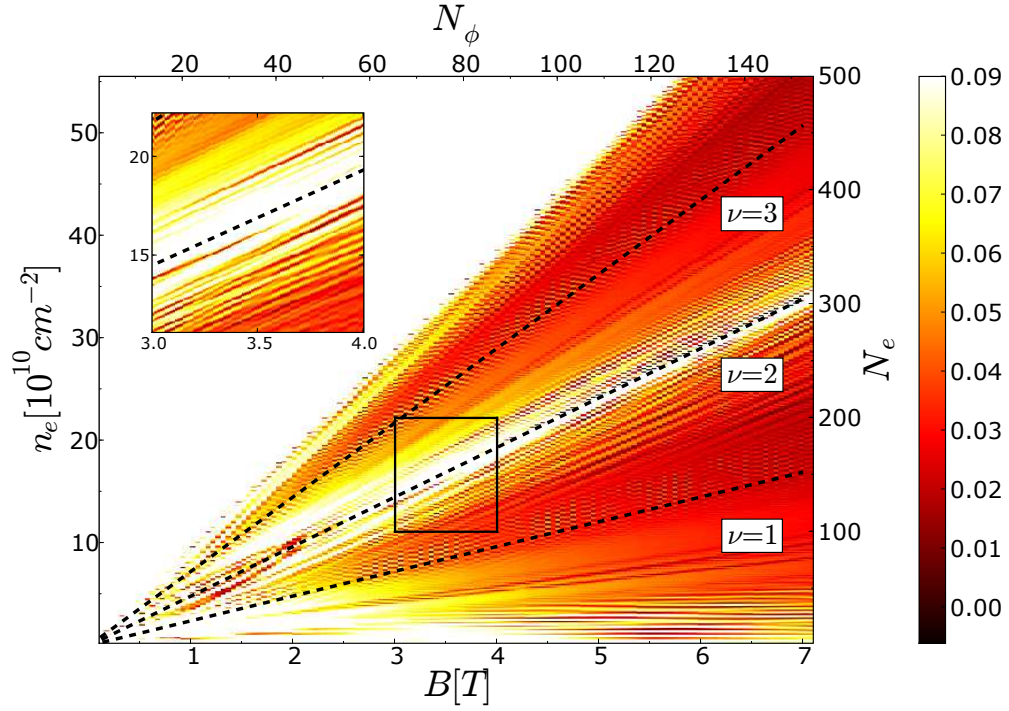


Figure 6.4: Inverse electronic compressibility  $\kappa^{-1}$  for a non-interacting system of size  $L = 300\text{nm}$  with disorder strength  $W/d^2 = 2.5\text{meV}$  in the  $(B, n_e)$ -plane. The color scale spans two standard deviations around the average of  $\kappa^{-1}$ . The inset shows more detailed results for the region marked by a black rectangle.

edges. Other less pronounced lines are visible along different filling factors, seemingly mostly emanating from  $(0, 0)$ . Some lines even appear to have a varying slope as shown in the inset of Figure 6.4. We interpret these features as the aforementioned fingerprints of scattering resonances in the disorder potential [109] which do not necessarily need to align with constant filling factors. Moreover, we clearly observe an increasing number of those lines with increasing magnetic field. At  $\nu = 0$  and 4, the compressibility is again low.

We next include interaction with  $\gamma = 0.3$ . This is not yet the full  $\gamma = 1$  Coulomb term, but the results are numerically more stable while at the same time not being dramatically different from  $\gamma = 1$ . Furthermore,  $\gamma < 1$  is essentially equivalent

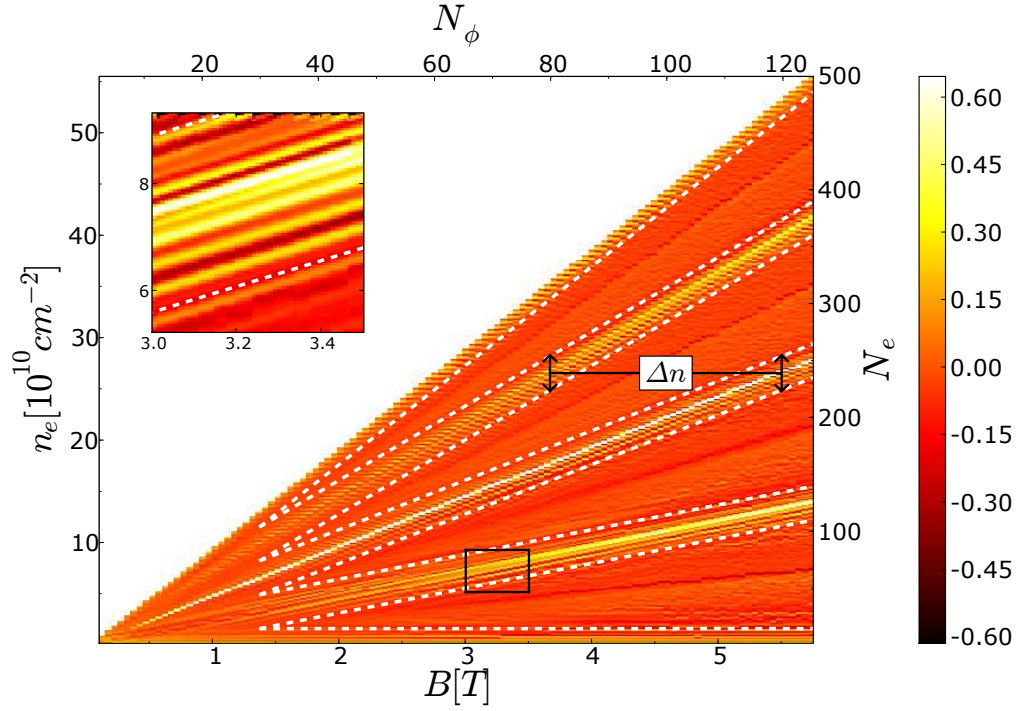


Figure 6.5: Inverse electronic compressibility  $\kappa^{-1}$  for a HF-interacting system of size  $L = 300\text{nm}$  with disorder strength  $W/d^2 = 1.25\text{meV}$  in the  $(B, n_e)$ -plane. The dotted lines show estimates based on a perfect screening condition (see text for details). The color scale spans two standard deviations around the average of  $\kappa^{-1}$ . The inset shows more detailed results for the region marked by a black rectangle.

to increased disorder with the full Coulomb interaction present. Figures 6.5, 6.6, and 6.7 show results in the  $(B, n_e)$ -plane for an interacting system of size  $L = 300\text{nm}$  with disorder strengths  $W/d^2 = 1.25, 2.5$ , and  $3.75\text{meV}$ , respectively, at fixed impurity range  $d = 40\text{nm}$ . We observe that the exchange interaction results in an effective  $g$ -factor substantially enhanced from its bare value [118–120], leading to a clear separation of the two spin bands. This yields two additional strongly incompressible stripes at  $\nu = 1$  and  $\nu = 3$ , indicated by particularly high  $\kappa^{-1}$  values. Quite different from the non-interacting case, we find that most of the incompressible lines form groups which align parallel in the  $(B, n_e)$ -plane along integer filling factors. Above a certain minimal

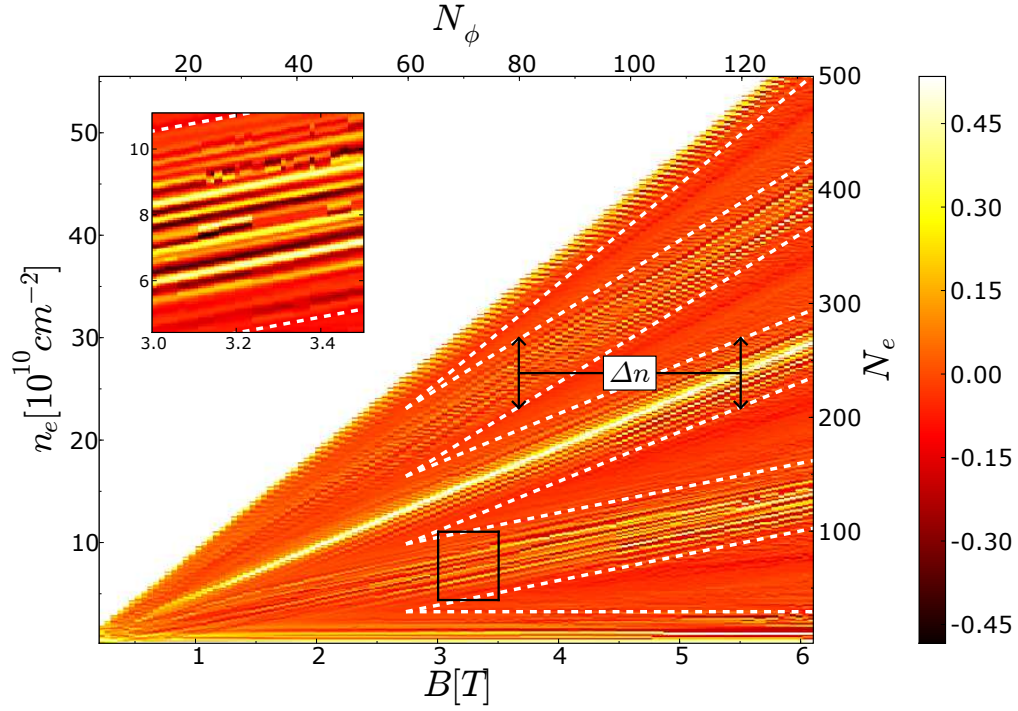


Figure 6.6: Inverse electronic compressibility as in Figure 6.5 but with  $W/d^2 = 2.5 \text{ meV}$ .

magnetic field, the width of these groups — the number of the lines — is independent of the magnetic field and Landau level, forming *incompressible* stripes of constant width around integer filling factors. Overall, this behaviour is strikingly similar to the effects observed in the experiments of [17, 18]. Outside the stripes, there is hardly any feature in the compressibilities except directly at the QH plateau-to-plateau transitions at half-integer fillings where a small increase in compressibility is discernible. In these areas between incompressible stripes, the inverse compressibility tends to have a very low or even negative value, which relates to a very high or negative TTDOS, respectively. This effect has been predicted [121] and observed experimentally [22, 122] and is a signature of the exchange interaction. From the proportionality between compressibility and the screening length, we can conclude to observe strong overscreening in the areas of negative compressibility. We attribute this to the tendency of the HF-interacting



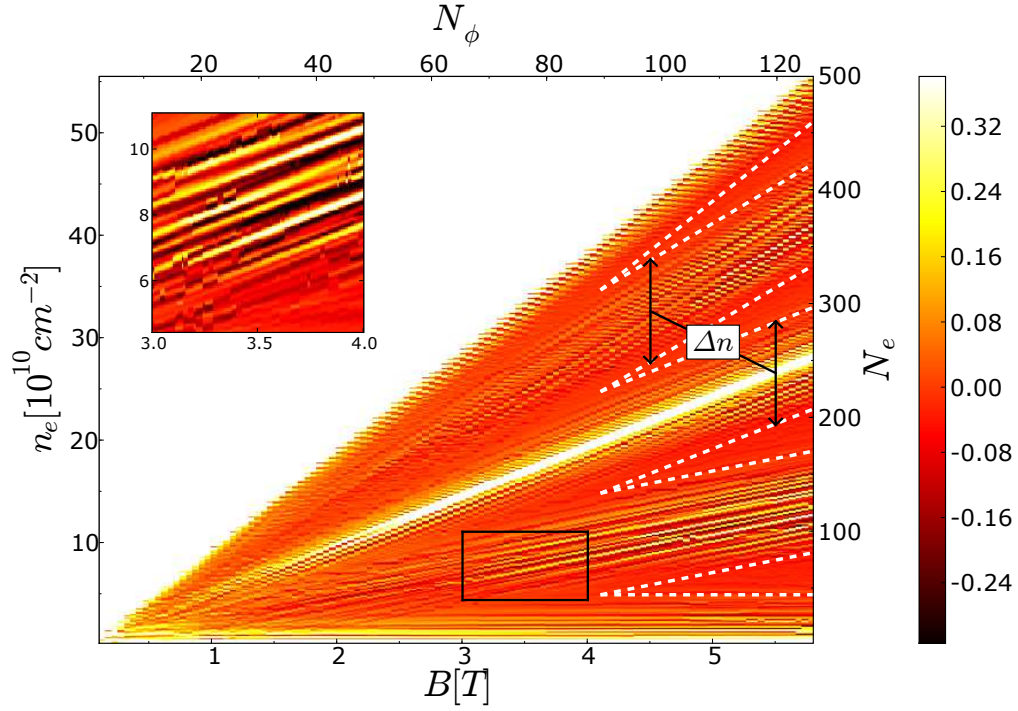


Figure 6.7: Inverse electronic compressibility as in Figure 6.5 but with  $W/d^2 = 3.75\text{meV}$ .

2DES to form a charge density wave [94, 123]. Furthermore, when comparing Figures 6.5, 6.6, and 6.7 we find that the width of the incompressible stripes increases with increasing disorder strength  $W/d^2$ .

## 6.4 Charge Density Distribution and Screening

We will now focus on the behaviour of the electron density in presence of electron-electron interactions and study the screening effect outlined in Section 5.5 numerically. The spatial distribution of the total electronic density

$$n(\mathbf{r}) = \sum_{\sigma} \sum_{\alpha=1}^M |\psi_{\alpha}^{\sigma}(\mathbf{r})|^2 \quad (6.7)$$

$$= L^{-2} \sum_{\sigma} \sum_{n,k,n',k'} \sum_{\mathbf{q}} \mathbf{D}_{n,k;n',k'}^{\sigma} S_{n,k;n',k'}(\mathbf{q}) \exp(-i\mathbf{q}\mathbf{r}) \quad (6.8)$$

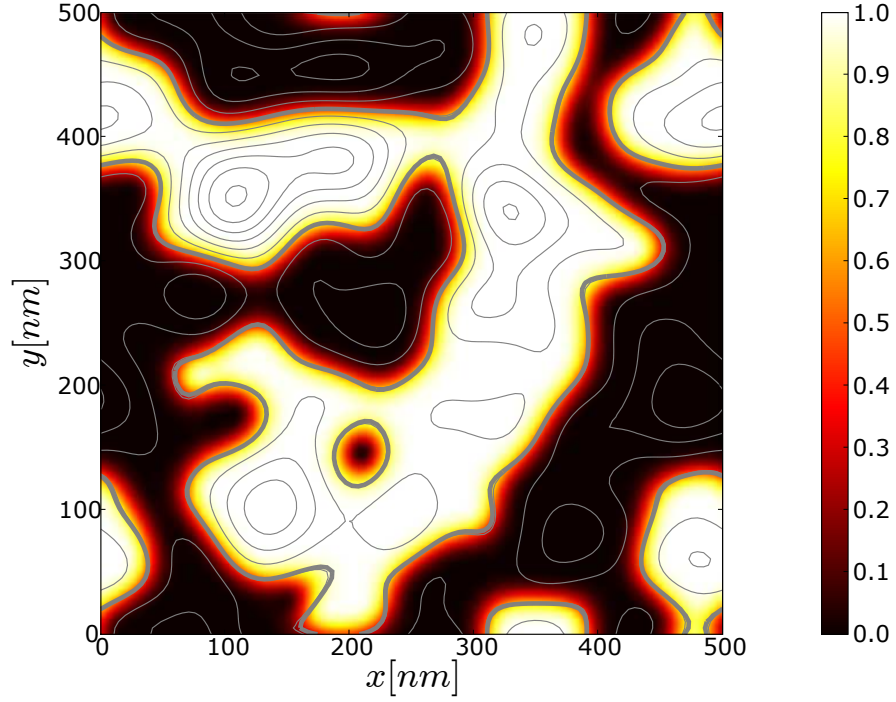


Figure 6.8: Spatial distribution of non-interacting electron density  $n(\mathbf{r})/n_0$  at  $B = 4\text{T}$ ,  $\gamma = 0$  and  $\nu = 1/2$  as indicated by the color scale. Solid contour lines show the equipotential lines of the  $V_I(\mathbf{r})$ . The thick solid lines corresponds to  $\epsilon_F$ .

is readily calculated in our system. It details the screening mechanism by providing direct insight into the interplay of disorder and interaction. Let us start at the QH transition. Figure 6.8 depicts the critical charge density at  $\nu = 1/2$  for a non-interacting system in units of  $n_0$ . The contour lines show the impurity potential  $V_I(\mathbf{r})$  where the critical energy  $V_I(\mathbf{r}) = \epsilon_F$  is highlighted by a thick line. The charge density evidently behaves according to the semiclassical approximation [34] and follows the equipotential lines of  $V_I(\mathbf{r})$ . For the interacting case, however, we expect Thomas-Fermi screening theory to apply [71, 124–126]. This approximation is appropriate for an impurity potential smooth on the scale of the magnetic length as well as a sufficient separation of the Landau bands, characterised by the condition  $\hbar\omega_c/l_c > \sqrt{\langle |\nabla V_I(\mathbf{r})|^2 \rangle}$ . The electrostatic potential of

the charge density

$$\phi(\mathbf{r}) = \frac{e}{4\pi\epsilon\epsilon_0} \int d^2\mathbf{r}' \frac{n(\mathbf{r}') - \bar{n}}{|\mathbf{r}' - \mathbf{r}|} \quad (6.9)$$

and the impurity potential  $V_I(\mathbf{r})$  form a screened potential  $V_{\text{scr}}(\mathbf{r}) = V_I(\mathbf{r}) + e\phi(\mathbf{r})$ . Here,  $\bar{n}$  accounts for the positive background. Since a flat screened potential is energetically most favourable, one expects to find  $V_{\text{scr}}(\mathbf{r}) = \epsilon_F$  for the case of perfect screening. However, since fluctuations of the density,  $\delta n(\mathbf{r}) = n(\mathbf{r}) - \bar{n}$ , are restricted between an empty and a full Landau level, i.e.  $0 < \delta n(\mathbf{r}) < n_0$ , the screening is not always perfect but depends on the fluctuations in the impurity potential as well as on the filling factor [71, 124, 125]. The plane can be divided into fully electron or hole depleted, insulating regions — where  $n(\mathbf{r}) = 0$  or  $n(\mathbf{r}) = n_0$ , respectively — and metallic regions — where  $n(\mathbf{r})$  lies in between. Depending on the filling factor, the extent of those regions varies. Close to the band edge, insulating regions dominate (cf. Figures 6.9 and 6.10). Screening is highly non-linear and transport virtually impossible. On the other hand, if disorder is weak enough, there exists a finite range of filling factors in the centres of each band where metallic regions cover most of the sample, percolate and render the whole system metallic. The disorder is effectively screened and transport greatly enhanced. In that case, the charge density  $n_{\text{scr}}(\mathbf{r})$  can be obtained by Fourier transforming the screened potential. In 3D, this simply leads to the Laplace equation. For 2D, however, one obtains [127]

$$n_{\text{scr}}(\mathbf{q}) = -\frac{2\epsilon\epsilon_0}{e^2} |\mathbf{q}| V_I(\mathbf{q}) + \nu n_0 \delta_{\mathbf{q},0}, \quad (6.10)$$

where the  $|\mathbf{q}| = 0$  term is "perfectly screened" by the positive background and thus does not contribute to screening of the impurity potential. In other words, in our system only the fluctuations  $\delta n(\mathbf{r})$  are essential for screening. Hence, in 2D, a perfectly screening charge density would obey

$$n_{\text{scr}}(\mathbf{r}) = -\frac{4\pi\epsilon\epsilon_0}{e^2} \int d^2\mathbf{r}' \frac{\Delta_{2D} V_I(\mathbf{r}')}{|\mathbf{r} - \mathbf{r}'|} + \nu n_0. \quad (6.11)$$

Clearly, the actual charge density is expected to deviate from  $n_{\text{scr}}(\mathbf{r})$  for several reasons. Firstly, the fluctuations of  $n(\mathbf{r})$  are restricted as discussed above. Secondly, (6.11) is

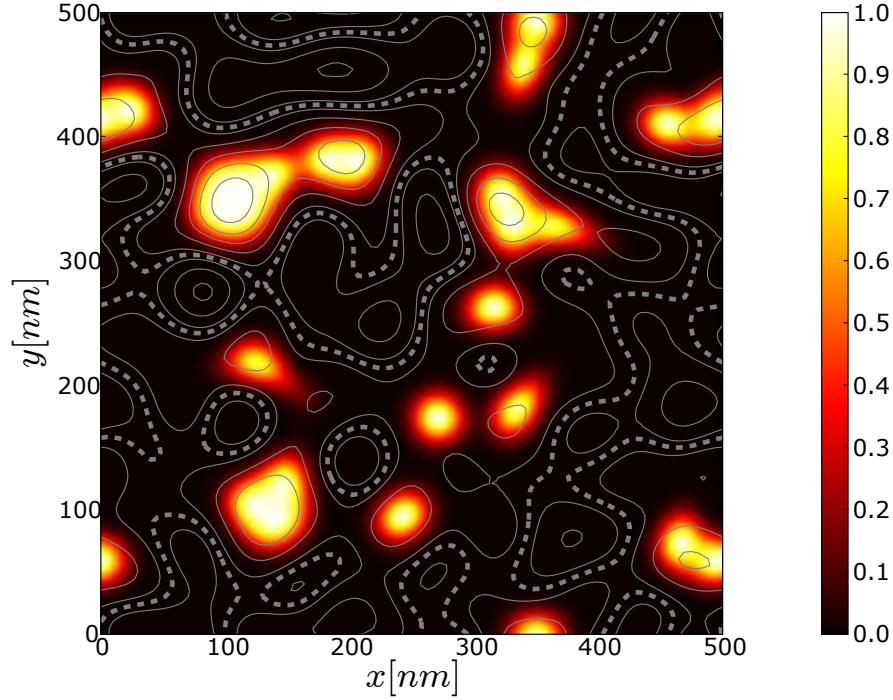


Figure 6.9: Spatial distribution of HF-interacting electron density  $n(\mathbf{r})/n_0$  at  $B = 4\text{T}$ ,  $\gamma = 0.3$  and  $\nu = 0.1$  as indicated by a color scale. Solid contour lines show the equipotential lines of (6.11). The broken lines indicate unscreenable (insulating) regions.

valid for the Hartree case only. For comparison, in Figure 6.11 we have depicted the charge density of a *Hartree*-calculation. The density displays purely classical behaviour and fits the contour lines, Equation (6.11), perfectly. Taking the Fock contribution into account will introduce short wavelength fluctuations due to the tendency for crystallisation. However, we still expect the charge density to follow (6.11) in the limit of  $|\mathbf{q}| \rightarrow 0$ . Figure 6.12 shows results for the charge density of interacting electrons at  $\nu = 1/2$ . Broken lines indicate the regions where  $n_{\text{scr}}(\mathbf{r})$  exceeds the range for  $\delta n(\mathbf{r})$  either below or above, i.e. areas that cannot be screened at all and thus exhibit insulating behaviour. Otherwise, we find the charge density to follow  $n_{\text{scr}}(\mathbf{r})$  very closely. In this regime, the density is well described by (6.11) and the screening is very effective. Metallic regions dominate over insulating ones and transport is expected to be good.

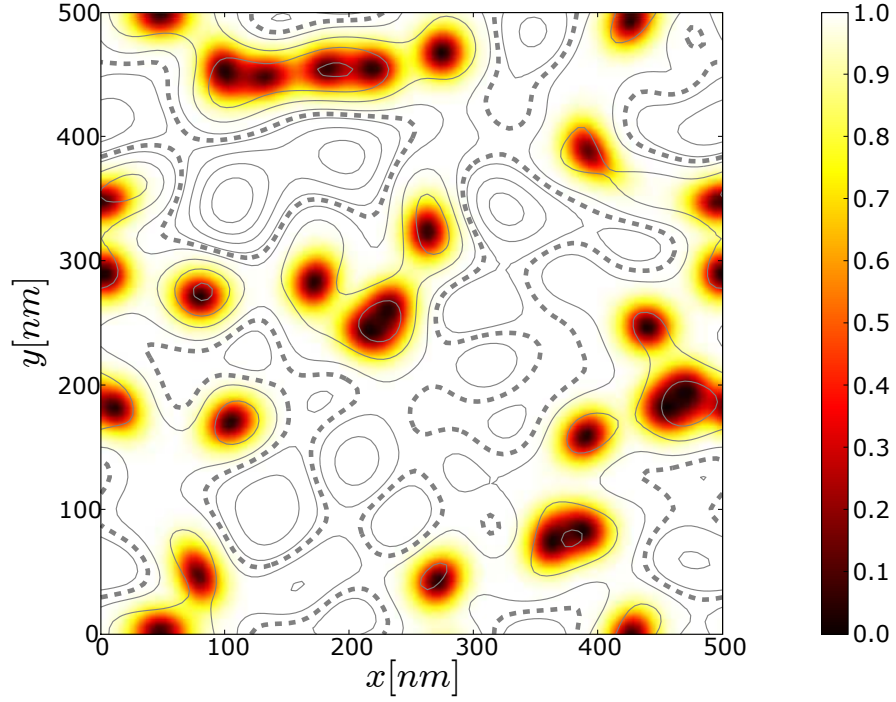


Figure 6.10: Spatial distribution of HF-interacting electron density  $n(\mathbf{r})/n_0$  at  $B = 4\text{T}$ ,  $\gamma = 0.3$  and  $\nu = 0.9$  as indicated by a color scale. Solid contour lines show the equipotential lines of (6.11). The broken lines indicate unscreenable (insulating) regions.

In contrast, if the filling factor is close to an integer value, the charge density cannot provide sufficient fluctuations in order to screen effectively. We have depicted this situation for  $\nu = 0.1$  in Figure 6.9 and for  $\nu = 0.9$  in Figure 6.10. In Figure 6.13 we depict cross-sectional plots of  $n(\mathbf{r})$  and  $n_{\text{scr}}(\mathbf{r})$  for the sample of Figure 6.12 at  $x = 100\text{nm}$  and three different filling factors, demonstrating the discussed effects again very clearly.

## 6.5 Breakdown of Linear Screening

Thus far we have shown that our results can qualitatively reproduce the structures observed in the  $(B, n_e)$  plots of the compressibility. We find stripes of constant width

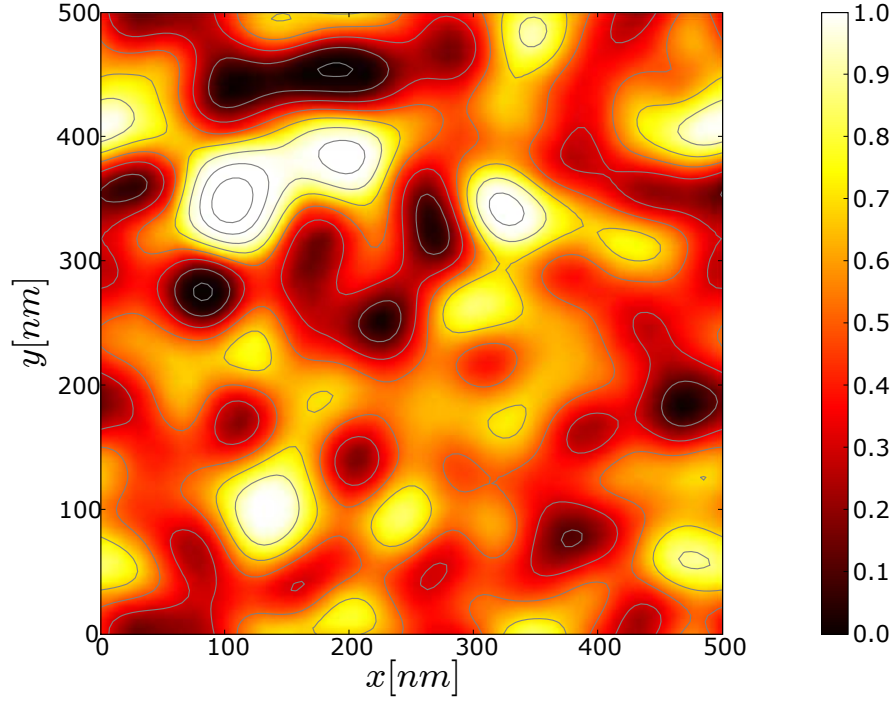


Figure 6.11: Spatial distribution of Hartree-interacting electron density  $n(\mathbf{r})/n_0$  at  $B = 4\text{T}$ ,  $\gamma = 0.3$  and  $\nu = 1/2$  as indicated by the color scale. Contour lines show (6.11). Evidently, the charge density behaves completely classical and provides perfect screening for the impurity potential.

with very similar characteristics as in the experiments. Furthermore, we show that within HF, the impurity potential in the band centre can be quite effectively screened by the charge density. Let us now turn our attention to the stripes. The screening of the impurity potential is non-linear near the edges of the Landau bands. Most of the sample is thus covered by insulating regions where the Landau band is either completely depleted or completely filled. We will now derive an estimation for the cross-over to the linear screening regime, which can be found by very general considerations [67]. An insulating island where  $n(\mathbf{r}) = n_0$  is confined by the force of the impurity potential,  $\nabla V_I(\mathbf{r})$ , around its edge. Thereby, the Coulomb interactions opposing this force making the edge of the full region metallic. The size of the edges, i.e. the size of the metallic

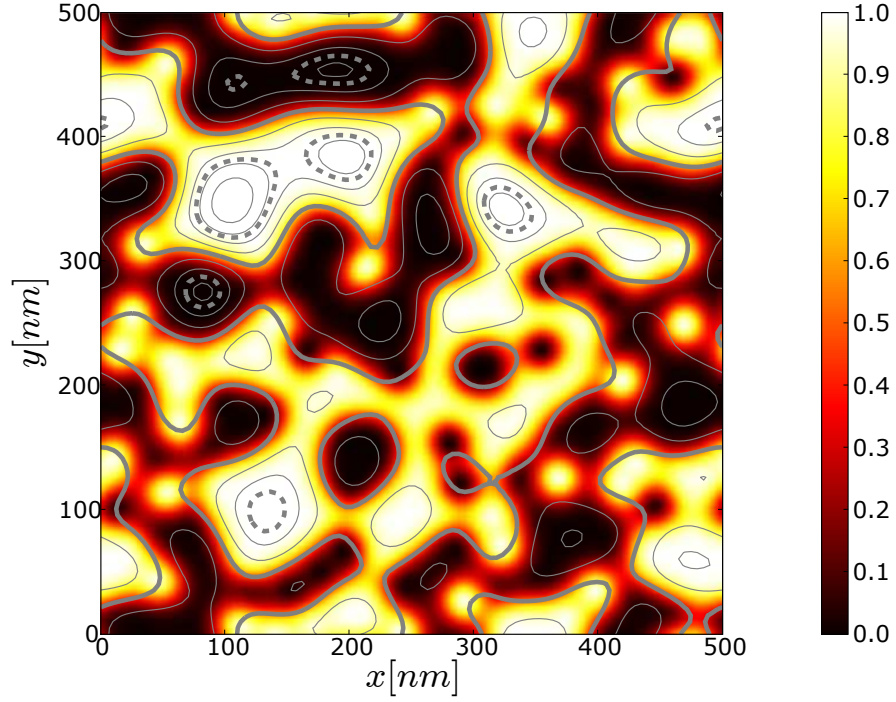


Figure 6.12: Spatial distribution of HF-interacting electron density  $n(\mathbf{r})/n_0$  at  $B = 4\text{T}$ ,  $\gamma = 0.3$  and  $\nu = 1/2$  as indicated by the color scale. Contour lines show (6.11). The broken lines indicate unscreenable (insulating) regions. The thick solid line shows  $n_{\text{scr}}(\mathbf{r}) = \bar{n}_{\text{scr}} = 0$ .

region, is then determined by the Coulomb force  $n_0 e^2 / (2\pi\epsilon\epsilon_0)$ . Only if the Coulomb force acquires a magnitude comparable to the typical confining potential force, the metallic edges of the full islands will connect and dominate over the insulating regions. The typical force of our impurity potential is given by  $\langle |\nabla V_I(\mathbf{r})|^2 \rangle = n_I \langle w_s^2 \rangle_s / (\pi d^4)$ . We would like to remark that with  $N_I = 288$ , the expected standard deviation of  $\langle w_s^2 \rangle_s$  is  $\sim 2\%$ , which makes the typical force a reliable characteristic of  $V_I$  for finite sample calculations. From equating the typical force with the Coulomb force we can derive an expression for the minimal required density  $n_0$  which corresponds to a minimum magnetic field  $B_{\text{min}} = n_0 h / e$  below which linear screening breaks down for any density.



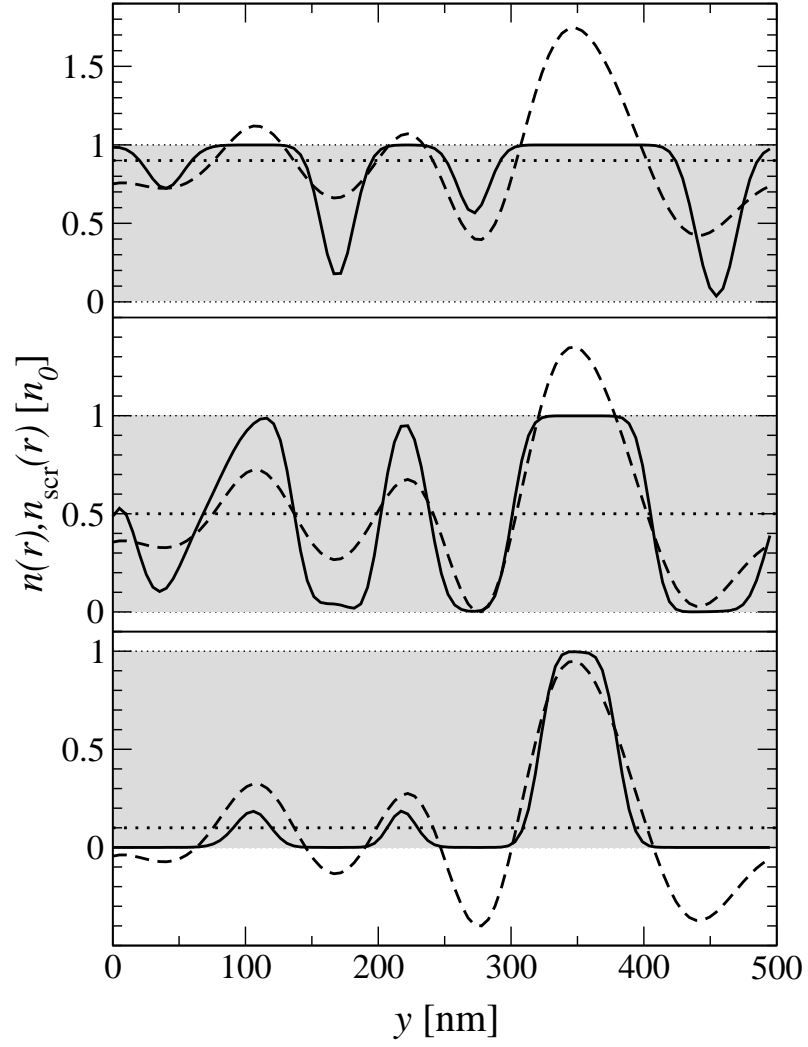


Figure 6.13: Cross-sections of the system of Figure 6.12 at  $x = 100\text{nm}$  and filling factors  $\nu = 0.1$ ,  $\nu = 0.5$ , and  $\nu = 0.9$  (bottom to top). Full curves correspond to  $n(\mathbf{r})$ , broken lines show (6.11). A thick horizontal dotted line shows the average charge density,  $\nu n_0$ . The grey areas, bounded by thin dotted lines, indicate the complete band.



Therefore,  $n_0$  determines the width of the charging stripes  $\Delta n$  and we find

$$\Delta n = n_0 = \frac{2\pi\epsilon\epsilon_0}{\gamma e^2} \sqrt{\langle |\nabla V_I(\mathbf{r})|^2 \rangle} = \frac{2\pi\epsilon\epsilon_0}{\gamma e^2} \sqrt{\frac{n_I}{3\pi}} \frac{W}{d^2}. \quad (6.12)$$

Note that  $\Delta n$  is indeed independent of  $B$  and  $n_e$  as observed in the experiments. In Figures 6.5, 6.6, and 6.7, we have indicated the breakdown of the linear screening regime by dashed white lines. The points at which the lines merge indicate  $B_{\min}$ . Evidently, (6.12) nicely estimates the widths of the observed stripes for all three disorder configurations used. Furthermore, we have tested the criterion for breakdown by plotting compressibilities as a function of  $n_e$  and disorder strength  $W/d^2$ . Figure 6.14 shows the result for  $W/d^2$  between 1meV and 3meV at  $B = 3.5$ T. The dashed white lines again

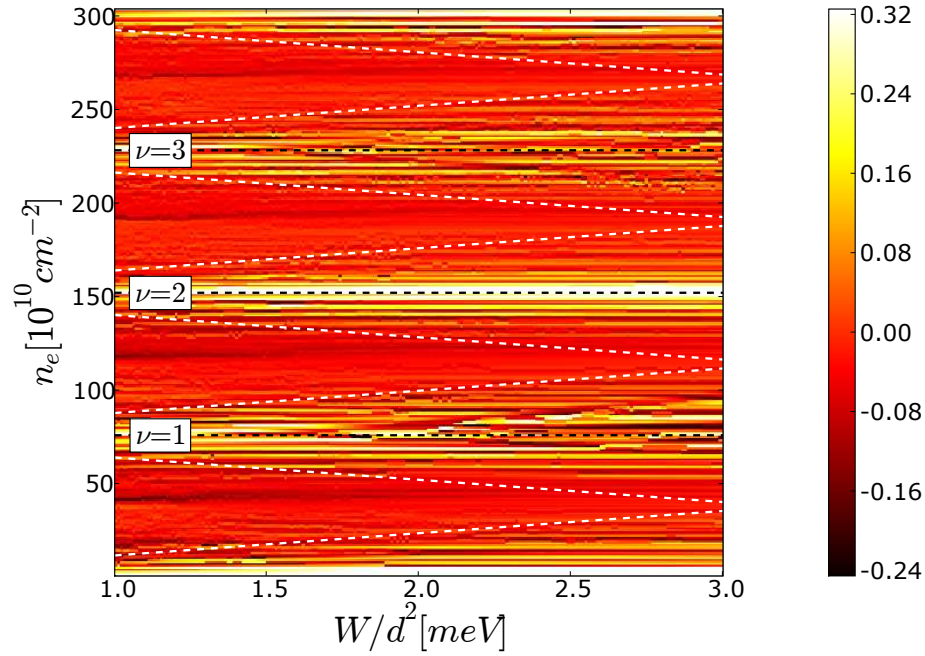


Figure 6.14: Inverse electronic compressibility  $\kappa^{-1}$  for a HF-interacting system ( $\gamma = 0.3$ ) of size  $L = 300$ nm in the  $(W/d^2, n_e)$ -plane. Dashed white lines indicate expected boundaries of linear screening as calculated from (6.12), dashed black lines show integer filling factors.

indicate (6.12). In order to confirm the dependence of the stripes on the ratio between  $W$  and  $d^2$  only, the plot has been divided into two regimes. Between 1meV and 2meV, we kept  $d = 40\text{nm}$  as a constant and varied  $W$ , and between 2meV and 3meV we kept  $W/\text{nm}^2 = 3.2\text{meV}$  constant whilst varying  $d$ , accordingly. The results confirm (6.12). Deviations from the expected behaviour can be explained with the proximity to the disorder dominated regime for higher values of  $W/d^2$  where  $B \simeq B_{\min}$ . This regime is strongly disorder dominated and charging effects become much less pronounced at the band edges.

Eventually, we would like to mention a similar numerical study on compressible edge channels in split-gate quantum wires [128]. Although edges are absent in our model, extrema in the impurity potential lead to an edge-like situation in the vicinity. Therefore, we can relate the width of the compressible edge channels to the width of our linear screening regime. The authors find an increase in the width of the compressible channels upon increasing the magnetic field. This is in good agreement with our findings (cf. Figures 6.5, 6.6, and 6.7). We do, however, also find good agreement with (6.12), which has been derived in Hartree approximation. We ascribe this discrepancy to the rather different systems under study. An investigation of the explicit effect of the exchange interaction in our model could be worthwhile.

## 6.6 Compressibility Patterns in the FQHE

Similar compressibility patterns have also been observed around fractional filling factors  $\nu = 1/3, 2/5$ , and  $2/3$  [18]. Energy gaps at fractional filling, e.g.  $\nu = p/(2p + 1)$ , with  $p$  being an integer, are a consequence of electron correlations which are absent in HF approximation. However, with the formal analogy [129] between IQHE and FQHE put forward by the composite fermion (CF) model [130, 131], let us venture a few statements about compressibility patterns around those fractional fillings. It is argued that the FQHE can be regarded as a manifestation of the IQHE for CFs in an effective magnetic field  $B^* = B_\nu - B_{\nu=1/2}$  [132, 133]. If we pretend to have obtained results

for CFs in an  $(B^*, n_{\text{CF}})$  plane, a transformation back to electrons yields an increase in the density of charging lines (per  $n_e$ ) by a factor of  $2p + 1$ . Indeed, in the above mentioned experiment an increase of 3 has been found for  $\nu = 1/3$ . Furthermore, such a transformation predicts a dependence of the width of the incompressible stripes on the filling factor as well as a strong increase of  $B_{\text{min}}$  when fractional filling factors approach  $\nu = 1/2$ . This remains yet to be explored in detail.

## 6.7 Conclusion

We investigated the compressibility patterns observed in recent imaging experiments [17, 18]. Our numerical simulations confirmed the suggestion that these patterns are due to linear and non-linear screening of the impurity potential by the electrons. More precisely, the breakdown of the ability of the 2DEG to screen the impurity potential completely. In the centre of the Landau band, at half integer filling factors, the electron density is free to fluctuate and due to energy minimisation will adapt to the impurity potential. This screening effect can be near to perfect given that the potential of the impurities to be screened lies within an empty and a full Landau band. Due to the energy gap between the Landau bands, the charge density is restricted to lie within this band and cannot screen stronger fluctuations. A certain finite range of filling factors exist in the middle of the Landau bands where near-to-perfect screening can be achieved. At filling factors close to an integer value the restriction of the band edges becomes relevant and the sample will contain incompressible charge density patches of a completely full or empty Landau band, respectively. The charge density becomes torn apart more and more strongly and screening will be highly non-linear. The remaining compressible regions are spatially confined which is reminiscent of quantum dots and holes. Eventually, any new charge entering the sample in this regime will trigger Coulomb blockade effects within the sample, leading to a jump of the chemical potential, and hence the compressibility. The experimentally observed patterns around integer filling factor are fingerprints of precisely those charging effects. As long as the Fermi level lies in the non-linear regime,

the screening is ineffective and the addition of a new electron results in a compressibility jump, independent of the nature or the width of the gap. In fact, the energy width of the first and the second gap in the regime of our calculation differ by about a factor five. Strikingly similar patterns have been found around fractional filling factors in an experiment by [18], indicating the importance of screening as well as charging effects even for quasi-particles.

## Chapter 7

# Conductivity

In the preceding Chapter we have focussed our attention on interaction driven compressibility patterns in the localised regime. The results were successfully compared to imaging experiments. We were able to explain those patterns in terms of linear and non-linear screening and found a formula to discriminate between the two regimes. The derived formula based on a force-balance argument fitted the numerical results very well. One may now want to argue that the numerical support provided by the compressibility results might be limited to the localised regime. Therefore we will now focus on how transport coefficients are affected by the mutual interactions and whether the above arguments also hold in the delocalised regime. The compressibility patterns found in the experiments discussed above were in fact preceded by transport experiments that revealed patterns in the conductance, also apparently interaction mediated [19,20]. Reference [19] reported on Hall conductance measurements on mesoscopic MOSFET devices in the  $(V_g, B)$ -plane, where  $V_g$  is the gate voltage. The results were different to the expectations deduced from a single-particle model [109]. The gate voltage  $V_g$  can be linked to the electron number density as  $n_e = (C/e)V_g$ , where  $C$  is a material specific constant. Similar to the experiments of Ilani et al. [17], a line in the  $(V_g, B)$ -plane can thus be labeled by a certain filling factor,  $\nu$ .

In Figure 7.1 we show the Hall conductance measured by Cobden et al. [19] The

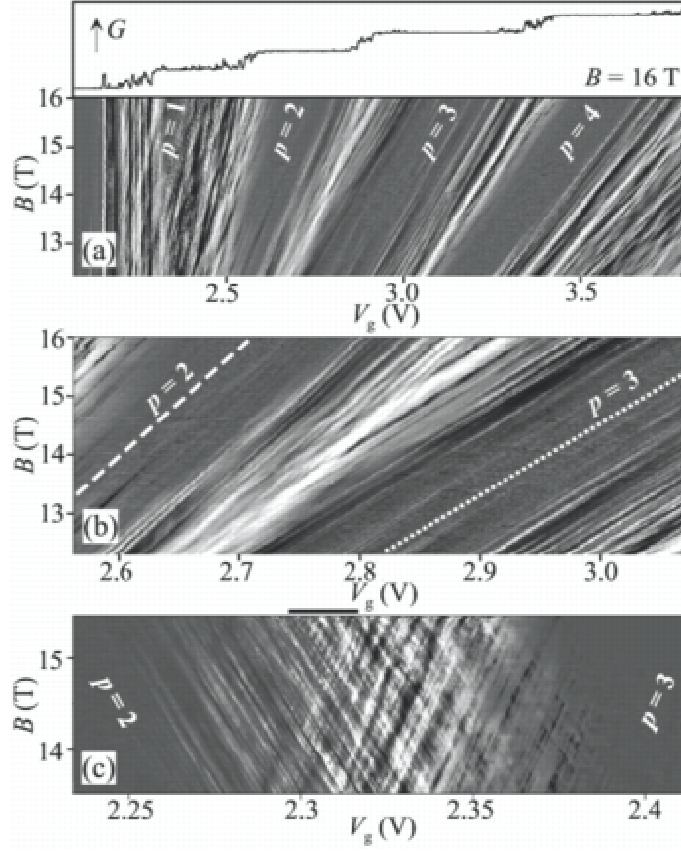


Figure 7.1: Hall conductance in the  $(V_g, B)$ -plane, where the gate voltage  $V_g$  is proportional to  $n_e$ . The plateau values have been subtracted for clarity [19]. Light areas show low conductance. Alignment of conductance minima with integer filling factors can be seen, thereby leading to plateaus with constant width.

fluctuations around the plateau transitions at half integer filling factor are apparently correlated over a large interval of the magnetic field. Surprisingly, however, the lines formed by the conductance extrema in the  $(V_g, B)$ -plane evidently align with *integer filling factors*. In a simplified model, such resonances can be thought of as bound states around potential extrema. The quantisation condition for such bound states requires an integral number of flux quanta to be encircled. Thus, the encircled area is proportional to the magnetic field. When the flux is increased by one flux quantum, the bound state expands accordingly, thereby increasing or decreasing its energy when bound to a

potential minima or maxima, respectively. A change in magnetic field thereby entails a change in energy of a resonance dependent on the specific form of the potential extrema. Thus it is not obvious why peaks in the conductance should align with an integer filling factor in the  $(V_g, B)$ -plane. In fact, considering electron-electron interactions offers a much more convincing explanation. Cobden et al. [19] suggested the following scenario. The charge density in the sample can be divided into compressible and incompressible regions. Wherever the density is free to fluctuate, i.e. where the local filling  $2\pi l_c^2 n_e(\mathbf{r})$  lies well away from an integer value, the 2DES exhibits metallic behaviour. Wherever the density fills a whole LL, i.e.  $2\pi l_c^2 n_e(\mathbf{r})$  is close to an integer, the density is incompressible and thus insulating. In the spatial density profile, the metallic regions form puddles that are enclosed by insulating boundaries where the density corresponds to a full LL. With electron-electron interactions present, transport through the sample is now influenced by tunneling through the metallic puddles that are always surrounded by an insulating, incompressible density strip. The conductance peaks can then be associated with the charging condition of the puddles and therefore with the shape of the puddles. It is reasonable to assume that a particular density profile does not change along lines of constant filling factor in the  $(V_g, B)$ -plane, only the average density as  $n_e = \nu e B / h$ . Thus it is clear that along lines where  $\nu$  is an integer, the shape of the incompressible puddles (contours where  $2\pi l_c^2 n_e(\mathbf{r})$  is an integer) remains roughly constant, therefore its charging condition and hence the conductance extrema.

## 7.1 Linear Response: The Kubo Formula

The Kubo formula is based on a fluctuation-dissipation theorem linking the imaginary part of a response function to an equilibrium expectation value. A small, time-dependent perturbation of the Hamiltonian is assumed and the response only taken to linear order [134]. We will be interested in the conductivity,  $\sigma_{\alpha\beta}$ , which is the response of the current due to an externally applied electric fields. The linear response is the microscopic version

of Ohm's law and reads

$$j_\alpha(\mathbf{r}) = \sum_\beta \sigma_{\alpha\beta} E_\beta^{\text{ext}}(\mathbf{r}) , \quad \text{with } \alpha, \beta \in \{x, y\}. \quad (7.1)$$

This can be integrated over the whole area to yield the total current as  $\mathbf{J} = \int d^2\mathbf{r} \mathbf{j}(\mathbf{r})$ .

The scope of this thesis will be restricted to the static off-diagonal part of the conductivity tensor. For this Hall conductivity one finds the well-know expression [105, 135]

$$\sigma_{xy} = -\frac{ne c}{B} + \frac{2e^2 \hbar}{L^2} \sum_\alpha^{(<\epsilon_F)} \sum_\beta^{(>\epsilon_F)} \text{Im} \frac{\langle \psi_\alpha | \dot{X} | \psi_\beta \rangle \langle \psi_\beta | \dot{Y} | \psi_\alpha \rangle}{(\epsilon_\alpha - \epsilon_\beta)^2} , \quad (7.2)$$

where the first term on the right hand side is the classical contribution from the cyclotron motion and the second can be regarded as the quantum mechanical correction. A detailed derivation of the above Kubo formula is lengthy [134] and will not be revised in this work. We rather turn to the problem of numerically evaluating the Hall conductivity for an HF-interacting system.

## 7.2 Periodic Boundary Conditions, Berry Phase, and Conductivity

For a single-particle system, an expression for the guiding centre velocity required to compute the above Kubo formula is easily found and given in Appendix D. However, in a HF-interacting system, where a non-local exchange term is involved, the procedure is much less trivial. In fact, the evaluation of the non-local exchange-velocity is usually limited to a perturbative treatment in the short or long-wavelength limit of the electromagnetic field [136], both of which do not apply for a spatially varying vector potential. We can, however, make headway by noting that the two terms on the right hand side of Equation (7.2) are just the result of splitting up the spatial coordinates  $x$  and  $y$  into cyclotron and guiding centre coordinates. Rewinding this step in the derivation of the Kubo formula, we can write

$$\langle \psi_\alpha | \dot{\hat{x}} | \psi_\beta \rangle = \frac{i}{\hbar} \langle \psi_\alpha | \mathcal{H} \hat{x} - \hat{x} \mathcal{H} | \psi_\beta \rangle = (\epsilon_\alpha - \epsilon_\beta) \frac{i}{\hbar} \langle \psi_\alpha | \hat{x} | \psi_\beta \rangle , \quad (7.3)$$



instead of the velocity matrix elements, and we find the following expression for the conductivity

$$\sigma_{xy} = \frac{2e^2}{\hbar L^2} \sum_{\alpha} \sum_{\beta} f_{\alpha}(1 - f_{\beta}) \text{Im} \langle \psi_{\alpha} | \hat{x} | \psi_{\beta} \rangle \langle \psi_{\beta} | \hat{y} | \psi_{\alpha} \rangle . \quad (7.4)$$

At first sight, this expression seems to avoid the complicated non-local commutators and should therefore be easier to handle. This is indeed true for a non-periodic system. However, one realises rather quickly that the PBC, which are essential in order to obtain useful results from finite-sized numerical simulations, will cause serious problems. The reason is that a non-periodic position operator is ill-defined in the Hilbert space of periodic wave functions, and we therefore have

$$\langle \psi_{\alpha} | \hat{\mathbf{r}} | \psi_{\beta} \rangle \neq \langle \psi_{\alpha} | \mathbf{r} | \psi_{\beta} \rangle . \quad (7.5)$$

This is easily rationalised by considering the position expectation of a localised state at the cell boundary. By virtue of the PBC, the state is replicated onto the other side of the cell and a naive evaluation of the expectation value will yield anything but the true centre of mass of the localised state. The solution to this problem is the definition of a periodic position operator [137–141]. An expectation value could then be defined as [138, 140]

$$\langle \psi_{\alpha} | \hat{x} | \psi_{\alpha} \rangle = \frac{L}{2\pi} \text{Im} \log \langle \psi_{\alpha} | \exp \left( i \frac{2\pi}{L} x \right) | \psi_{\alpha} \rangle , \quad (7.6)$$

which is an admissible expression because  $\psi_{\alpha}^*(\mathbf{r})\psi_{\alpha}(\mathbf{r})$  is a real valued. For any off-diagonal matrix element, however, such an expression fails and instead we have to define the position operator as

$$\langle \psi_{\alpha} | \hat{\mathbf{r}} | \psi_{\beta} \rangle = -i \langle \psi_{\alpha} | e^{-i\mathbf{k}\mathbf{r}} \nabla_{\mathbf{k}} e^{i\mathbf{k}\mathbf{r}} | \psi_{\beta} \rangle \Big|_{\mathbf{k}=0} = -i \langle \psi_{\alpha}^{\mathbf{k}} | \nabla_{\mathbf{k}} | \psi_{\beta}^{\mathbf{k}} \rangle \Big|_{\mathbf{k}=0} \quad (7.7)$$

where we introduce an additional phase-factor,  $\mathbf{k} = (k_x, k_y)^T$ , into the wave functions as

$$| \psi_{\beta}^{\mathbf{k}} \rangle = e^{i\mathbf{k}\mathbf{r}} | \psi_{\beta} \rangle . \quad (7.8)$$

These wave functions are not eigenstates of the original Hamiltonian, but of a parametrised Hamiltonian,  $\mathcal{H}^{\mathbf{k}}|\psi_{\beta}^{\mathbf{k}}\rangle = \epsilon^{\mathbf{k}}|\psi_{\beta}^{\mathbf{k}}\rangle$ , which in our case reads

$$\mathcal{H}^{\mathbf{k}} = \frac{1}{2m^*} (\mathbf{p} - e\mathbf{A} + \hbar\mathbf{k})^2 + V. \quad (7.9)$$

Since we are working in terms of basis functions that are eigenfunctions of the clean, kinetic part of this Hamiltonian, we derive the new  $\mathbf{k}$ -dependent basis functions,  $\varphi_{n,k}(\mathbf{k}, \mathbf{r})$ , for which we find

$$\langle \mathbf{r} | \varphi_{n,k}(\mathbf{k}) \rangle = e^{-ik_y y - ik_x (x - kl_c^2)} \varphi_{n,k+k_y}(\mathbf{r}) = \quad (7.10)$$

$$\frac{1}{\sqrt{2^n n!} \sqrt{\pi} l_c L} \exp \left[ ik_x (x - kl_c^2) + ik_y y - \frac{(x - (k + k_y)l_c^2)^2}{2l_c^2} \right] H_n \left[ \frac{x - (k + k_y)l_c^2}{l_c} \right]. \quad (7.11)$$

In the previous Chapters we have formulated most of the expressions in terms of plane-wave matrix elements,  $S_{n,k;n',k'}(\mathbf{q})$ , instead of working with the basis function directly. Thus, by changing the plane-wave matrix elements to their general,  $\mathbf{k}$ -dependent form, we can reuse the hitherto derived expressions and have readily access to  $\mathbf{k}$ -dependent wave functions and thus the matrix elements of the PBC-compatible position operator. After some algebra we find for the new general plane-wave matrix elements

$$S_{n,k;n',k'}(\mathbf{q}, \mathbf{k}) = \langle \varphi_{n,k}(\mathbf{k}) | \exp(i\mathbf{q} \cdot \mathbf{r}) | \varphi_{n',k'}(\mathbf{k}) \rangle = \exp[il_c^2(\mathbf{q} \times \mathbf{k})_z] S_{n,k;n',k'}(\mathbf{q}). \quad (7.12)$$

With this minor change we are now able to compute position expectation values and thus the Kubo formula for the conductivity. One little drawback, however, is that the matrix elements of the gradient with respect to  $\mathbf{k}$  must be evaluated numerically. The reason is that both the basis states and the expansion coefficients depend on the additional parameter, and the coefficients can only be obtained through diagonalisation of the Hamiltonian. The derivative of the basis states, however, can be carried out analytically

and we find for the matrix elements of the position operator

$$-\mathfrak{i}\langle\psi_{\alpha}^{\mathbf{k}}|\nabla_{\mathbf{k}}|\psi_{\beta}^{\mathbf{k}}\rangle\Big|_{\mathbf{k}=0} \quad (7.13)$$

$$= -\mathfrak{i}\sum_{a,b,n,m}C_{n,a}^{\alpha*}(\mathbf{k})\langle\varphi_{n,a}(\mathbf{k})|\nabla_{\mathbf{k}}C_{m,b}^{\beta}(\mathbf{k})|\varphi_{m,b}(\mathbf{k})\rangle\Big|_{\mathbf{k}=0} \quad (7.14)$$

$$= -\mathfrak{i}\sum_{a,b,n,m}C_{n,a}^{\alpha*}\langle\varphi_{n,a}|\varphi_{m,b}\rangle\nabla_{\mathbf{k}}C_{m,b}^{\beta}(\mathbf{k})\Big|_{\mathbf{k}=0} \quad (7.15)$$

$$- \mathfrak{i}\sum_{a,b,n,m}C_{n,a}^{\alpha*}C_{m,b}^{\beta}\langle\varphi_{n,a}|\nabla_{\mathbf{k}}|\varphi_{m,b}(\mathbf{k})\rangle\Big|_{\mathbf{k}=0} \quad (7.16)$$

$$= -\mathfrak{i}\sum_{a,n}C_{n,a}^{\alpha*}\nabla_{\mathbf{k}}C_{n,a}^{\beta}(\mathbf{k})\Big|_{\mathbf{k}=0} \quad (7.17)$$

$$- \mathfrak{i}\sum_{a,b,n,m}C_{n,a}^{\alpha*}C_{m,b}^{\beta}\left(\langle\varphi_{n,a}|x-k_b l_c^2|\varphi_{m,b}\rangle - \mathfrak{i}\langle\varphi_{n,a}|x-k_b l_c^2|\varphi_{m,b}\rangle - l_c\sqrt{2m}\langle\varphi_{n,a}|\varphi_{m-1,b}\rangle\right) \quad (7.18)$$

The second term can be further simplified using the relations Equation (E.2) from the Appendix and we find

$$\langle\varphi_{n,a}|(x-k_b l_c^2)|\varphi_{m,b}\rangle = l_c\sqrt{\frac{m}{2}}\delta_{n,m-1}\delta_{a,b} + l_c\sqrt{\frac{m+1}{2}}\delta_{n,m+1}\delta_{a,b} \quad (7.19)$$

and for the position operator

$$\begin{aligned} & -\mathfrak{i}\langle\psi_{\alpha}^{\mathbf{k}}|\nabla_{\mathbf{k}}|\psi_{\beta}^{\mathbf{k}}\rangle\Big|_{\mathbf{k}=0} \\ &= -\mathfrak{i}\sum_{a,n}C_{n,a}^{\alpha*}\nabla_{\mathbf{k}}C_{n,a}^{\beta}(\mathbf{k})\Big|_{\mathbf{k}=0} \\ &+ \mathfrak{i}l_c\sum_{a,b,n,m}C_{n,a}^{\alpha*}C_{m,b}^{\beta}\left(\mathfrak{i}\left[\sqrt{\frac{m}{2}}\delta_{n,m-1} + \sqrt{\frac{m+1}{2}}\delta_{n,m+1}\right] - \sqrt{\frac{m}{2}}\delta_{n,m-1} - \sqrt{\frac{m+1}{2}}\delta_{n,m+1}\right)\delta_{a,b}. \end{aligned} \quad (7.20)$$

The derivative in the first term on the right hand side of Equation (7.20) will be evaluated numerically by a simple two-point formula. Especially in a self-consistent HF calculation, the result will be very sensitive to the choice of the step-width for the numerical derivative. Choosing too small a step size will introduce errors due to the machine precision, whereas too big a choice might cause the self-consistent scheme to converge into different ground states. For our simulations we used a step-width of  $10^{-8}$  in magnetic units. We have to point out that by numerically evaluating Equation (7.20),

an arbitrary phase occurs in the expansion coefficients due to the numerical diagonalisation [142]. When multiplying coefficients, this phase normally cancels given it is equal for both coefficients. However, this phase may differ when numerically diagonalising the Hamiltonian for different  $\mathbf{k}$  values. Evaluating the matrix element at several discrete values of  $\mathbf{k}$ , this arbitrary phase can be eliminated [142], thereby yielding a fully gauge invariant result. Unfortunately, such a procedure increases the computational cost by at least an order of magnitude for each direction of  $\mathbf{k}$ . However, when comparing results using Equation (7.20) with results obtained from the guiding centre velocity formula of Equation (D.23), we do not observe any deviation between the two approaches in terms of  $\sigma_{xy}$ . Therefore we conclude that this phase does not influence our results greatly.

Thus, we have found a way of avoiding the evaluation of the non-local exchange velocity as well as the ill-defined position operator. In fact, the additional parameter which can be interpreted as an abstract vector potential in parameter space is a very useful concept that for instance has opened up the link between the quantum Hall effect and topology [12, 13, 143]. Namely, the surface integral over what is known as the Berry connection (or single-point Berry phase),  $\chi(\mathbf{k}) = i\langle\psi^{\mathbf{k}}|\nabla_{\mathbf{k}}|\psi^{\mathbf{k}}\rangle$ , yields the so-called Berry phase [141, 144, 145], an observable that cannot be expressed as an expectation value of any Hermitian operator. Such a geometric phase is observed in a multitude of physical systems [146–151]. In the IQHE, in particular, the Berry phase can be interpreted as a topological quantum number, namely the first Chern class, that assumes integer values only [34, 152]. In this abstract topological interpretation, the quantisation of the IQHE in multiples of  $e^2/h$  has a well-defined mathematical foundation.

## 7.3 Numerical Results

In this Section we present our numerical results obtained by the method detailed above. We note that for the single-particle case the results of the above approach are in perfect agreement with results obtained by the 'standard' guiding centre velocity formula of

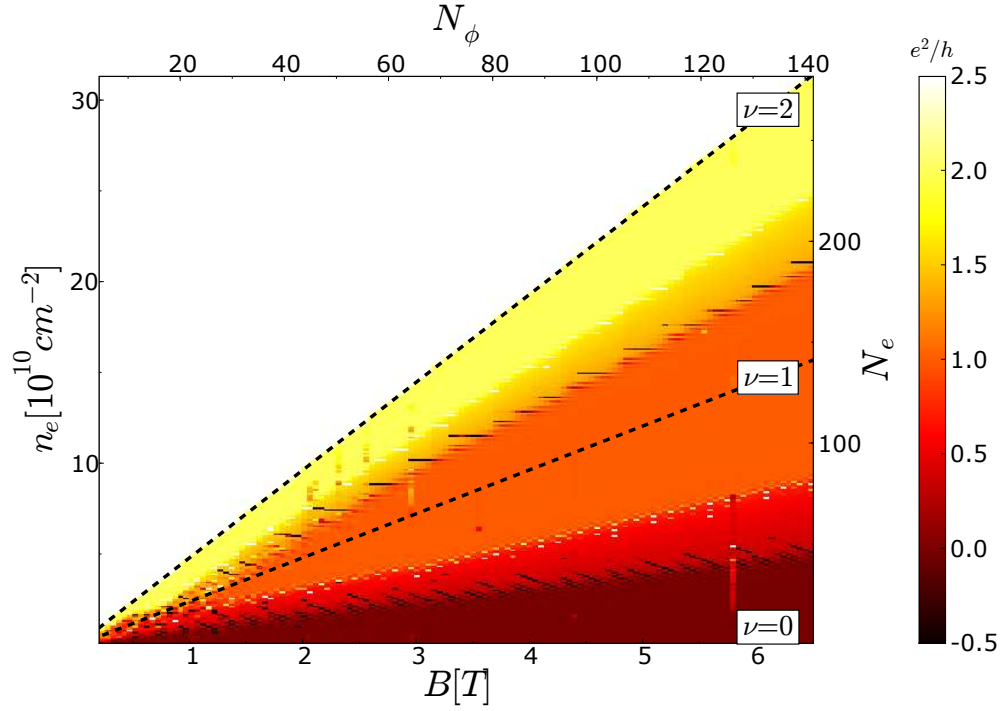


Figure 7.2: Hall conductivity,  $\sigma_{xy}$ , for a *spinless* non-interacting system of size  $L = 300\text{nm}$  with disorder strength  $W/d^2 = 2.5\text{meV}$  in the  $(B, n_e)$ -plane. The two lowest orbital Landau levels are included and integer filling factors are indicated by black broken lines. Due to the neglect of spin, the plateaus appear at 0, 1, and  $2 e^2/h$ .

Equation (D.23), i.e. yielding the same  $\sigma_{xy}$ . We have calculated the Hall conductance in the  $(B, n_e)$ -plane for different parameters.

Figure 7.2 shows the lowest two orbital Landau levels for a system of non-interacting, spinless electrons of size  $L = 300\text{nm}$ . The disorder strength is chosen as  $W/d^2 = 2.5\text{meV}$  with an impurity range of  $d = 40\text{nm}$ . We have indicated the integer filling factors by black broken lines. The first three plateaus with  $\sigma_{xy} = 0, 1$ , and  $2 e^2/h$  are clearly visible. The widths of the plateaus as well as the plateau-to-plateau transitions are proportional to the applied magnetic field  $B$ . Having a  $B$ -independent DOS, this implies a constant width of the plateau and transition regions in energy, which is expected from a single-particle calculation since they are determined by the particular

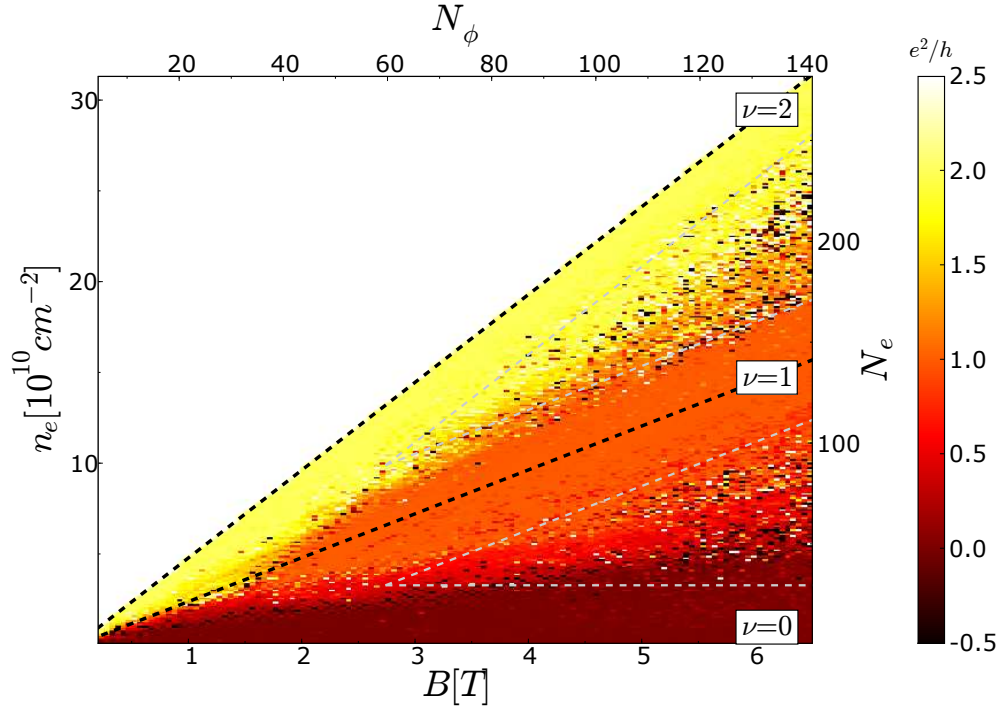


Figure 7.3: Hall conductivity,  $\sigma_{xy}$ , for the lowest two *spin levels* of a HF-interacting system of size  $L = 300\text{nm}$  with disorder strength  $W/d^2 = 2.5\text{meV}$  in the  $(B, n_e)$ -plane. The two spin levels are well separated by virtue of the exchange enhancement of the spin splitting. Integer filling factors are indicated by the black broken lines, whereas the grey broken lines indicate boundaries between linear and non-linear screening as obtained from Equation (6.12).

disorder configuration.

In Figure 7.3 we have depicted the lowest two spin levels of a system of HF-interacting electrons for the same disorder configuration as in Figure 7.2. The spin levels are well separated by the exchange enhanced spin splitting. We observe stable plateaus around integer filling factors, which are indicated by the black broken lines. Figure 7.4 shows the first orbital transition (no spin) of the same system but for a different disorder configuration. In Figure 7.5 we depict the spin-transition of Figure 7.3 with a lower disorder strength of  $W/d^2 = 1.25\text{meV}$ . And Figure 7.6 shows the orbital transition (no spin) of Figure 7.5 for a different disorder configuration. In each figure

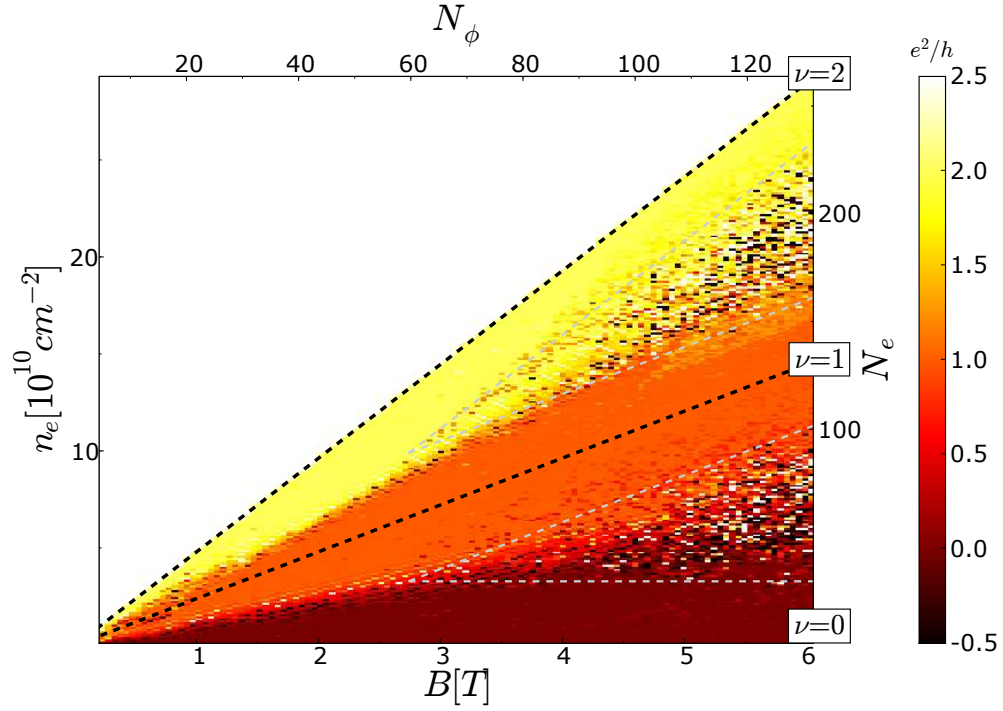


Figure 7.4: Hall conductivity  $\sigma_{xy}$  for the lowest two Landau levels of a *spinless* HF-interacting system of size  $L = 300\text{nm}$  with disorder strength  $W/d^2 = 2.5\text{meV}$  in the  $(B, n_e)$ -plane. The two lowest orbital Landau levels are included and integer filling factors are indicated by the grey broken lines. The black broken lines indicate the boundary between linear and non-linear screening as obtained from Equation (6.12). Due to the neglect of spin, the plateau values are 0, 1, and  $2e^2/h$ , respectively.

we have indicated the integer filling factors by black, and the boundary between the non-linear and the linear screening regime by grey broken lines. From our simulations we can conclude to observe the same behaviour for the spin and the orbital transition, both having similar wide, stable plateaus at the integer filling factors. In contrast to the single-particle calculation, having electron-electron interactions present the widths of the plateaus remain constant when  $B$  is varied. Similarly to the compressibility calculations, the estimation of the cross-over between the non-linear and linear screening appears to describe the competition between disorder and interactions well. The constant width of the plateau is in agreement with the experimental findings of Reference [19] and

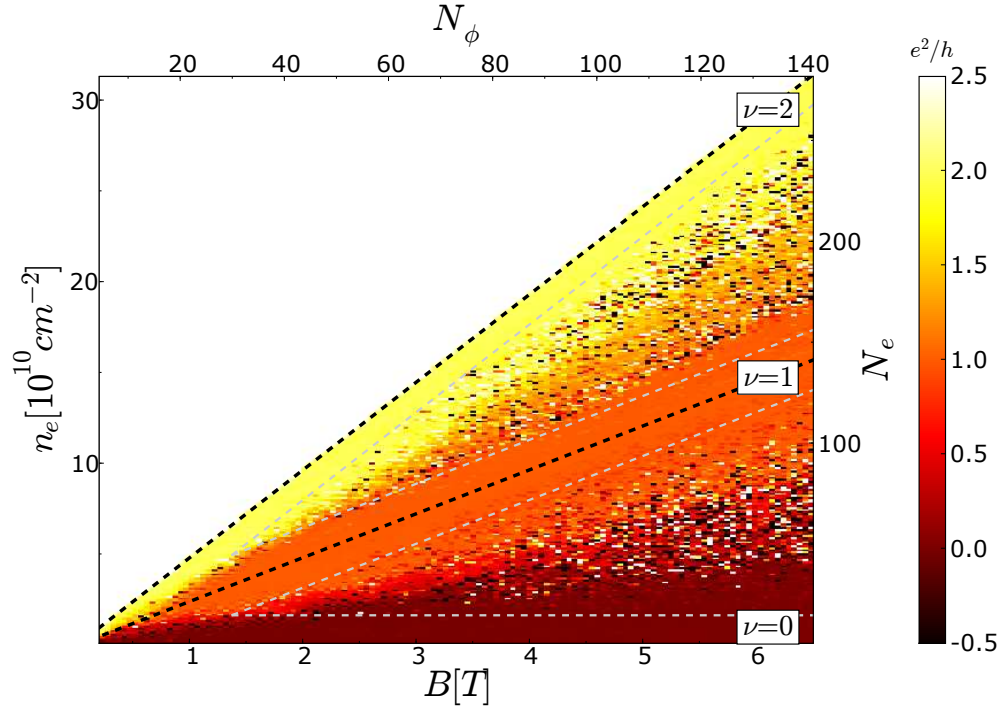


Figure 7.5: Hall conductivity,  $\sigma_{xy}$ , as in Figure 7.3 but with disorder strength  $W/d^2 = 1.25\text{meV}$  and for a different disorder configuration. The black broken lines are again obtained from Equation (6.12).

Reference [17]. The expected alignment of conductance peaks along integer filling factor are, however, absent in our calculations. Instead, we observe rather random conductance jumps in the centre of the bands. We attribute this behaviour to the strong exchange correlation in this regime, which was also predominant in the previous chapter, where the compressibility became strongly negative in the centre of the bands. Therefore we conclude that exchange induced effects dominate over charging and Coulomb blockade effects. The experimentally observed features might be related to an effect beyond numerical tractability. Finally, in Figure 7.7 we show cross-sectional cuts of the previous figures. The left column shows cuts at  $B = 4\text{T}$ , the right column shows  $B = 6\text{T}$ . Figures 7.7(a) and (b) correspond to Figure 7.2, Figures 7.7(c) and (d) to Figure 7.3, Figures 7.7(e) and (f) to Figure 7.4, Figures 7.7(g) and (h) to Figure 7.5, and Figures



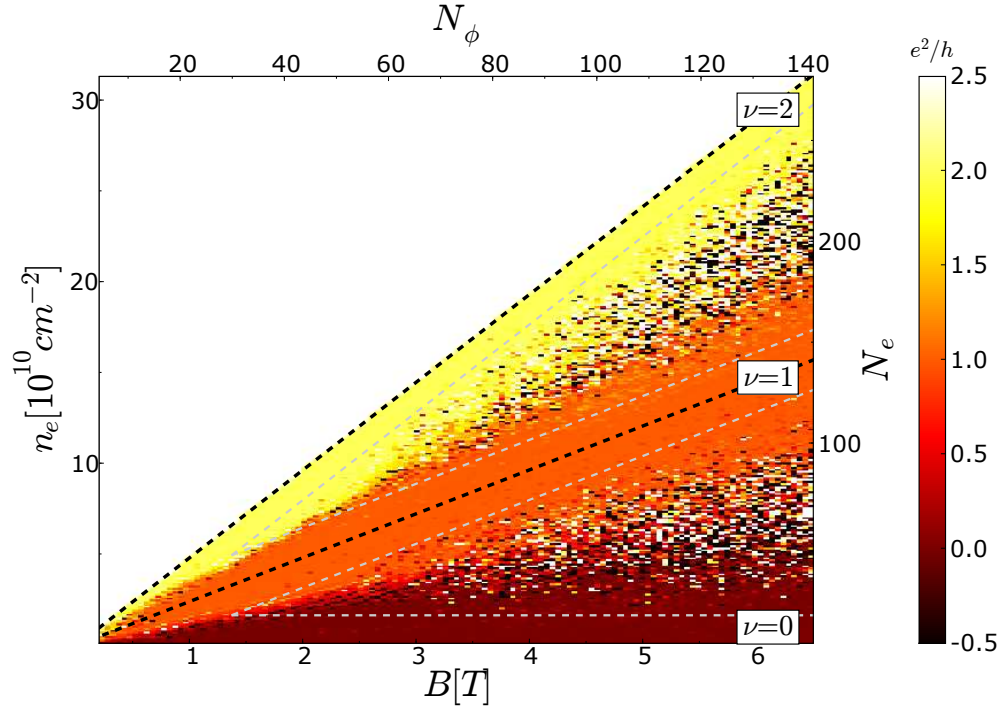


Figure 7.6: Hall conductivity,  $\sigma_{xy}$ , as in Figure 7.4 but with disorder strength  $W/d^2 = 1.25\text{meV}$  and for a different disorder configuration.. The black broken lines are again obtained from Equation (6.12).

7.7(i) and (k) to Figure 7.6. Again, we have indicated the boundaries between linear and non-linear screening by vertical grey broken lines. The plateau regions of localised electrons align well with the estimation formula Equation (6.12) and, to the accuracy of this simulation, their width is indeed independent of the magnetic field. The delocalised regime of the plateau-to-plateau transitions on the other hand increases strongly. This is in contrast to the single particle result, where both the plateau and the transition region increases with the magnetic field. Whereas the compressibility stripes are fingerprints of the non-linear screening, i.e. the insulating regime, the increasing width of the plateau transition demonstrates interaction promoted delocalisation. We regard this behaviour as another important manifestation of the competing interplay between disorder and electron-electron interactions even in the integer quantum Hall effect.

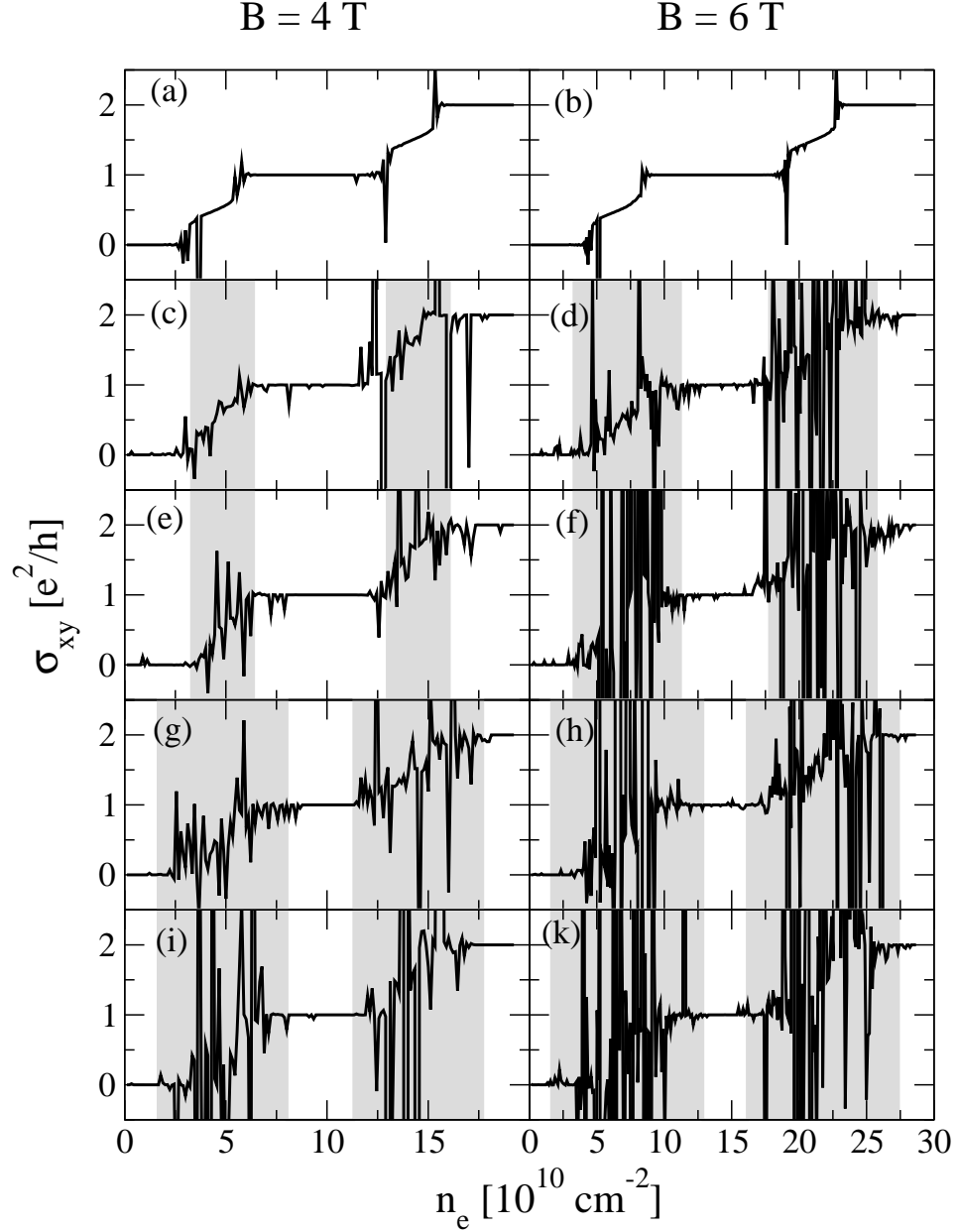


Figure 7.7: Hall conductivity,  $\sigma_{xy}$ , as a function of  $n_e$  for  $B = 4\text{T}$  (left column) and  $B = 6\text{T}$  (right column). Figures (a),(b) show the orbital transition without interactions and spin (cf. Figure 7.2), Figures (c),(d) show lowest spin transition with interactions (cf. Figure 7.3), Figures (e),(f) show lowest orbital transition with interactions (cf. Figure 7.4), Figures (g),(h) same as (c),(d) for weaker disorder (cf. Figure 7.5), and Figures (i),(k) same as (e),(f) for weaker disorder (cf. Figure 7.6). Broken grey lines indicate boundary between non-linear and linear screening regime. For further details see text.

## Chapter 8

# Interaction Effects in STS Measurements

### 8.1 Probing a 2DEG

Scanning tunneling spectroscopy (STS) measurements constitute a tool for directly imaging electrons in a 2D plane [153, 154]. In contrast to compressibility measurements information obtained from STS imaging can be linked to the charge density and thereby provide a way of visualising them spatially [107]. The sample surface which contains the 2DEG is approached by a very narrow tip consisting of a few atoms only. When a potential,  $U$ , is applied between tip and sample and their distance becomes as low as a few Å, the wave functions overlap and a tunneling current flows. Following the standard model of Tersoff and Hamann [107, 155], which calculated the current from a rate equation, it can be seen that at  $T = 0$  the current is related to the LDOS in the following way (given  $U > 0$ )

$$I(U, \mathbf{r}, z) \propto \int_0^{eU} \text{LDOS}'_{\text{sample}}(E_{\text{sample}} + E, \mathbf{r}, z) \cdot \text{LDOS}_{\text{tip}}(E_{\text{tip}} - eU + E) dE , \quad (8.1)$$

where the energies  $E_{\text{sample}}$  and  $E_{\text{tip}}$  are the Fermi energies in the sample and in the tip, respectively, and  $U$  is the potential drop between the sample and the tip. The LDOS in the integrant is, however, not the true sample LDOS, but also depends on the distance and work functions of tip and sample. How these influences are eliminated from the data are experimental details which will be omitted here. The integral is eliminated simply by measuring the differential conductivity,  $dI/dU$ , which is, up to some corrections, directly proportional to the LDOS. Since the LDOS of the tip will not change whilst moving across the sample, the LDOS of the sample can eventually be extracted. The LDOS is thereby defined as the charge density at a particular energy, as given in Equation (5.6). The measurement is, however, subject to a finite energy resolution. The energy window can be modeled as a semi-ellipse around the Fermi energy [108], thus the measured local density of states,  $\text{LDOS}_{\Delta E}$ , is calculated as

$$\text{LDOS}_{\Delta E}(E, \mathbf{r}) = \int dE' \text{LDOS}(E', \mathbf{r}) \cos \left[ \arcsin \left( \frac{E - E'}{\Delta E} \right) \right], \quad (8.2)$$

where  $\Delta E$  is governed by temperature and a AC modulation voltage of the order of 1mV, leading to an energy window of  $\Delta E \simeq 2.5\text{meV}$ . The AC modulation voltage is the main contributor to the broadening of the window, but necessary in order to suppress unwanted noise which would render the STS image unusable [108]. Therefore one has to compromise between energy resolution and noise. For completeness it should be mentioned that another feature of the STS experiment is the exponential dependence of the current on the distance,  $d$ , from the surface, i.e.  $I \propto \exp(-d)$ , making the current very sensitive to the distance and therefore allows for a spatial resolution to a few picometer. The experiments which will be referred to in this work, and which serve as a comparison for our numerical simulations, are measurements on the surface of cleaved n-type InSb (110) crystals [156, 157]. Thereby, the sample energy,  $E_{\text{sample}}$ , is held constant at 0meV, whereas  $E_{\text{tip}}$  is varied by the voltage drop between tip and sample. A change in  $E_{\text{sample}}$  will only take place locally due to the QD potential of the STS tip. Further away from the tip  $E_{\text{sample}}$  remains a constant. Since  $E_{\text{tip}}$  is typically below 0meV, electrons are ejected from the filled states of the sample into

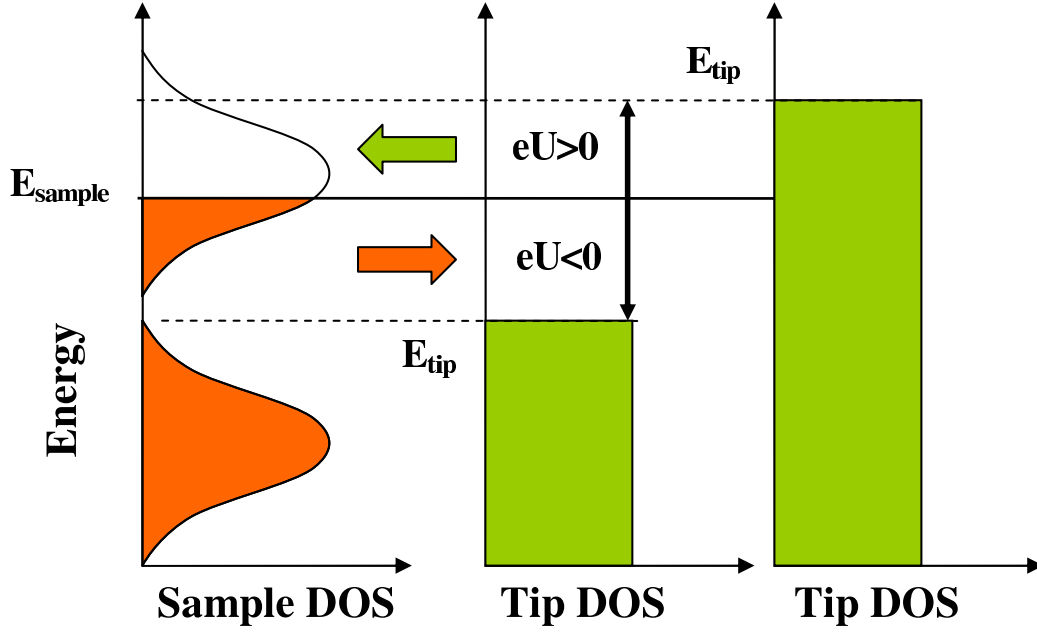


Figure 8.1: The energy scheme of an STS measurement. Left: DOS and filled states in the sample, the Fermi energy is fixed. Middle: DOS and filled states in the tip with negative bias ( $eU < 0$ ). Electrons tunnel from the tip to the sample, indicated by the arrow. Right: DOS and Fermi energy of a tip with positive bias. Electrons tunnel from the sample into the tip.

empty states in the tip, as indicated in Figure 8.1. We also indicated the situation when  $E_{\text{tip}} > E_{\text{sample}}$ , where electrons are injected from the tip into the sample. If the two Fermi levels coincide, i.e. if states around the Fermi level of the sample are probed, interaction effects may become relevant, since the DOS at the Fermi level is significantly altered (see Section 5.1). In the following, we will derive an expression for the potential experienced by the 2DEG and investigate the effect of the tip potential as well as mutual interactions between the electrons in the sample.

## 8.2 The Donor Potential

We model the InSb structure as a 3D distribution of donor atoms with a 2DEG sitting on top at the cleaved surface at  $z = 0$ . We take the  $z$ -direction pointing downwards. The

donor density in the 3D region of the experimentally used sample is  $n_{3D} = 1.7 \cdot 10^{16} / \text{cm}^3$  [157]. The electrostatic potential at  $\mathbf{R} = (\mathbf{r}, z)$  of a single donor atom sitting at  $\mathbf{R}_0 = (\mathbf{r}_0, z_0)$  below the 2DEG ( $z_0 \geq 0$ ) has the screened form [158]

$$V_{3D}(\mathbf{r}, z) = -\frac{V_0}{\sqrt{(\mathbf{r} - \mathbf{r}_0)^2 + (z - z_0)^2}} \exp \left[ -q_{3D} \sqrt{(\mathbf{r} - \mathbf{r}_0)^2 + (z - z_0)^2} \right] , \quad (8.3)$$

with the parameters  $V_0 = e^2 / (4\pi\epsilon_{\text{InSb}}\epsilon_0) = 81 \text{nm} \cdot \text{meV}$  where we have used  $\epsilon_{\text{InSb}} = 17.7$ , and  $q_{3D} = (24 \text{nm})^{-1}$  [104], being the appropriate screening length for the relevant 3D density. We take the finite thickness of the 2DEG into account by assuming the  $z$ -part of the wave function as

$$n_e(z) = \frac{q_z^3}{2} z \exp(-q_z z) , \quad (8.4)$$

where  $q_z = (4.5 \text{nm})^{-1}$  [159, 160]. The effective potential experienced by the 2DEG at  $z = 0$  can eventually be determined by the convolution [31, 160]

$$V_{2D}(\mathbf{r}) = \int_0^\infty dz n_e(z) V_{3D}(\mathbf{r}, z) . \quad (8.5)$$

## Fourier Transform

For the numerical implementation we are interested in the Fourier transform of the effective donor potential,  $\tilde{v}_{2D}(\mathbf{q}) = L^{-2} \int d^2\mathbf{r} \exp(-i\mathbf{q}\mathbf{r}) V_{2D}(\mathbf{r})$ . Therefore we place the donor atom at  $\mathbf{R}_0 = (\mathbf{0}, z_0)$  and we compute the 2D Fourier transform of Equation (8.3) first, yielding

$$\tilde{V}_{2D}(q, z) = -\frac{2\pi V_0}{L^2 \sqrt{q^2 + q_{3D}^2}} \exp \left( -|z - z_0| \sqrt{q^2 + q_{3D}^2} \right) . \quad (8.6)$$

The Fourier transform of the effective potential can now be computed straightforwardly from

$$\tilde{v}_{2D}(q) = \int_0^\infty dz n_e(z) \tilde{V}_{2D}(q, z) , \quad (8.7)$$

which gives

$$\tilde{v}_{2D}(q) = -\frac{\pi V_0 q_z^3 e^{-z_0 q_z}}{L^2 \sqrt{q^2 + q_{3D}^2}} \left[ \frac{(1 + z_0 q_+)^2 + 1}{q_+^3} - \frac{(1 + z_0 q_-)^2 + 1 - 2e^{z_0 q_-}}{q_-^3} \right] , \quad (8.8)$$

where we have used the abbreviation

$$q_{\pm} = q_z \pm \sqrt{q^2 + q_{3D}^2} \quad . \quad (8.9)$$

The second term on the right hand side of Equation (8.8) even though being mathematically well defined, suffers from numerical instability whenever  $q_- \rightarrow 0$ . Therefore we expand this term to fourth order and use

$$\tilde{v}_{2D}(q) = -\frac{\pi V_0 q_z^3 e^{-z_0 q_z}}{L^2 \sqrt{q^2 + q_{3D}^2}} \left[ \frac{(1 + z_0 q_+)^2 + 1}{q_+^3} + \frac{z_0^3}{3} \left( 1 + \frac{z_0 q_-}{4} \right) \right] , \quad (8.10)$$

whenever  $|z_0 q_-| < \epsilon$  instead of Equation (8.8). The value of  $\epsilon$  depends on the machine precision but appears to be reasonable as  $\epsilon = 10^{-3}$ . We finally like to add that after a careful study of the n-type crystal used in the experimental LDOS measurements, our experimental collaborators found a certain amount of acceptors and thus we decided to do the calculations with both donors and acceptors, and chose the densities as  $n_D = 9 \cdot 10^{21} \text{m}^{-3}$  and  $n_A = 5 \cdot 10^{21} \text{m}^{-3}$ . In Figure 8.2 we have depicted the effective potential of a distribution of impurities in an area of size 350nm. The dark spots are donor impurities, whereas the white spots are acceptors.

### 8.3 The Tip Potential

The tip will be modeled as an additional potential acting in the plane of the 2DEG. The tip shape and strength are very hard to estimate [156]. Therefore we will assume a Gaussian shape and a width of 25nm. The strength will be varied in the range  $V_{\text{tip}} = -20 \text{meV}$  to  $V_{\text{tip}} = 20 \text{meV}$  which can be regarded as worst case scenarios [156]. We emphasise that its effect on imaging data is hitherto unclear. The numerical effort increases considerably by introducing the tip potential since for each spatial position of the tip the (self-consistent) eigenvalue problem has to be solved independently.

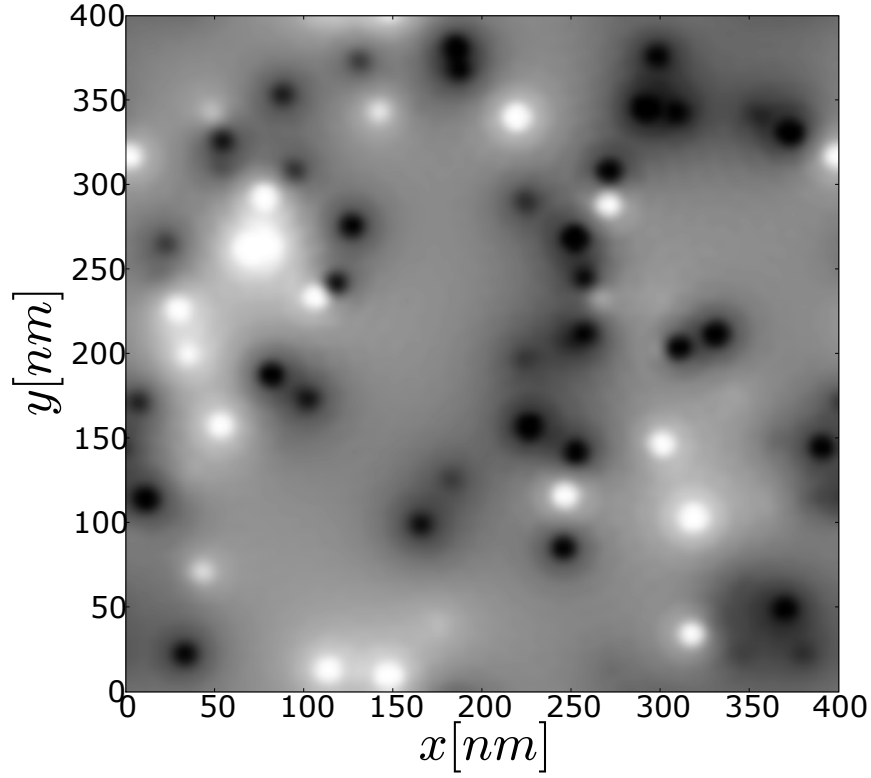


Figure 8.2: Effective impurity potential at  $z = 0\text{nm}$  for a distribution of donors and acceptors situated  $50\text{nm} < z < 0\text{nm}$  below the 2DEG. Dark spots are donor impurities, white spots show acceptors.

## 8.4 Numerical Results

The following results are calculated using an effective  $g$ -factor as  $g^* = 28$ , effective mass as  $m^* = 0.02$ , and a dielectric constant  $\epsilon = 17.7$  [104]. The  $g$ -factor obtained from the experimental data was slightly lowered from its bulk value, most likely due to stress and confinement effects [161], and has been adjusted accordingly in the calculation. Moreover, the experimentally determined minimum of the conduction band of  $E_{\text{CBM}} = -100\text{meV}$  [162] due to the surface potential has been subtracted. The energy window, i.e. the energy resolution is chosen as  $\Delta E = 2.5\text{meV}$ . In Figure 8.3 we show a comparison between a measured and a calculated LDOS for a non-interacting



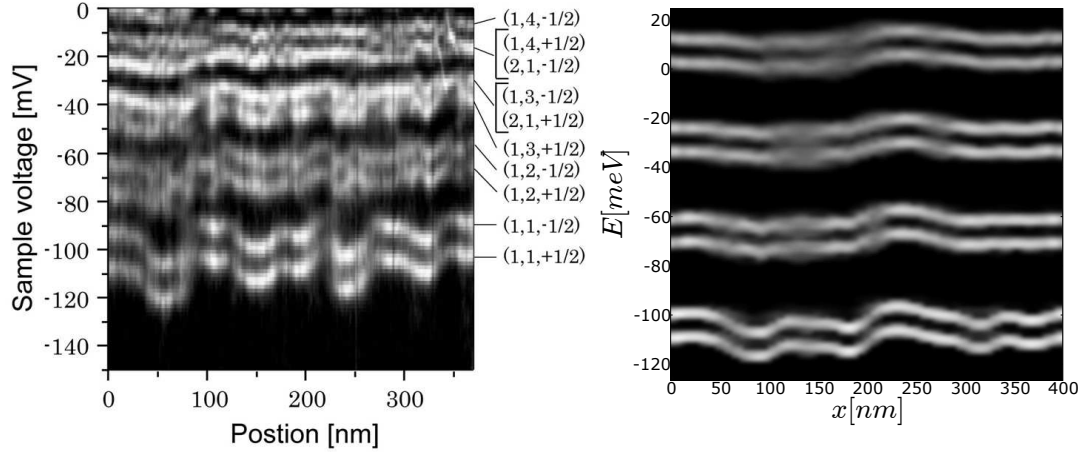


Figure 8.3: Comparison between the measured (left) and calculated (right) LDOS for the lowest four spin-split LL. The tip strength is chosen as  $V_{\text{TIP}} = -20\text{meV}$ .

system at  $B = 6\text{T}$  with  $V_{\text{tip}} = -20\text{meV}$ . The left figure shows the measurement, the right is the corresponding non-interacting calculation. Lighter areas correspond to a high LDOS, whereas darker areas correspond to a low LDOS. The visible features thus correspond to different Landau levels which vary as a function of position due to the locally varying disorder potential. The position as well as the fluctuations of the LDOS is in good agreement with the experimental data, supporting the adequacy of our numerical model. Slight deviations in the positions of the Landau levels can be attributed to the non-parabolicity of the conduction band, leading to an energy dependence of the effective mass [157, 161], which is not accounted for in our calculations. Even though the impurity density in the calculation has been chosen carefully, it is not completely clear as to why the experimental LDOS exhibits slightly more features than the simulation. This could be related to an amount of Cs atoms which has been detected on the surface of the sample and those might lead to an increased impurity potential [157]. This is, however, hard to determine experimentally and not particularly relevant for this investigation. Therefore we now turn to the effect of the QD tip potential strength and the electron-electron interactions. The sample Fermi energy in the experiment is held constant at  $E_{\text{sample}} = 0\text{meV}$ , which resides inside the fifth orbital LL when  $B = 6\text{T}$ . In

our simulation, however, we may analyse different fillings as well. Due to our numerical scheme, the filling of the sample has to be determined by the electron density rather than the Fermi energy. Fixing the Fermi energy leads to unphysical jumps in the LDOS. In Figure 8.4 we have plotted the LDOS for a HF-interacting system at different filling factors of the sample and different tip strengths. We show the lowest two spin-split Landau levels which we label from the lowest to the highest with LL1 through LL4. The three columns correspond to  $V_{\text{tip}} = -20, 0, \text{ and } 20 \text{ meV}$ , and the four rows are sample fillings of  $\nu = 0, 0.5, 1.0, \text{ and } 2.5$ , as given in the caption of Figure 8.4.

We will analyse Figure 8.4 from the bottom row to the top row, always starting without a tip potential (middle column), then discuss the effects of applying a negative (left column) and a positive bias (right column) bias, respectively. Starting at  $\nu = 0$ , the Fermi level lies below LL1 and the system does not contain filled states. Thus the LDOS is equivalent to the single-particle case. With a negative bias, the LDOS is shifted down in energy about the amount of the tip potential, whereas a positive bias shifts the LDOS similarly upwards in energy. This is due to a tip induced states residing at the bottom or the top of the tip potential, respectively. The effect of the QD tip can thus be summarised as a rigid energy shift of the LDOS proportional to the tip strength.

In the second row from the bottom we place the Fermi level at  $\nu = 0.5$ , i.e. in the centre of LL1. Without a QD tip present, the LDOS of LL1 fluctuates strongly whereas LL2 through LL4, away from the Fermi level, exhibit less structure than at  $\nu = 0$ . This effect can be identified as the screening mechanism, where electrons close to the Fermi level in LL1 redistribute whilst far away from it an effectively screened potential remains, leading to a narrower LDOS. We note here that the fluctuating LDOS of LL1 seems to split into two bands, developing a gap exactly at the Fermi level which gives rise to the DOS gap as reported on in Section 5.1. If the tip bias is negative, we find strong exchange enhanced spin splitting between the different spin levels, LL1 and LL2. Since the probed states of LL1 are situated below the Fermi level, the LDOS features in LL1 are due to ejected electrons from filled states, which are pushed downwards in energy.

Therefore we observe direct spin splitting enhancement between states of different spin below and above the Fermi level, i.e. of LL1 and LL2. Moreover, we also observe indirect splitting enhancement between LL3 and LL4, the next orbital Landau level. We would like to mention very recent spectroscopy experiments [21] with similar findings in support of our results. For positive tip bias, all the probed states are located above the Fermi level and the observed features can be attributed to injecting electrons into the higher band tails. Those states are empty and basically unaffected by interactions.

Having a completely filled LL1, i.e.  $\nu = 1$ , the spin splitting is predicted to be highest [21,121], which can be seen clearly without a QD tip present. Adding a negative tip bias to the calculation will cause the probed states of the lowest two Landau levels, LL1 and LL2, to also lie below the Fermi surface and distinctly separate in energy from LL3 and LL4. In case of a positive bias, the LDOS again corresponds to injecting electrons into empty states which are unaffected by the exchange splitting. We note that the abrupt jumps of the LDOS visible for  $\nu = 1$  are numerical instabilities due to the HF-convergence scheme.

Finally, at filling factor  $\nu = 2.5$ , where all the states up to the centre of LL3 are filled, we find a similar situation as for  $\nu = 0.5$ , only with the Fermi level in LL3. The spin shifts due to the exchange correlation can be understood accordingly. In view of the recent high-resolution experiments by Dial et al. [21], a more quantitative analysis of the enhancement of spin splitting due to the exchange correlation could be a worthwhile task.

Eventually we present some real-space imaging results of the LDOS. The two top rows of Figure 8.4 show the experimentally obtained LDOS. The top row corresponds to the real-space data in an square area of length  $L = 350\text{nm}$  and the second row shows the respective Fourier transforms. The images are taken in LL1 through LL4. The two bottom rows show the corresponding calculation results without a QD tip, whereby the second row from the bottom are the real-space result and the bottom row the Fourier transforms. We observe ring structures in  $k$ -space with the number of rings equal to

the orbital Landau level. These rings can be linked to the number of peaks in a Landau state, which is equal to the Landau level index. They can be traced back to the effective harmonic confinement due to the magnetic field, as seen in Equation (2.19). In fact, the striking similarity between experiment and simulation can be regarded as the first experimental verification of the spatial structure of higher Landau level wave functions, which even survives the influence of the QD potential.

In summary, we have investigated the influence of a tip potential and electron-electron interactions on spatially resolved measurements of the LDOS by comparison with numerical calculations. We found a minor influence of the QD tip potential, mainly leading to a rigid shift in energy. Regarding the electron-electron interactions, we described the relevance of the position of the Fermi level on the interpretation of the results. In view of the data of our experimental collaborators [157], the influence of electron-electron interactions is negligible since the sample Fermi level is fixed in the fifth orbital level, far away from the more interesting lower levels. Finally, we would like to acknowledge the contributions of Katsushi Hashimoto and Markus Morgenstern, providing the experimental LDOS data.

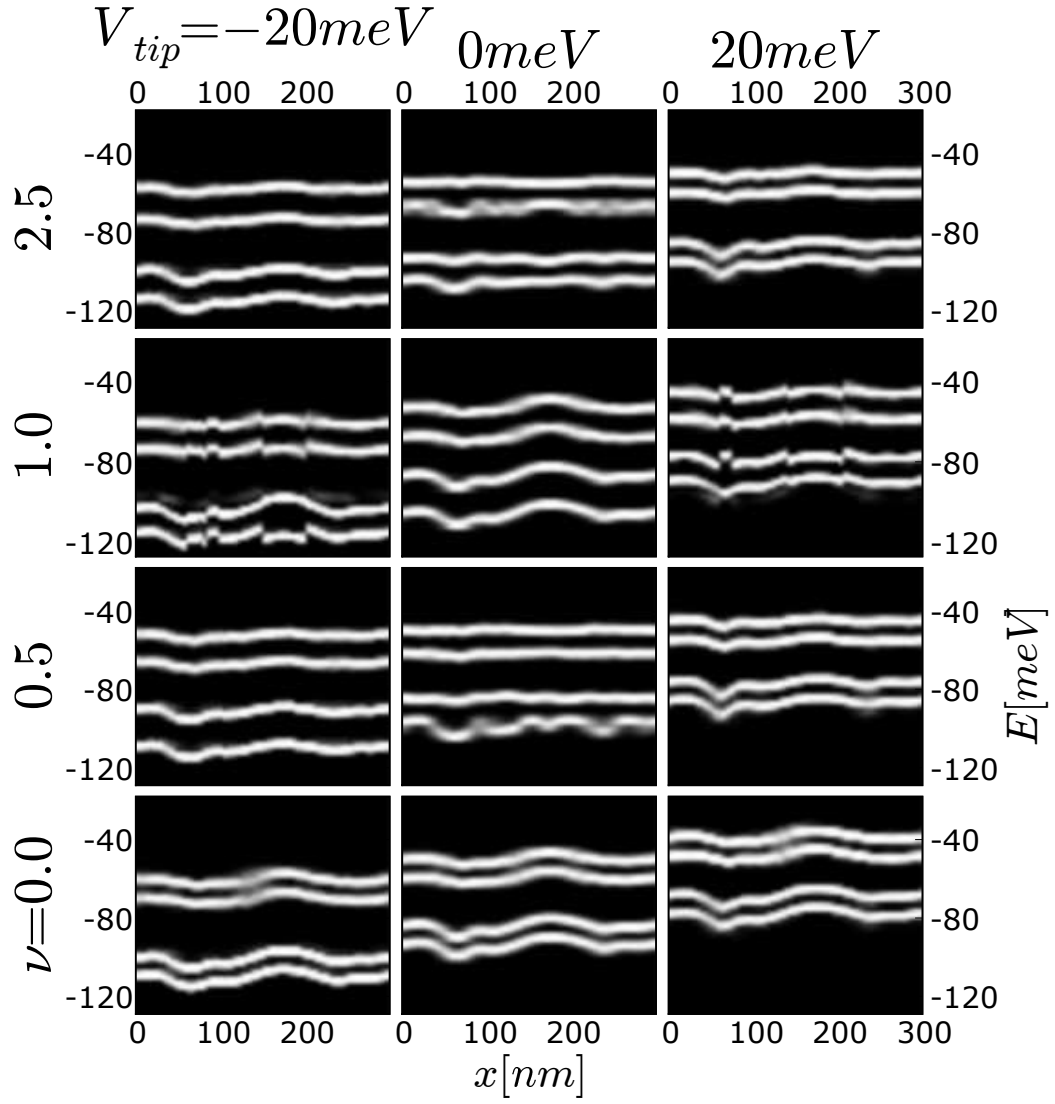


Figure 8.4: Calculated LDOS for the two lowest, spin-split Landau levels. Light areas correspond to high LDOS, whereas dark areas correspond to low LDOS. The QD tip strength is  $V_{\text{tip}} = -20\text{meV}$  in the left column,  $0\text{meV}$  in the middle column, and  $20\text{meV}$  in the right column. The filling factor is  $\nu = 0, 0.5, 1$ , and  $2.5$ , starting from the bottom row.

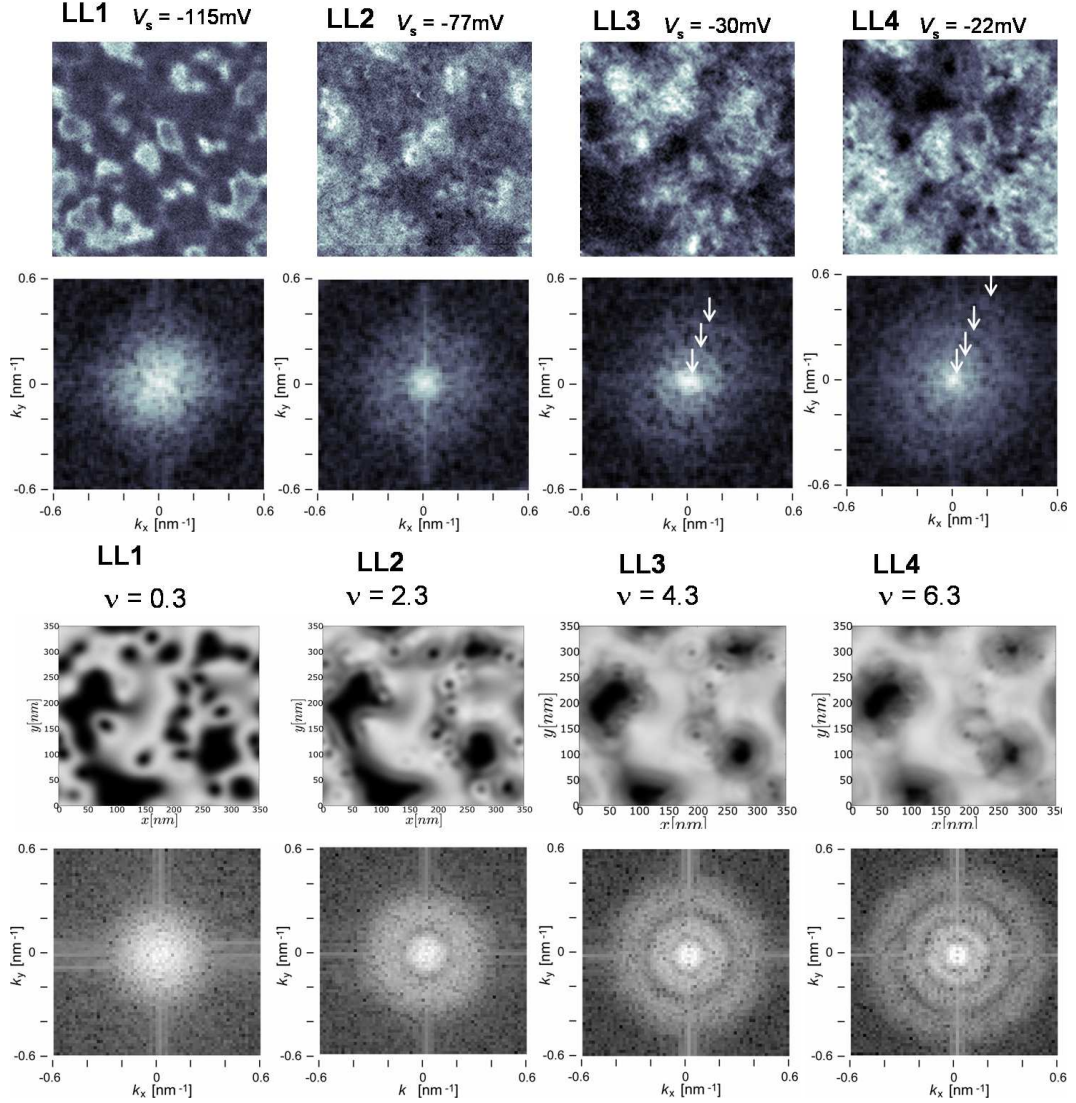


Figure 8.5: Upper two rows: Measured LDOS images (first row) in an area of  $350 \times 350\text{nm}$ , in the lowest four spin down Landau levels and the respective Fourier transforms (second row). Lower two rows: Simulation result of the above LDOS images. The orbital level is indicated with LL1 through LL4. Lighter areas correspond to high LDOS and high Fourier intensity, respectively, whereas dark areas correspond to low LDOS and low Fourier intensity, respectively. Arrows indicate ring structures in the FT images of the experimental data.

## Chapter 9

# Summary and Conclusion

We have investigated numerically how the interplay of electron-electron interactions and disorder affect the localization properties of electrons in the integer quantum Hall effect with regard to recent imaging and transport experiments. We diagonalised the Hamiltonian for electrons confined to two dimensions and subject to a perpendicular magnetic field in the suitable basis of Landau functions and treated interactions in an effective, self-consistent Hartree-Fock mean-field approximation.

The introductory part of this work established the basic fundamentals for describing electrons in the IQH regime using numerical methods. We outlined the characteristic electronic properties and their microscopic explanation, and introduced the Hartree-Fock approximation for treating the electron-electron interactions in systems of mesoscopic length scale. Throughout this work we put strong emphasis on comparing the behaviour of non-interacting and interacting systems. We concluded the first part by testing the universality of the MIT by calculating the participation ratio in the centre of the lowest Landau band for different system sizes, in the non-interacting and HF-interacting case, respectively. To the accuracy of our numerical calculations, we can conclude that the critical properties of the extended states remain unaltered whether interactions are taken into account or not, consistent with previous numerical [26, 115] and analytical work [111]. In particular, we found the correlation dimension as  $D(2) = 1.62 \pm 0.10$  in

both cases. Similarly, we obtained a critical exponent  $\tilde{\nu}$  between 2 and 2.4, compatible with the expected value  $2.34 \pm 0.04$  [34, 42]. However, we add that at the magnetic fields studied, the system is still not in the fully interaction-dominated regime. Studying the critical properties at higher fields might reveal so far unnoticed deviations from this behaviour.

In Chapter 6 we then turned to recent experimental results on the compressibility for high-mobility samples pointing to strong interaction-mediated effects even in the integer QH regime. Our calculations revealed substantial differences in the electronic compressibility between non-interacting and interacting systems when viewed as a joint function of magnetic field and carrier density. For interacting systems, we found strongly incompressible stripes of constant width around integer filling factors. We showed the dependence of the width of the stripes on the disorder configuration and computed the width based on a force balance argument. These results are in very good agreement with recent imaging experiments. Moreover, we observed strong  $g$ -factor enhancement as well as negative compressibility in the band centres, also consistent with experiments. We demonstrated that the incompressible patterns can be attributed to non-linear screening effects in the tails of the Landau bands. For magnetic fields larger than  $B_{\min}$ , the effects of linear screening — and hence interactions — dominate in the  $(B, n_e)$ -plane. Thus, our results support the existence of a greater variety of transport regimes due to electron-electron interactions in the integer quantum Hall effect.

Chapter 7 was dedicated to the investigation of transport behaviour when electron-electron interactions are present. We discussed problems in evaluating the Kubo formula for the conductivity due to the presence of the non-local exchange potential. We derived an alternative expression to the usual velocity form which makes use of the position expectation values. In order to evaluate them for a system with PBC, we used an expression similar to evaluating the single-point Berry phase. Finally, we outlined the results of our calculations for the Hall conductivity in the  $(B, n_e)$ -plane. Our single-particle calculations show a linear relation between the width of the plateau transition and the



magnetic field. In contrast, when taking interactions into account, we find a strong dependence of the width of the plateau-transition on the interaction. In the interaction dominated regime as defined by the linear screening criterion of Equation 6.12, the quantised plateaus show a constant width as a function of magnetic field, leading to an increasing width of the plateau transition. We interpret this behaviour similarly to the constant-width compressibility patterns and attribute it to the onset of linear screening. In this regime the electronic properties are strongly interaction dominated. Therefore our results do not display conductivity peaks aligning with integer filling factor, as observed experimentally [19]. Rather, the conductivity jumps irregularly strongly influenced by the exchange interaction. We argue that such patterns might become visible in simulations of larger systems which, however, is beyond our numerical capabilities.

Finally, in Chapter 8 we investigate interaction effects in STS imaging experiments. Tunneling of electrons between the sample and the STS tip allows to image the LDOS as a function of energy and tip position. The electrostatic potential of the STS tip leads to a local change of the effective potential felt by the 2DEG and induces states underneath. Introducing an additional QD-like potential into the simulation, we find good qualitative and quantitative agreement of a non-interacting calculation with the experimental data. Then, we systematically investigated how the measurements might be affected by the presence of both, the electrostatic STS tip potential and the induced states. For the non-interacting case, the effect can be summarised as constant energy shift of the LDOS, proportional to the tip strength. With electron-electron interactions present, the interpretation of the data, especially the position of the Landau levels, is more complicated and strongly depends on the sample Fermi level and the position of the tip-induced states. This combination complicates the analysis of STS data. Therefore our results may assist in the interpretation of experimental data.

We conclude this work with some final remarks. Whereas disorder is usually associated with a reduction of signal quality, in the IQHE the concurrence of a magnetic field, reduced dimensionality, and disorder leads to a remarkable resilience of quantised

transport. While the critical behaviour at the transition appears unaffected, localisation in the band tails is changed by interactions, yielding a significant change in the widths of the plateau regions. Although single-particle models can well describe many aspects of quantum Hall physics, only by taking interactions into account the whole spectrum of experimentally observed features can be satisfactorily understood. As a long-term goal, it would certainly be desirable to model the IQHE in a full many-body description. However, at present, the mesoscopic scale appears simply inaccessible to an exact treatment.

## Appendix A

# Calculation of Periodic Matrix Elements

Care has to be taken when computing matrix elements of periodic operators in a periodic basis,  $\langle \tilde{\varphi}_{n,k} | \tilde{V} | \tilde{\varphi}_{n',k'} \rangle$ , where the  $\tilde{\varphi}_{n,k}(\mathbf{r})$  and  $\tilde{V}(\mathbf{r})$  are  $L$ -periodic. We can write the wave functions as replicated Landau functions in  $x$ -direction of the form

$$\tilde{\varphi}_{n,k}(\mathbf{r}) = \lim_{P \rightarrow \infty} \frac{1}{\sqrt{2P+1}} \sum_{s=-P}^P \varphi_{n,k+sL/l_c^2}(\mathbf{r}) \quad (\text{A.1})$$

which is properly normalised as  $\langle \tilde{\varphi}_{n,k} | \tilde{\varphi}_{n',k'} \rangle = 1$ . The matrix element now reads

$$\langle \tilde{\varphi}_{n,k} | \tilde{V} | \tilde{\varphi}_{n',k'} \rangle = \lim_{P \rightarrow \infty} \frac{1}{2P+1} \sum_{s=-P}^P \sum_{t=-P}^P \int d^2\mathbf{r} \varphi_{n,k+sL/l_c^2}^*(\mathbf{r}) \tilde{V}(\mathbf{r}) \varphi_{n',k'-tL/l_c^2}(\mathbf{r}) . \quad (\text{A.2})$$

This can be rewritten as

$$\int d^2\mathbf{r} \varphi_{n,k+sL/l_c^2}^*(\mathbf{r}) \tilde{V}(\mathbf{r}) \varphi_{n',k'-tL/l_c^2}(\mathbf{r}) = \int d^2\mathbf{r} \varphi_{n,k+(s+t)L/l_c^2}^*(\mathbf{r}) \tilde{V}(\mathbf{r}) \varphi_{n',k'}(\mathbf{r}) , \quad (\text{A.3})$$

which is also valid for the case of general boundary conditions. The potential  $\tilde{V}(\mathbf{r})$  thereby remains unaffected due to its periodicity. The double sum can then be expressed

as a single sum by noting that  $(s+t) \in [-2P, 2P]$ , where each value has a degeneracy of  $2P+1-(s+t)$ . We can write

$$\langle \tilde{\varphi}_{n,k} | \tilde{V} | \tilde{\varphi}_{n',k'} \rangle = \lim_{P \rightarrow \infty} \sum_{u=-2P}^{2P} \frac{2P+1-u}{2P+1} \int d^2\mathbf{r} \varphi_{n,k+uL/l_c^2}(\mathbf{r}) V(\mathbf{r}) \varphi_{n',k'}(\mathbf{r}) \quad (\text{A.4})$$

$$= \sum_{u=-\infty}^{\infty} \int d^2\mathbf{r} \varphi_{n,k+uL/l_c^2}(\mathbf{r}) V(\mathbf{r}) \varphi_{n',k'}(\mathbf{r}) \quad (\text{A.5})$$

where the  $u$ -sum only needs to be taken to the neighbouring cells due to the exponential decay of the wave functions. Thus, we eventually obtain

$$\langle \tilde{\varphi}_{n,k} | \tilde{V} | \tilde{\varphi}_{n',k'} \rangle \approx \sum_{u=-1}^1 \langle \varphi_{n,k+uL/l_c^2} | \tilde{V} | \varphi_{n',k'} \rangle. \quad (\text{A.6})$$

## Appendix B

### Mobility

The differential scattering cross-section in 2D is given by (see Equation 126.9 in [32])

$$dw_{\mathbf{p}',\mathbf{p}} = \frac{4\pi m^*}{\hbar v_{\mathbf{p}}} |u_{\mathbf{p}'-\mathbf{p}}|^2 \delta(p'^2 - p^2) \frac{d^2 \mathbf{p}'}{(2\pi\hbar)^2} \quad (\text{B.1})$$

where  $u_{\mathbf{k}} = \int d^2 \mathbf{r} u(\mathbf{r}) \exp -i\mathbf{k} \cdot \mathbf{r}$  is the Fourier transform of the electron-impurity interaction potential. With  $\mathbf{k} = \mathbf{p}/\hbar$ , the mean free path  $\lambda_{\mathbf{k}} = v_{\mathbf{k}} \tau_{\mathbf{k}}$ , the impurity density in the plane,  $n_I$ , as well as

$$\lambda_{\mathbf{k}}^{-1} = n_I \int [1 - \cos(\phi)] dw_{\mathbf{k}',\mathbf{k}} \quad (\text{B.2})$$

we get

$$\frac{1}{\tau_{\mathbf{k}}} = \frac{m^* n_I}{\pi \hbar^3} \int d^2 \mathbf{k}' [1 - \cos(\theta)] |u_{\mathbf{k}'-\mathbf{k}}|^2 \delta(k'^2 - k^2) \quad (\text{B.3})$$

where  $\theta$  is the angle between  $\mathbf{k}$  and  $\mathbf{k}'$ .

If the electron-impurity interaction depends on the magnitude of  $\mathbf{k}' - \mathbf{k}$  only, we can make the replacements  $d^2 \mathbf{k}' = k' dk' d\theta$  and  $d(k'^2)/dk' = 2k'$  and get

$$\frac{1}{\tau_{\mathbf{k}}} = \frac{m^* n_I}{2\pi \hbar^3} \iint d\theta d(k'^2) [1 - \cos(\theta)] |\tilde{u}(2k \sin(\theta/2))|^2 \delta(k'^2 - k^2) \quad (\text{B.4})$$

$$= \frac{m^* n_I}{2\pi \hbar^3} \int d\theta [1 - \cos(\theta)] |\tilde{u}(2k \sin(\theta/2))|^2 \quad (\text{B.5})$$

where  $\tilde{u}(|\mathbf{k}' - \mathbf{k}|) = u_{\mathbf{k}'-\mathbf{k}}$  since  $\mathbf{k}'^2 = \mathbf{k}^2$  leading to  $(\mathbf{k}' - \mathbf{k})^2 = 2k \sin(\theta/2)$ .

In order to evaluate the mobility for a potential built up of many different scatterers, with each radially symmetric, we make use of that the total scattering cross-section is the sum of the individual scattering cross-sections,  $\sigma = \sum_i \sigma_i$ . The scattering rate in an area  $L^2$  is

$$r_{\text{scatt}}(k) = \sum_i \frac{\sigma_i(k)}{L^2}, \quad (\text{B.6})$$

which is the sum of the individual scattering areas (or cross-sections). Now the  $\sigma_i$  can be evaluated individually for each radially symmetric scatter. Especially, if the scatterers are the same with an areal density of  $n_I$ , then  $r_{\text{scatt}} = n_I \sigma_0(k)$ .

## Appendix C

### Commutators

Separating the coordinates into guiding centre and drift motion,

$$\begin{pmatrix} x \\ y \end{pmatrix} = \begin{pmatrix} \xi \\ \eta \end{pmatrix} + \begin{pmatrix} X \\ Y \end{pmatrix}, \quad (\text{C.1})$$

we have the following commutators among each other (zeros on the diagonal omitted for clarity):

$[\downarrow, \rightarrow]$	$x$	$y$	$\xi$	$\eta$	$X$	$Y$
$x$		0	0	$\mathfrak{i}l_c^2$	0	$-\mathfrak{i}l_c^2$
$y$	0		$-\mathfrak{i}l_c^2$	0	$\mathfrak{i}l_c^2$	0
$\xi$	0	$\mathfrak{i}l_c^2$		$\mathfrak{i}l_c^2$	0	0
$\eta$	$-\mathfrak{i}l_c^2$	0	$-\mathfrak{i}l_c^2$		0	0
$X$	0	$-\mathfrak{i}l_c^2$	0	0		$-\mathfrak{i}l_c^2$
$Y$	$\mathfrak{i}l_c^2$	0	0	0	$\mathfrak{i}l_c^2$	

Table C.1: Table of commutators between total, guiding centre, and drift motion coordinates.

## Appendix D

# Guiding Centre Velocity

For a clean system the Hamiltonian reads

$$H_0 = \frac{1}{2m} (\mathbf{p} - e\mathbf{A})^2 = \frac{1}{2m} \left( \begin{matrix} p_x \\ p_y - eBx \end{matrix} \right)^2 \equiv \frac{1}{2m} \boldsymbol{\pi}^2 \quad (\text{D.1})$$

where  $\boldsymbol{\pi}$  is the canonical momentum. Evaluating the EOM,

$$\dot{\pi}_x = \frac{i}{\hbar} [H_0, \pi_x] = \frac{i}{2m\hbar} [p_x^2 + p_y^2 - eBp_yx - eBxp_y + e^2B^2x^2, p_x] \quad (\text{D.2})$$

$$= \omega_c(p_y - eBx) = \omega_c\pi_y, \quad (\text{D.3})$$

$$\dot{\pi}_y = \frac{i}{\hbar} [H_0, \pi_y] = \frac{i}{2m\hbar} [p_x^2 + p_y^2 - eBp_yx - eBxp_y + e^2B^2x^2, p_y - eBx] \quad (\text{D.4})$$

$$= -\omega_cp_x = -\omega_c\pi_x, \quad (\text{D.5})$$

clearly reveals the cyclotron motion of the electrons and with  $x = \xi + X$  and  $y = \eta + Y$  we find

$$\pi_x = -\dot{\pi}_y/\omega_c = m\dot{\xi}, \quad (\text{D.6})$$

$$\pi_y = \dot{\pi}_x/\omega_c = m\dot{\eta} \quad (\text{D.7})$$

and

$$\xi = -\frac{\pi_y}{m\omega_c}, \quad (\text{D.8})$$

$$\eta = \frac{\pi_x}{m\omega_c}. \quad (\text{D.9})$$



With the following commutation relations

$$[\pi_x, \pi_y] = [p_x, p_y - eBx] = i\hbar eB = i\hbar m\omega_c, \quad (\text{D.10})$$

$$[\pi_x, x] = [\pi_y, y] = -i\hbar, \quad (\text{D.11})$$

$$[\xi, \eta] = \frac{i\hbar}{m\omega_c} = il_c^2, \quad (\text{D.12})$$

$$[H_0, \pi_x] = \frac{1}{2m}[\pi_x^2 + \pi_y^2, \pi_x] = \frac{1}{2m}(\pi_y\pi_y\pi_x - \pi_x\pi_y\pi_y) = -i\hbar\omega_c\pi_y \quad (\text{D.13})$$

$$[H_0, \pi_y] = \frac{1}{2m}[\pi_x^2 + \pi_y^2, \pi_y] = \frac{1}{2m}(\pi_x\pi_x\pi_y - \pi_y\pi_x\pi_x) = i\hbar\omega_c\pi_x \quad (\text{D.14})$$

we can find the EOM for a Hamiltonian of the form

$$H = H_0 + V. \quad (\text{D.15})$$

With  $p_\mu = \frac{\hbar}{i}\partial_\mu$  and  $[V, x_\mu] = 0$ , we have the commutators

$$[V, \pi_x] = i\hbar\partial_x V, \quad (\text{D.16})$$

$$[V, \pi_y] = i\hbar\partial_y V, \quad (\text{D.17})$$

and find for the EOM

$$\dot{\xi} = \frac{i}{\hbar}[H, \xi] = -\frac{i}{m\hbar\omega_c}[H_0 + V, \pi_y] = \frac{\pi_x}{m} + \frac{l_c^2}{\hbar}\partial_y V, \quad (\text{D.18})$$

$$\dot{\eta} = \frac{i}{\hbar}[H, \eta] = \frac{i}{m\hbar\omega_c}[H_0 + V, \pi_x] = \frac{\pi_y}{m} - \frac{l_c^2}{\hbar}\partial_x V, \quad (\text{D.19})$$

$$\dot{x} = \frac{i}{\hbar}[H, x] = \frac{i}{2m\hbar}(\pi_x\pi_x x - x\pi_x\pi_x) = \frac{\pi_x}{m}, \quad (\text{D.20})$$

$$\dot{y} = \frac{i}{\hbar}[H, y] = \frac{i}{2m\hbar}(\pi_y\pi_y y - y\pi_y\pi_y) = \frac{\pi_y}{m}, \quad (\text{D.21})$$

and thus

$$\dot{X} = \dot{x} - \dot{\xi} = -\frac{l_c^2}{\hbar}\partial_y V, \quad (\text{D.22})$$

$$\dot{Y} = \dot{y} - \dot{\eta} = \frac{l_c^2}{\hbar}\partial_x V, \quad (\text{D.23})$$

which reflects the drift motion of the guiding centres along equipotential lines of the disorder potential.

## Appendix E

# Formulas Involving Landau Functions

The following useful expressions are utilised in this work. Landau function have the properties

$$(x - k_b l_c^2) \varphi_{m,b}(\mathbf{r}) = l_c \left[ \sqrt{\frac{m}{2}} \varphi_{m-1,b}(\mathbf{r}) + \sqrt{\frac{m+1}{2}} \varphi_{m+1,b}(\mathbf{r}) \right] \quad (\text{E.1})$$

$$\partial_x \varphi_{m,b}(\mathbf{r}) = l_c^{-1} \left[ \sqrt{\frac{m}{2}} \varphi_{m-1,b}(\mathbf{r}) - \sqrt{\frac{m}{2}} \varphi_{m+1,b}(\mathbf{r}) \right] \quad (\text{E.2})$$

$$\varphi_{m,b}(\mathbf{r}, \mathbf{k}) = \frac{\exp[\mathbf{i} k_x (x - k_b l_c^2)]}{\sqrt{2^m m!} \sqrt{\pi} l_c L} \exp \left[ \mathbf{i} k_b y - \frac{(x - (k_b + k_y) l_c^2)^2}{2 l_c^2} \right] \times \\ H_m \left[ \frac{x - (k_b + k_y) l_c^2}{l_c} \right]. \quad (\text{E.3})$$

The plane wave matrix elements for PBC are

$$S_{n,k;n',k'}(\mathbf{q}) = \langle \varphi_{n,k} | \exp(\mathbf{i} \mathbf{q} \cdot \mathbf{r}) | \varphi_{n',k'} \rangle = \\ \delta'_{q_y, k-j} \sqrt{\frac{2^n m!}{2^m n!}} \exp \left( -\frac{\mathbf{q}^2}{4} + \frac{\mathbf{i}}{2} q_x (k+j) \right) \left( \frac{\mathbf{i} q_x - q_y}{2} \right)^{n-m} L_m^{n-m} \left( \frac{\mathbf{q}^2}{2} \right), \quad (\text{E.4})$$

if  $n \geq n'$  and  $L_n^a(x)$  are the generalised Laguerre polynomials. For periodic boundaries, the delta function is defined with modulus, i.e.

$$\delta'_{a,b} = \begin{cases} 1 & \text{if } \text{mod}(a-b, N_\phi) = 0, \\ 0 & \text{otherwise.} \end{cases} \quad (\text{E.5})$$

Thus the bielectronic integrals

$$G_{n,k;n',k'}^{m,l;m',l'} = \sum_{\mathbf{q} \neq 0} v(\mathbf{q}) S_{n,k;n',k'}(\mathbf{q}) S_{m,l;m',l'}(-\mathbf{q}) \quad (\text{E.6})$$

simplify to (if  $n \geq n'$  and  $m \geq m'$ )

$$\begin{aligned} G_{n,k;n',k'}^{m,l;m',l'} = & \sum_{q_y} \delta_{q_y, k-k'} \delta_{l', l+k-k'} \sum_{q_x} v(\mathbf{q}) \sqrt{\frac{2^n n'!}{2^{n'} n!}} \sqrt{\frac{2^m m'!}{2^{m'} m!}} e^{-\frac{\mathbf{q}^2}{2} + i q_x (k' - l)} \\ & \times \left( \frac{i q_x - q_y}{2} \right)^{n-n'} \left( \frac{q_y - i q_x}{2} \right)^{m-m'} L_{n'}^{n-n'} \left( \frac{\mathbf{q}^2}{2} \right) L_{m'}^{m-m'} \left( \frac{\mathbf{q}^2}{2} \right). \end{aligned} \quad (\text{E.7})$$

The plane wave matrix elements for general boundary conditions read

$$S_{n,k;n',k'}(\mathbf{q}, \mathbf{k}) = \langle \varphi_{n,k}(\mathbf{k}) | \exp(i \mathbf{q} \cdot \mathbf{r}) | \varphi_{n',k'}(\mathbf{k}) \rangle = \exp [i l_c^2 (\mathbf{q} \times \mathbf{k})_z] S_{n,k;n',k'}(\mathbf{q}) \quad (\text{E.8})$$

The derivatives with respect to the phase shift read

$$\partial_{k_x} \varphi_{m,b}(\mathbf{r}, \mathbf{k})|_{\mathbf{k}=0} = -i(x - k_b l_c^2) \varphi_{m,b}(\mathbf{r}) = -i l_c \left[ \sqrt{\frac{m+1}{2}} \varphi_{m+1,b} + \sqrt{\frac{m}{2}} \varphi_{m-1,b}(\mathbf{r}) \right] \quad (\text{E.9})$$

and

$$\partial_{k_y} \varphi_{m,b}(\mathbf{r}, \mathbf{k})|_{\mathbf{k}=0} = l_c \left[ \sqrt{\frac{m+1}{2}} \varphi_{m+1,b} - \sqrt{\frac{m}{2}} \varphi_{m-1,b}(\mathbf{r}) \right] \quad (\text{E.10})$$

# Bibliography

- [1] K. v. Klitzing, G. Dorda, and M. Pepper, Phys. Rev. Lett. **45**, 494 (1980).
- [2] B. Jeckelmann and B. Jeanneret, Rep. Prog. Phys. **64**, 1603 (2001).
- [3] D. C. Tsui, H. L. Stormer, and A. C. Gossard, Phys. Rev. Lett. **48**, 1559 (1982).
- [4] R. B. Laughlin, Phys. Rev. B **23**, 5632 (1981).
- [5] R. B. Laughlin, Phys. Rev. Lett. **50**, 1395 (1983).
- [6] F. D. M. Haldane, Phys. Rev. Lett. **51**, 605 (1983).
- [7] B. I. Halperin, Phys. Rev. Lett. **52**, 2390 (1984).
- [8] R. E. Prange, Phys. Rev. B **23**, 4802 (1981).
- [9] T. Chakraborty and P. Pietiläinen, *The Quantum Hall effects* (Springer, Berlin, 1995).
- [10] M. Janssen, O. Viehweger, U. Fastenrath, and J. Hajdu, *Introduction to the Theory of the Integer Quantum Hall effect* (VCH, Weinheim, 1994).
- [11] A. M. M. Pruisken, Nucl. Phys. B **235**, 277 (1984).
- [12] D. J. Thouless, M. Kohmoto, M. P. Nightingale, and M. den Nijs, Phys. Rev. Lett. **49**, 405 (1982).
- [13] *The Quantum Hall Effect*, edited by R. E. Prange and S. M. Girvin (Springer, Berlin, 1987).
- [14] J. T. Chalker and P. D. Coddington, J. Phys.: Condens. Matter **21**, 2665 (1988).
- [15] P. Cain and R. A. Römer, EuroPhys. Lett. **66**, 104 (2004).
- [16] B. Kramer, T. Ohtsuki, and S. Kettmann, Phys. Rep. **417**, 211 (2005), ArXiv: cond-mat/0409625.
- [17] S. Ilani, J. Martin, E. Teitelbaum, J. Smet, D. Mahalu, V. Umansky, and A. Yacoby, Nature **427**, 328 (2004).
- [18] J. Martin, S. Ilani, B. Verdene, J. Smet, V. Umansky, D. Mahalu, D. Schuh, G. Abstreiter, and A. Yacoby, Science **305**, 980 (2004).
- [19] D. H. Cobden, C. H. W. Barnes, and C. J. B. Ford, Phys. Rev. Lett. **82**, 4695 (1999).
- [20] T. Machida, S. Ishizuka, S. Komiyama, K. Muraki, and Y. Hirayama, Phys. Rev. B **63**, 045318 (2001).

- [21] O. E. Dial, R. C. Ashoori, L. N. Pfeiffer, and K. W. West, *Nature* **448**, 176 (2007).
- [22] J. P. Eisenstein, L. N. Pfeiffer, and K. W. West, *Phys. Rev. Lett.* **68**, 674 (1992).
- [23] S. G. Semenchinskii, **41**, 605 (1985).
- [24] L. Zheng and H. A. Fertig, *Phys. Rev. B* **50**, 4984 (1994).
- [25] D.-H. Lee and Z. Wang, *Phys. Rev. Lett.* **76**, 4014 (1996).
- [26] S.-R. E. Yang, A. H. MacDonald, and B. Huckestein, *Phys. Rev. Lett.* **74**, 3229 (1995).
- [27] E. H. Hall, *Amer. Jour. Math.* 2:287 (1879).
- [28] G. D. Mahan, *Many Particle Physics* (Kluwer Academic/Plenum, New York, 2000).
- [29] N. W. Ashcroft and N. D. Mermin, *Solid State Physics* (Saunders College, New York, 1976).
- [30] *The Hall Effect and Its Applications*, edited by L. Chien and C. W. Westgate (Plenum, New York, 1980).
- [31] T. Ando, A. B. Fowler, and F. Stern, *Rev. Mod. Phys.* **54**, 437 (1982).
- [32] L. D. Landau and E. M. Lifshitz, *Quantum Mechanics* (Butterworth-Heinemann, Oxford, 1981).
- [33] T. Dittrich, P. Hänggi, G.-L. Ingold, B. Kramer, G. Schön, and W. Zwerger, *Quantum Transport and Dissipation* (Wiley-VCH, Berlin, 1998).
- [34] B. Huckestein, *Rev. Mod. Phys.* **67**, 357396 (1995).
- [35] F. Wegner, *Z. Phys. B* **35**, 207 (1979).
- [36] F. Wegner, *Z. Phys. B* **36**, 209 (1980).
- [37] E. Abrahams, P. W. Anderson, D. C. Licciardello, and T. V. Ramakrishnan, *Phys. Rev. Lett.* **42**, 673 (1979).
- [38] H. Aoki, *J. Phys. C* **16**, L205 (1983).
- [39] H. Aoki, *Phys. Rev. B* **33**, 7310 (1986).
- [40] L. Schweitzer, B. Kramer, and A. MacKinnon, *J. Phys. C* **17**, 4111 (1984).
- [41] H. Aoki and T. Ando, *Phys. Rev. Lett.* **54**, 831 (1985).
- [42] B. Huckestein and B. Kramer, *Phys. Rev. Lett.* **64**, 1437 (1990).
- [43] Y. Huo and R. N. Bhatt, *Phys. Rev. Lett.* **68**, 1375 (1992).
- [44] P. Cain, R. A. Römer, and M. E. Raikh, *Phys. Rev. B* **67**, 075307 (2003), ArXiv: cond-mat/0209356.
- [45] B. Huckestein and L. Schweitzer, *Phys. Rev. Lett.* **72**, 713 (1994).
- [46] R. A. Römer and H. Schulz-Baldes, *Europhys. Lett.* **68**, 247 (2004).
- [47] P. A. Lee and T. V. Ramakrishnan, *Rev. Mod. Phys.* **57**, 287 (1985).
- [48] D. Belitz and T. R. Kirkpatrick, *Rev. Mod. Phys.* **66**, 261 (1994).
- [49] J. Rammer, *Quantum Transport Theory* (Westview Press Inc, New York, 2004).

- [50] J. T. Chalker and G. J. Daniell, Phys. Rev. Lett. **61**, 593 (1988).
- [51] H. Levine, S. B. Libby, and A. M. M. Pruiskien, Phys. Rev. Lett. **51**, 1915 (1983).
- [52] A. Pruiskien and I. Burmistrov, Annals of Physics **316**, 285 (2005).
- [53] A. M. M. Pruiskien and I. S. Burmistrov, cond-mat/0507412 (2005).
- [54] A. M. M. Pruiskien and I. S. Burmistrov, cond-mat/0502488 (2005).
- [55] D. R. Hofstadter, Phys. Rev. B **14**, 2239 (1976).
- [56] T. Nakanishi, T. Ohtsuki, and M. Saitoh, J. Phys. Soc. Jpn. **64**, 2092 (1995).
- [57] J.-L. Pichard and G. Sarma, J. Phys. C **14**, L127 (1981).
- [58] J.-L. Pichard and G. Sarma, J. Phys. C **14**, L617 (1981).
- [59] A. MacKinnon and B. Kramer, Z. Phys. B **53**, 1 (1983).
- [60] B. Kramer and A. MacKinnon, Rep. Prog. Phys. **56**, 1469 (1993).
- [61] A. MacKinnon, J. Phys.: Condens. Matter **6**, 2511 (1994).
- [62] Y. Ono, T. Ohtsuki, and B. Kramer, J. Phys. Soc. Japan **65**, 1734 (1996), ArXiv: cond-mat/9603099.
- [63] D.-H. Lee, Phil. Mag. Lett. **73**, 145 (1996).
- [64] M. Tsukada, J. Phys. Soc. Jpn. **41**, 1466 (1976).
- [65] P. Cain and R. A. Römer, Int. J. Mod. Phys. B **19**, 2085 (2005).
- [66] P. Cain, R. A. Römer, M. Schreiber, and M. E. Raikh, Phys. Rev. B **64**, 235326 (2001), ArXiv: cond-mat/0104045.
- [67] N. R. Cooper and J. T. Chalker, Phys. Rev. B **48**, 4530 (1993).
- [68] N. d'Ambrumenil, B. I. Halperin, and R. Morf, , unpublished.
- [69] B. Huckestein and B. Kramer, Sol. Stat. Comm. **71**, 445 (1989).
- [70] D. Yoshioka, B. I. Halperin, and P. A. Lee, Phys. Rev. Lett. **50**, 1219 (1983).
- [71] A. L. Efros, Solid State Commun. **67**, 1019 (1988).
- [72] A. L. Efros, Solid State Commun. **70**, 253 (1989).
- [73] T. Ando, J. Phys. Soc. Jpn. **52**, 1740 (1983).
- [74] H. Aoki, J. Phys. C **12**, 633 (1979).
- [75] A. H. MacDonald and G. C. Aers, Phys. Rev. B **34**, 2906 (1986).
- [76] H. Haug and S. Koch, *Quantum Theory of the Optical and Electronic Properties of Semiconductors* (World Scientific Publishing, London, 2004).
- [77] M. Backhaus and B. Huckestein, Int. J. Mod. Phys. B **15**, 1369 (2001).
- [78] C. C. J. Roothaan, Rev. Mod. Phys. **23**, 69 (1951).
- [79] D. Pfannkuche, V. Gudmundsson, and P. A. Maksym, Phys. Rev. B **47**, 2244 (1993).
- [80] F. Epperlein, M. Schreiber, and T. Vojta, Phys. Rev. B **56**, 5890 (1997).

- [81] T. Vojta, F. Epperlein, and M. Schreiber, Phys. Rev. Lett. **81**, 4212 (1998).
- [82] D. C. Thompson and A. Alavi, J. Chem. Phys. **122**, 124107 (2005).
- [83] M. Defranceschi and C. L. Bris, *Mathematical models and methods for ab initio Quantum Chemistry*, Vol. 74 of *Lecture Notes in Chemistry* (Springer, Berlin, 2000).
- [84] L. Cohen and C. Frishberg, Phys. Rev. A **13**, 927 (1976).
- [85] H. Nakatsuji, Phys. Rev. A **14**, 41 (1976).
- [86] H. Schlosser, Phys. Rev. A **15**, 1349 (1977).
- [87] J. E. Harriman, Phys. Rev. A **19**, 1893 (1979).
- [88] H. Haken, *Quantenfeldtheorie des Festkörpers* (Teubner, Stuttgart, 1973).
- [89] I. S. Gradshteyn and I. M. Ryzhik, *Table of Integrals, Series and Products* (Academic Press, London, 1994).
- [90] J. A. Pople and R. K. Nesbet, J. Chem. Phys. **22**, 571 (1954).
- [91] W. H. Adams, Phys. Rev. **127**, 1650 (1962).
- [92] J. S. Andrews, D. Jayatilaka, R. G. A. Bone, N. C. Handy, and R. D. Amos, Chem. Phys. Lett. **183**, 423 (1991).
- [93] P. Nandi, T. Kar, and A. Sannigrahi, J. Mol. Struct. (Theochem) **362**, 69 (1996).
- [94] D. Yoshioka and H. Fukuyama, J. Phys. Soc. Jpn. **47**, 394 (1979).
- [95] A. MacDonald and S. Girvin, Phys. Rev. B **38**, 6295 (1988).
- [96] E. Cancès and C. L. Bris, Int. J. Quantum Chem. **79**, 82 (2000).
- [97] M. Challacombe and E. Schwegler, J. Chem. Phys. **106**, 5526 (1997).
- [98] A. D. Daniels and G. E. Scuseria, J. Chem. Phys. **110**, 1321 (1999).
- [99] R. McWeeny, *Methods of Molecular Quantum Mechanics* (Academic Press, New York, 1992).
- [100] V. R. Saunders and I. H. Hillier, Int. J. Quantum Chem. **7**, 699 (1973).
- [101] S. Das Sarma and F. Stern, Phys. Rev. B **32**, 8442 (1985).
- [102] I. Lo, W. C. Mitchel, R. E. Perrin, R. L. Messham, and M. Y. Yen, Phys. Rev. B **43**, 11787 (1991).
- [103] C. Weisbuch and C. Hermann, Phys. Rev. B **15**, 816 (1977).
- [104] *Semiconductors - Basic Data*, edited by O. Madelung (Springer, Berlin, 1996).
- [105] T. Ando, J. Phys. Soc. Jpn. **53**, 3101 (1984).
- [106] S.-R. E. Yang and A. H. MacDonald, Phys. Rev. Lett. **70**, 4110 (1993).
- [107] J. Tersoff and D. R. Hamann, Phys. Rev. Lett. **50**, 1998 (1983).
- [108] J. Wiebe, Ph.D. thesis, Universität Hamburg, 2003.
- [109] J. K. Jain and S. A. Kivelson, Phys. Rev. Lett. **60**, 1542 (1988).

- [110] M. Backhaus and B. Huckestein, *Physica B* **256–58**, 52 (1998).
- [111] A. M. M. Pruisken, M. A. Baranov, and B. Škorić, *Phys. Rev. B* **60**, 16807 (1999).
- [112] J. Bauer, T.-M. Chang, and J. L. Skinner, *Phys. Rev. B* **42**, 8121 (1990).
- [113] C. M. Soukoulis and E. N. Economou, *Phys. Rev. Lett.* **52**, 565 (1984).
- [114] M. Janssen, *Int. J. Mod. Phys. B* **8**, 943 (1994).
- [115] A. Struck and B. Kramer, *Phys. Rev. Lett.* **97**, 106801 (2006).
- [116] A. M. M. Pruisken and M. Voropaev, , unpublished.
- [117] H. van Houten, C. W. J. Beenakker, and A. A. M. Staring, *arXiv:cond-mat/0508454* (2005).
- [118] J. F. Janak, *Phys. Rev.* **178**, 1416 (1969).
- [119] R. J. Nicholas, R. J. Haug, K. v. Klitzing, and G. Weimann, *Phys. Rev. B* **37**, 1294 (1988).
- [120] A. Manolescu and R. R. Gerhardts, *Phys. Rev. B* **51**, 1703 (1995).
- [121] I. L. Aleiner and L. I. Glazman, *Phys. Rev. B* **52**, 11296 (1995).
- [122] S. V. Kravchenko, V. M. Pudalov, and S. G. Semenchinsky, *Physics Letters A* **141**, 71 (1989).
- [123] R. Côté and A. H. MacDonald, *Phys. Rev. B* **44**, 8759 (1991).
- [124] A. L. Efros, *J. Comput. System Sci.* **65**, 1281 (1988).
- [125] A. L. Efros, *Solid State Commun.* **70**, 253 (1989).
- [126] A. L. Efros, *Phys. Rev. B* **45**, 11354 (1992).
- [127] U. Wulf, V. Gudmundsson, and R. R. Gerhardts, *Phys. Rev. B* **38**, 4218 (1988).
- [128] S. Ihnatsenka and I. V. Zozoulenko, *Phys. Rev. B* **73**, 155314 (2006).
- [129] J. K. Jain, *Physica E* **20**, 79 (2003).
- [130] J. K. Jain, *Phys. Rev. Lett.* **63**, 199 (1989).
- [131] J. K. Jain, *Physics Today* 39 (2000).
- [132] R. R. Du, H. L. Stormer, D. C. Tsui, L. N. Pfeiffer, and K. W. West, *Phys. Rev. Lett.* **70**, 2944 (1993).
- [133] H. L. Stormer, D. C. Tsui, and A. C. Gossard, *Rev. Mod. Phys.* **71**, S298 (1999).
- [134] R. Kubo, *J. Phys. Soc. Japan* **12**, 570 (1957).
- [135] H. Aoki and T. Ando, *Solid State Commun.* **38**, 1079 (1981).
- [136] S. Ismail-Beigi, E. K. Chang, and S. G. Louie, *Phys. Rev. Lett.* **87**, 087402 (2001).
- [137] M. V. Berry, *Proc. R. Soc. A* **392**, 45 (1984).
- [138] R. Resta, *Phys. Rev. Lett.* **80**, 1800 (1998).
- [139] R. Resta and S. Sorella, *Phys. Rev. Lett.* **82**, 370 (1999).
- [140] A. A. Aligia and G. Ortiz, *Phys. Rev. Lett.* **82**, 2560 (1999).



- [141] R. Resta, Phys. Rev. Lett. **95**, 196805 (2005).
- [142] E. Yaschenko, L. Fu, L. Resca, and R. Resta, Phys. Rev. B **58**, 1222 (1998).
- [143] Q. Niu, D. J. Thouless, and Y.-S. Wu, Phys. Rev. B **31**, 3372 (1985).
- [144] G. Bergmann, Phys. Rep. **107**, 1 (1984).
- [145] R. Resta, J. Phys. Cond. Mat. **12**, R107 (2000).
- [146] Y. Aharonov and D. Bohm, Phys. Rev. **115**, 485 (1959).
- [147] A. Tomita and R. Y. Chiao, Phys. Rev. Lett. **57**, 937 (1986).
- [148] M. Kugler and S. Shtrikman, Phys. Rev. D **37**, 934 (1988).
- [149] Y.-S. M. Wu, A. Kuppermann, and B. Lepetit, Chem. Phys. Lett. **186**, 319 (1991).
- [150] H. von Busch, V. Dev, H.-A. Eckel, S. Kasahara, J. Wang, W. Demtröder, P. Sebald, and W. Meyer, Phys. Rev. Lett. **81**, 4584 (1998).
- [151] D. Xiao, Y. Yao, Z. Fang, and Q. Niu, Physical Review Letters **97**, 026603 (2006).
- [152] D. P. Arovas, R. N. Bhatt, F. D. M. Haldane, P. B. Littlewood, and R. Rammal, Phys. Rev. Lett. **60**, 619 (1988).
- [153] M. Morgenstern, J. Klijn, C. Meyer, M. Getzlaff, R. Adelung, R. A. Römer, K. Rossnagel, L. Kipp, M. Sibowski, and R. Wiesendanger, Phys. Rev. Lett. **89**, 136806 (2002), ArXiv: cond-mat/0202239.
- [154] M. Morgenstern, J. Klijn, C. Meyer, and R. Wiesendanger, Phys. Rev. Lett. **90**, 056804 (2003).
- [155] J. Tersoff and D. R. Hamann, Phys. Rev. B **31**, 805 (1985).
- [156] R. Dombrowski, C. Steinebach, C. Wittneven, M. Morgenstern, and R. Wiesendanger, Phys. Rev. B **59**, 8043 (1999).
- [157] K. Hashimoto, C. Sohrmann, M. Morgenstern, T. Inaoka, J. Wiebe, R. A. Römer, Y. Hirayama, and R. Wiesendanger, (2007), in preparation.
- [158] G. Lehner, *Elektromagnetische Feldtheorie für Ingenieure und Physiker* (Springer, Berlin, 2004).
- [159] F. F. Fang and W. E. Howard, Phys. Rev. Lett. **16**, 797 (1966).
- [160] F. Stern and W. E. Howard, Phys. Rev. **163**, 816 (1967).
- [161] G. A. Khodaparast, D. C. Larrabee, J. Kono, D. S. King, S. J. Chung, and M. B. Santos, Phys. Rev. B **67**, 035307 (2003).
- [162] V. Y. Aristov, V. M. Zhilin, C. Grupp, A. Taleb-Ibrahimi, H. J. Kim, P. S. Mangat, P. Soukiassian, and G. L. Lay, Appl. Surf. Sci. **166**, 263 (2000).